NTNU

Norwegian University of
Science and Technology

Joint Rock Physics Inversion of Seismic and Electromagnetic Data for CO2 Monitoring at Sleipner

Isa Adi Subagjo

Abstract

The Carbon Capture and Storage project that is taking place at the Sleipner field involving the injection of CO_2 into Utsira sandstone reservoir at 1012 m below sea level. The migration of CO_2 must be monitored to understand the amount and composition of CO_2 inside the reservoir. The goal of this study is to estimate petrophysical parameters such as CO_2 saturation and its mixing type inside the reservoir by jointly inverting P-wave velocity and resistivity model.

In this study, the effective fluid model is combined with rock physic models to estimate rock physic properties. In the effective fluid model, the fluid mixing type is determined by Brie equation. Here, the fluid mixture is controlled by Brie exponent (e) and this parameter can be spatially heterogeneous inside the reservoir. In Utsira, velocity-saturation curves confirm that the velocity change due to CO_2 saturation is variable depending on Brie exponent (e). To reduce the uncertainty related to saturation and its mixing type, resistivity is combined with P-wave velocity as input in the rock physic inversion. For inversion, semi-global optimization method called Neighbourhood Algorithm is used to explore the space of possible solutions.

To reduce the number of unknowns in the inversion, some a priori properties are defined from log data. These properties are used to invert frame properties using P-wave velocity before CO_2 injection (1994 data). All information from the baseline model are then used as a priori to invert saturation and Brie exponent. Here, the input for inversion are P-wave velocity and resistivity after CO_2 injection (2008 data).

CO_2 saturation in Sleipner estimated from joint rock physics inversion can reach 68% with uncertainty of around 20%. The same test also shows that the Brie exponent (e) for CO_2 saturation higher than 15% is around 7, suggesting that the mixing type of CO_2 and brine is somewhere between patchy and uniform. These results are variable depend on the chosen parameters. The study shows that two different geophysical methods can be combined to provide complementary information for discrimination of CO_2 saturation and its mixing type.

Preface

This thesis was written as part of a two year master study in Petroleum Geosciences at the Norwegian University of Science and Technology (NTNU), to complete an *Master of Science* (MSc) degree in petroleum geophysics. The thesis represents 30 ECTS credit points, which is equivalent to a one semester study. The study was conducted in collaboration with SINTEF Industry, under supervision of Alexey Stovas (NTNU) and Bastien Dupuy (SINTEF).

This research is an exclusive continuation of my specialization project conducted in Fall 2017 with the title "Sensitivity Tests of Joint Rock Physics Inversion for CO_2 Characterization at Sleipner"

Acknowledgements

Contents

List of Figures

List of Tables

1 Introduction

Carbon Capture and Storage (CCS) is a method to reduce the growing emission of CO_2 in the atmosphere by separating the CO_2 from energy-related sources and transport it to the permanent disposal in deep underground rock formations. The CO_2 will be trapped far below the surface by thick and impermeable layers of cap rocks. Over time, the CO_2 will dissolve in water and combine chemically with the rocks in the aquifer. The CCS project taking place at the Sleipner field, North Sea is the world's first industrial-scale for the purpose of carbon emission reduction. The project involves the injection of CO_2 into Utsira sandstone formation at depth 1012 m below sea level. The CO_2 is separated on the offshore platform from the produced hydrocarbon and pumped into the aquifer. Since 1996, this site has been operating with a rate of injection 0.9 metric tons of CO_2 yearly. The CCS project must be carefully tracked through periodic monitoring. This is a crucial factor to determine the development of CO_2 migration path in the aquifer and the potential of geological hazards that might lead to gas leakage.

Most of the technologies that is being used for monitoring are already in existence for other purposes such as for hydrocarbon reservoir. In Sleipner, ten 3D seismic surveys have been acquired to date (Furre, Eiken, Alnes, Vevatne, & Kiær, 2017). The repeated survey is important to determine the alterations occurring in the reservoir because of CO_2 injection into the aquifer by comparing the repeated datasets. In Sleipner, the effect of CO_2 on the seismic data can be tracked nicely through time. It was found that the injected CO_2 gas leads to stronger negative seismic amplitudes (bright spot) and reach the top of reservoir in 1999. (Arts, Chadwick, Eiken, Thibeau, & Nooner, 2008).

The use of different geophysical methods is required to provide complementary information for seismic method. In 2008, a Controlled Source Electromagnetic (CSEM) test line was acquired at Sleipner. The 2.5D inversion of marine electromagnetic data shows that there is no sign of the injected CO_2 leaking through the cap rock and overburden (Park, Sauvin, Vöge, & Vanneste, 2016). Several studies suggest that although the resistivity anomaly of the CO_2 plume in Sleipner is small (Park, Viken, Bjørnarå, & Aker, 2011), there is a possibility of applying CSEM method to monitor CO_2 inside monitoring (Bhuiyan, Landrø, & Johansen, 2012), (Park, Fawad, Viken, Aker, & Bjørnarå, 2013).

During the last decades, many geophysical techniques have been developed to delineate the reservoir properties. The integration of two different methods, CSEM and seismic, provide considerable value for reservoir monitoring as one method alone will provide incomplete information because of non-uniqueness and limited spatial resolution (Abubakar, Gao, & Habashy, 2012). In this case, building relationship between poroelastic parameters and rock-fluid models is performed by inverting the petrophysical parameters (for example fluid saturation) using seismic and electromagnetic attributes as input data simultaneously. Several studies show that the joint-inversion approach can accurately estimate the porosity distribution and saturation changes caused by hydrocarbon production (Abubakar et al., 2012), (Gao, Abubakar, & Habashy, 2012). Joint interpretation study at Sleipner CO_2 storage also confirms its capability to quantify the total mass of CO_2 (Park, Sauvin, & Vöge, 2017).

In seismic monitoring, one of the most important type of reservoir changes is fluid satu-

ration. The recent study in Sleipner shows that the CO_2 saturations can be low and high depending on the rock physics model chosen (Dupuy et al., 2017). However, several studies at Sleipner shows that the CO_2 saturation is difficult to estimate reliably because the way the fluids are mixed up in the porous medium is unknown (Queißer & Singh, 2013), (Ghosh, Sen, & Vedanti, 2015), and (Dupuy et al., 2017). In the effective fluid model, the distribution type is determined by choosing the correct value of Brie exponent (e). In fact, Brie exponent is varying between 1 and 40, and can be spatially heterogeneous inside the reservoir (Brie, Pampuri, Marsala, & Meazza, 1995). The sensitivity study confirms that the viscoelastic attributes in Utsira sandstone are sensitive to Brie exponent. It shows that small variations of Brie exponent may lead to large disparity of seismic velocity (Subagjo, 2017). The goal of this study is to reduce the uncertainty regarding the fluid saturation estimates and its spatial distribution by adding CSEM resistivity input to seismic velocity. The study aims to give a better understanding of CO_2 saturation and distribution type in Sleipner by inverting 1D and 2D velocity and resistivity model simultaneously. Using this method, the capability to quantify the CO_2 development in the reservoir will be enhanced.

The thesis consists of 7 chapters and a continuation of a project with the title *"Sensitivity Tests of Joint Rock Physics Inversion for CO$_2$ Characterization at Sleipner"* (Subagjo, 2017). The summary of the report can be read on Chapter 2 in this report. The results obtained from the sensitivity test are set as the reference for 1D and 2D rock physics inversions using P-wave velocity and resistivity model data from Sleipner (Chapter 2). Neighbourhood Algorithm (NA) (Sambridge, 1999a) is used to minimize the misfit function between the observed data and calculated data. For the inversion, realistic a priori are extracted by applying the information from well data and geological settings of Utsira sandstone and Nordland Shale (Chapter 3). Chapter 4 presents the work-flow of the research together with velocity and resistivity model limitation that are used as input for 1D and 2D inversion. Chapter 5 shows the results of 1D and 2D inversions of Sleipner data and at Chapter 6 the interpretation of CO_2 saturation and its mixing distribution in Sleipner is presented. Conclusions, important remarks, and recommendations for future researches are summarized in Chapter 7.

2 Theory

2.1 Forward Modeling

Forward modeling is the use of geological and geophysical models of the subsurface formations to simulate seismic experiments. Subsurface formations have a big scale of heterogeneity and several models have been developed to be used for different geologic scenarios (for details, see (Avseth, Mukerji, & Mavko, 2005)). The origin of heterogeneity can be caused by either lithological variations or different geometrical distribution of the fluid phases. In this research, effective fluid phase plugged into extended Biot theory (Biot, 1956a, 1956b) is used in rock physics modeling. In addition to seismic, the electromagnetic methods (EM) is chosen to derive resistivity structure inside the reservoir. In this study, the resistivity forward modeling is derived from empirical formula by Archie (Archie, 1942).

2.1.1 Uniform Saturation Distribution (Effective Fluid Phase)

In this study, Biot-Gassmann relations (Gassmann, 1951) and (Biot, 1956a), (Biot, 1956b) have been used to calculate the variations in the bulk modulus during fluid substitution. However, the nature complexity and frequency dependent of the mechanichal moduli make it impractical to apply Biot-Gassmann theory directly. The reason for this is that the theory is valid under several circumstances such as isotropic medium, identical mineral composition (monomineralic), and saturated with only one single fluid phase within low frequency range.

To tackle the limitation of existing empirical studies by Biot-Gassmann, Pride (Pride, 2005) proposes the model (dynamic poroelastic models) that take into account generalized dynamic permeability. This model valid for a large range of frequencies and most consolidated rocks (Dupuy et al., 2016) (Pride, 2005). The characterization of poroelastic materials requires a homogenization approach for solid and fluid phase (Burridge & Vargas, 1979). Therefore, some averaging process is needed to compute the effective fluid bulk modulus (K_F), fluid density (ρ_F), and viscosity (η_F) of two different fluids (brine and CO_2) as given in Equations (2.1), (2.2), (2.3).

The fluid bulk modulus K_F is estimated through the equation proposed by Brie et al. (Brie et al., 1995)

$$K_F = (K_W - K_{CO2})S_W^e + K_{CO2} \tag{2.1}$$

The Brie exponent (e) associated with different mixture trend. If e equal to 1, equation (2.1) becomes Voigt average and suggests a patchy mixing fluid distribution. For large e ($e=40$), the velocity is close to that for homogeneous saturation (well mixing fluid saturation). For brine and gas mixture, Brie proposed e equal to 3 (Brie et al., 1995) and Carcione proposed e equal to 5 (Carcione, Picotti, Gei, & Rossi, 2006). In this study, two cases have been proposed. First case is to invert e and fluid saturation simultaneously and the second is by defining e and invert saturation.

2. Theory

The effective fluid density is expressed as a weighted average using the volume fraction of each fluid as given in Equation (2.2), where (ρ_W) and (ρ_{CO2}) are fluid density for brine and CO_2, respectively. S_W is brine saturation, such that:

$$\rho_F = S_W \rho_W + (1 - S_W)\rho_{CO2} \tag{2.2}$$

The effective fluid viscosity (η) of two phases (brine and CO_2) is calculated using equation proposed by Teja and Rice (Teja & Rice, 1981)

$$\eta_F = \eta_{CO2}\left(\frac{\eta_W}{\eta_{CO2}}\right)^{(1-V_{CO2})} \tag{2.3}$$

Where η_{CO2} and V_{CO2} denote viscosity and the volume of CO_2, respectively. η_W is brine viscosity.

The density of the porous medium (bulk density) is the arithmetic mean of the fluid and solid phases weighted by their own volumes via the porosity (ϕ) :

$$\rho = \phi\rho_F + (1 - \phi)\rho_S \tag{2.4}$$

Where (ρ_S) and (ρ_F) are grain density and effective fluid density. The effective fluid density (ρ_F) is calculated using Equation (2.2), while the grain density (ρ_S) is computed based on minerals composition in Utsira sandstone. The mineral density and composition of Utsira sandstone is given in Appendix A.

The mechanical moduli are composed by three poroelastic incompressibilities moduli: the undrained bulk modulus K_U, Biot's modulus C ,fluid storage parameter M and one shear modulus G. These parameters can be adapted to various models such as saturated, partially saturated or double porosity media (Dupuy & Stovas, 2014). The introduction of these parameters make it possible to explicitly describe the homogenized porous medium through the Gassmann relations (Dupuy et al., 2016) (Pride, 2005), where the modulus K_U, C, M are expressed in terms of K_D, K_S, K_F as given in Equations (2.5), (2.6), (2.7)

$$K_U = \frac{\phi K_D + (1 - (1 + \phi)K_D/K_S)K_F}{\phi(1 + \Delta)} \tag{2.5}$$

$$C = \frac{(1 - K_D/K_S)K_F}{\phi(1 + \Delta)} \tag{2.6}$$

$$M = \frac{K_F}{\phi(1 + \Delta)} \tag{2.7}$$

where Δ is a dimensionless parameter defined as

$$\Delta = \frac{1 - \phi}{\phi}\frac{K_F}{K_S}\left(1 - \frac{K_D}{(1 - \phi)K_S}\right) \tag{2.8}$$

The moduli K_D, K_S and K_F are frame bulk modulus, grain bulk modulus, and fluid bulk modulus, respectively. Porosity, ϕ, is the ratio of void space and total volume in a solid matrix and the grain bulk moduli, K_S is bulk moduli for grain.

The frequency dependent dynamic permeability is used to correct the seismic permeability and differentiate the viscous and inertial predominant effects at low and high frequency domain (Dupuy et al., 2016) (Johnson, Koplik, & Dashen, 1987). This term is expressed as:

$$k(\omega) = \frac{k_0}{\sqrt{1 - \frac{1}{2}i\frac{\omega}{\omega_c} - i\frac{\omega}{\omega_c}}} \tag{2.9}$$

Where parameters ω and ω_c are the angular frequency and critical angular frequency or maximum attenuation. Parameter k_0 is defined as effective hydraulic permeability, and i is the complex number. The characteristic of ω_c make it possible to separate the low frequency where viscous effects are dominant from the high frequency where inertial effects prevail (Dupuy et al., 2016) (Biot, 1956a).

The flow resistance $\tilde{\rho}(\omega)$ can be calculated using Equation (2.10). The term flow resistance density is introduced here to describe the intrinsic scattering of dynamic energy loss due to frequency dependent fluid flow (Biot, 1956b).

$$\tilde{\rho}(\omega) = \frac{i\eta}{\omega k(\omega)} \tag{2.10}$$

At this point, it is possible to compute the effective seismic properties (compressional and shear wave velocities and quality factors). First, the auxiliary parameter need to be defined to compute the complex slowness for compressional and shear wave (Equation 2.14). At the second step, the slowness for S-wave and P-wave are estimated using Equation (2.11) and (2.12). The phase velocity (V) as a function of angular frequency (ω) can be computed by taking the real part of the corresponding slowness as given in Equation (2.13).

$$S_S^2(\omega) = \frac{\rho - \rho_F^2/\rho(\omega)}{G} \tag{2.11}$$

$$S_P^2(\omega) = \frac{\gamma(\omega)}{2} - \frac{1}{2}\sqrt{(\gamma)^2(\omega) - \frac{4\rho\tilde{\rho}(\omega) - \rho_F^2}{HM - C^2}} \tag{2.12}$$

$$V_{P,S}(\omega) = \frac{1}{Re(S_{P,S}(\omega))} \tag{2.13}$$

where the auxiliary parameter $\gamma(\omega)$ and parameter H are given as:

$$\gamma(\omega) = \frac{\rho M + \tilde{\rho}(\omega)H - 2\rho_F C}{HM - C^2} \tag{2.14}$$

$$H = K_U \frac{4}{3}G \tag{2.15}$$

There is the third wave known as slow P-wave or Biot-wave which describes the differential motion due to the interaction between the frame and the fluid phase (Mavko, Mukerji, & Dvorkin, 1998). However, the Biot slow wave velocity and quality factors cannot be extracted from classical seismic records (Dupuy et al., 2016). Therefore, they are not used in this study.

2.1.2 Archie's Model of Resistivity

A large number of models relating brine saturation to resistivity have been developed. All these models are composed of a shale and sand term. In this study, the formation resistivity (R_T) can be expressed as a function of porosity and brine saturation according to the relationship by (Archie, 1942) :

$$R_t = \frac{R_w}{\phi^m S_w^n} \tag{2.16}$$

Where n is saturation exponent and m is cementation factor that is related to the formation factor (Adler, Jacquin, & Thovert, 1992) and to the pore tortuosities (Brown, 1980). R_W denotes brine resistivity in the reservoir. Archie's equation is essentially applicable to reservoir dominated by sandstone.

2.2 Inverse Modeling

Almost all geophysical inverse problems are nonunique and nonlinear. Non-unique means that there are more than one (infinite) model that would satisfy the observations data. The non-uniqueness in inverse modeling is caused by a number of factors such as noise on the data and the lack of data in constraining problems. Nonlinear means that the observations and the parameter of interests are such that small variations in the latter may induce large variations in the former (Sambridge, 1998). When non-linearity is taken into account, it can be useful to see the inversion process in terms of optimization in a high-dimensional parameter space (Mosegaard & Sambridge, 2002). The objective function (misfit) is then used to measures the discrepancies between observables and predictions.

In the sensitivity tests, the viscoelastic parameters (Vp, Vs, Qp, Qs, and ρ) and formation resistivity (Rt) that are derived using forward modeling become the data input to the rock physics inversion modelling to estimate poroelastic models. This process can be formulated as:

$$\mathbf{d} = \mathbf{g(m)} \tag{2.17}$$

$\mathbf{d}$, $\mathbf{m}$ and $\mathbf{g}$ are data vector, model vector, and linking function between data and model, respectively. The function $\mathbf{g}$ is a nonlinear function containing the extended Biot-Gassmann relations and Archie's formula which compute the viscoelastic and resistivity attributes in forward modelling. The inverse of $\mathbf{g}$ cannot be calculated and the solution of the system (inverse modeling) will be optimized using the global optimization method. The method is used to find the global minimum of the objective function (misfit) and avoid the local minima. The scalar misfit function C($\mathbf{m}$) can be computed using L2 norm:

$$C(\mathbf{m}) = \frac{1}{2}\left[(\mathbf{d}_{obs} - \mathbf{g(m)})^T(\mathbf{d}_{obs} - \mathbf{g(m)})\right] \tag{2.18}$$

An oriented Monte Carlo method called the neighbourhood algorithm (NA) is used to reduce the misfit function. The NA is a free derivative algorithm, contains only 2 tuneable parameters: the number of models generated for each iteration and the resampling size of Voronoi cells. At first, the algorithm generates n samples (cells) using uniform sampling

method. For each iteration, new samples are generated and guided by the low misfit area of the previous samples. Using NA, the misfit function will be reduced by concentrating sampling simultaneously in different region of parameter space (Sambridge, 1999a). For more comprehensive discussion about neighbourhood algorithm, see also (Sambridge, 1999b) .

2.2.1 One Point Inversion Formulation

In the sensitivity test, the inversion was performed to estimate one specific value of reservoir properties (one point). Figure 2.1 shows the example of one point inversion of water saturation (Sw) and Brie exponent (e) using P-wave velocity and quality factor (Vp, Qp) and S-wave velocity and quality factor (Vs, Qs) as input. In the process, an iteration number of 1000 and a resampling factor of 10 are set, generating 10000 samples for each inversion. All the samples have been plotted as a function of fluid saturation (x-axis) and Brie exponent (y-axis). Blue cross is the best model with the lowest misfit and red cross is the true value. It can be seen that the density of the samples with low misfit increases in the region around the true value (Sw = 0.2). However, the Brie exponent (e) is not well estimated because the best model ($e=\pm35$) is located far from the true value ($e=5$).
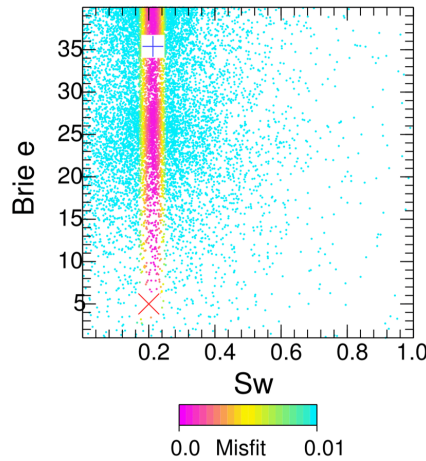
Figure 2.1: Example of one point inversion of brine saturation (Sw) and Brie exponent (e). 10000 models produced by the inversion projected onto the axes representing the brine saturation (x-axis) and Brie exponent (e) (y-axis). Blue cross is the best model with the lowest misfit and red cross is the true model. Source: (Subagjo, 2017)

2.2.2 1D Inversion Formulation

The above example showing the 1 point inversion of fluid saturation and Brie exponent (e). In the sensitivity test, true value of fluid saturation is set to be 0.2 and Brie exponent is 5. In practice, both parameters can be vary spatially inside the reservoir. In this study, 1D inversion is performed using the same inversion algorithm for 1 point inversion. However, the algorithm is adjusted to be adaptable for 1D application. To do this, the input trace is sampled every 3 meter. For each sample, we estimate the best fit model driven by the

misfit function. This process is repeated for all samples in a trace from top to base of the reservoir. The collection of samples from this estimation are then interpolated. The illustration of this process can be seen on Figure 2.2. The Vp shown here is not the actual log/trace used in this study.
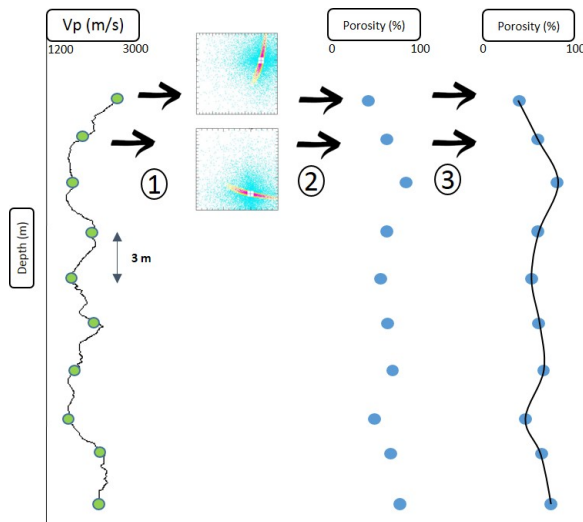
Figure 2.2: Illustration of 1D inversion of porosity from P-wave velocity. Three steps of 1D inversion including: 1) 3m sampling, 2) Model estimation for each sample, and 3) Result interpolation. The 1D profile can be in the form of log from a well or a trace from stack. The Vp shown here is not the actual log/trace used in this study.

The inversion has been run on central frequency 30 Hz. This is based on study done by (Arts et al., 2004) that shows the content of seismic data in Utsira has a bandwidth from approximately 10-70 Hz with a central peak frequency of around 30-40 Hz. Total iteration used for each inversion is 400. This number is chosen to avoid unnecessary excessive computation (Yan, 2017).

2.2.3 Uncertainty Calculation

The objective of Neighborhood Algorithm (NA) is to sample the region of parameter space that contains models of acceptable data fit (Sambridge, 1999a). The objective function (misfit) is then used to measure the deviation between observables and predictions. The 10000 models in Figure 2.3 are all computed based on the objective function (misfit) Eq.(2.18). In this example, the best fit and true models are close and the density of the samples is concentrated in the region close the true model (red cross). For one point inversion, the best fit model (blue cross) is the model with the lowest misfit function.
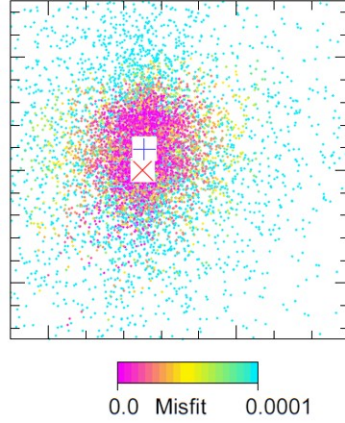
Figure 2.3: Example of 1 point inversion. Blue cross is the best model with the lowest misfit and red cross is the true value.

In geophysical inversion, it is important to have a measurement of uncertainty. In this study, the uncertainty of the inversion is analyzed by calculating the standard deviation. The standard deviation (SD) is used to quantify the distribution of a data set near to its mean value as given in Equation (2.19). This equation valid for Gaussian distribution.

$$SD = \sqrt{\frac{\sum |x - \mu|^2}{N}} \tag{2.19}$$

Where x is a value of a model, μ is the mean of the data set and N is the number of models.

In this study, the best fit model for 1D inversion is the mean of the models which the misfits are lower than 10% or 0.1. The uncertainty is then computed by calculating the standard deviation. Figure 2.4 shows the example of CO_2 saturation estimation. The blue line is the mean value of the best fit models (misfit lower than 0.1) and the dotted red line is the mean value $\pm$ standard deviation (uncertainty). Small standard deviation means small uncertainty and thus the inversion result is more confident.
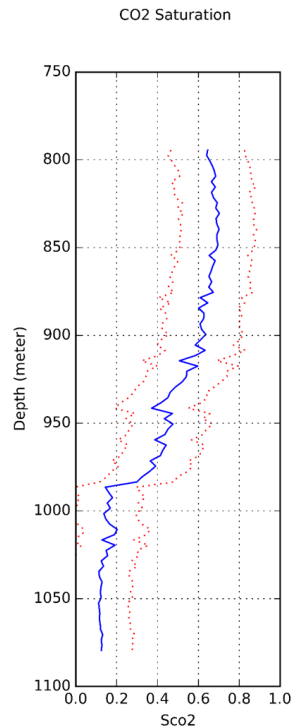
Figure 2.4: Example of 1D inversion. The blue line is the mean value of the best fit models and the dotted red line is the mean value plus minus uncertainty.

2.3   Sensitivity Tests

In the sensitivity analysis (Subagjo, 2017), the same work-flow is developed to estimate poroelastic parameters from viscoelastic seismic attributes. The effective fluid phase model plugged into extended Biot-Gassmann model is used to compute P-wave and S-wave velocity and quality factors (Vp,Vs,Qp,Qs). Brie equation (Equation 2.1) is used to calculate effective fluid bulk modulus (K_F) of two different fluid phase (brine and CO_2). Figure 2.5 shows the trade-off between P-wave velocity and fluid saturation. It shows that Brie coefficient (e) is specifying the degree of linearity between velocity and saturation. As described in forward modeling part, Brie exponent (e) refer to patchiness parameter. If e equal to 1, it associated with patchy fluid mixing, whereas high e associated with uniform (homogeneous) fluid mixing (Figure 2.5).
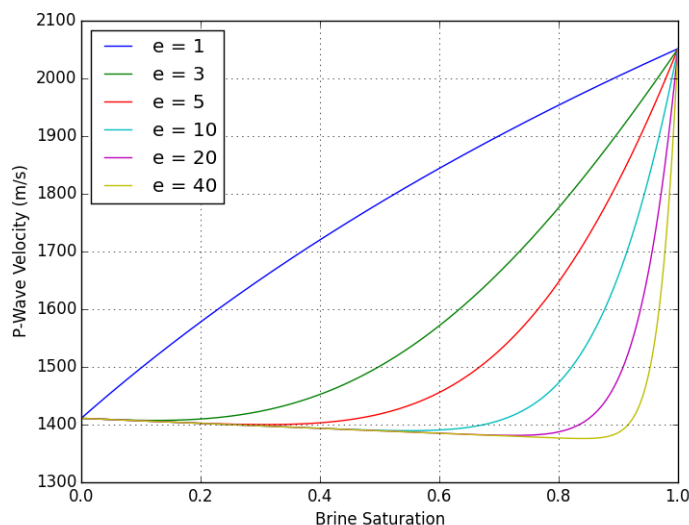
Figure 2.5: P-wave velocity versus brine saturation for different Brie exponent (e). The computed frequency is 30 Hz.

Brie exponent is conditioned by the type of fluid mixing and can vary spatially. Thus, to understand the mixing type of brine and CO_2 inside the reservoir, it is important to estimate this parameter in a proper way. Figure 2.6 shows the result of simultaneous inversion of fluid saturation (Sw) and Brie exponent (e).
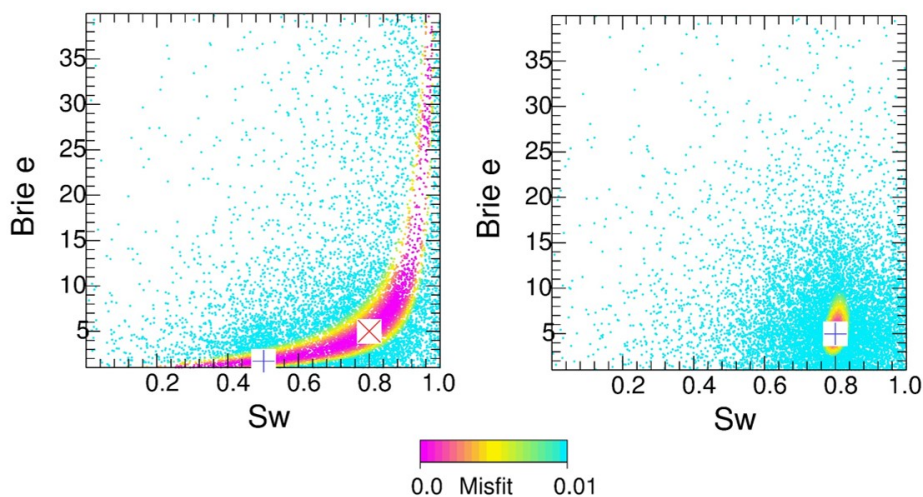
Figure 2.6: Inversion of brine saturation (Sw) and Brie exponent (e) from: Vp (left) and Vp and Rt (right). Blue cross is the best model with lowest misfit and red cross is the true model (Sw=0.8, e=5). Source: (Subagjo, 2017)

On the left, P-wave velocity (Vp) is used as input and on the right using Vp and resistivity (Rt). It is concluded from the test that resistivity attribute can be a valuable input in inversion because the best estimated model (blue cross) using Vp and Rt as input is close to the true value (Sw = 0.8 and e = 5).

In addition to that, the trade-off between resistivity and CO_2 saturation are clear. Figure

2.7 shows the correlation between resistivity derived using Archie and Indonesia model. Low brine saturation correlates to high resistivity and vice versa. In this study, only Archie model is used in the rock physics inversion.
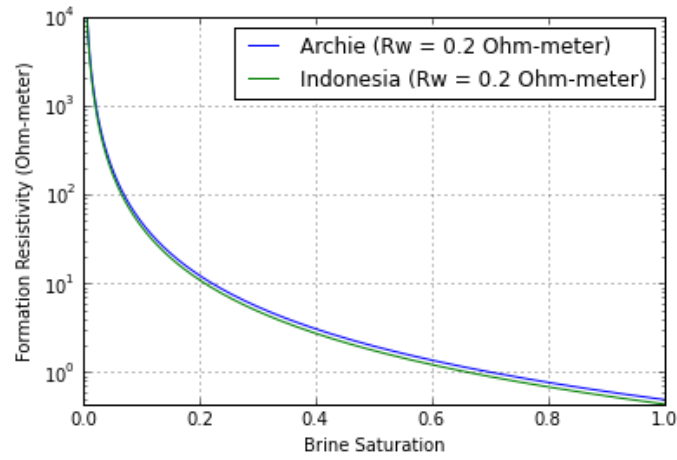
Figure 2.7: Resistivity vs brine saturation using Archie and Indonesia model. Source: (Subagjo, 2017)

3 Geological Settings and Rock Properties

The Sleipner gas field is located in the North Sea, 250 kilometers west of Stavanger. It consists of two main fields, Sleipner West and Sleipner East. Both producing gas and light oil from a reservoir at depth 2300 m. The CO_2 from both producing fields is separated, transported, and pumped back to the Utsira sandstone formation from well 15/9-A-16 which is located in Sleipner East. (Figure 3.1).
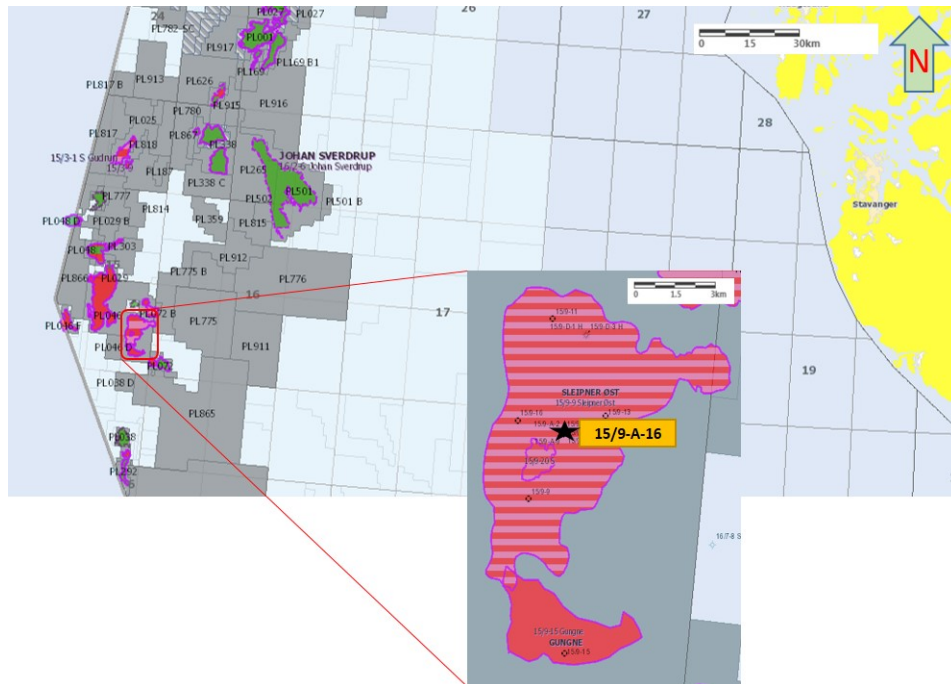
Figure 3.1: Location map of Sleipner Field (East). The red rectangle is zoomed to show the location of injection well 15/9-A-16. Source: modified from The Norwegian Petroleum Directorate (NPD).

3.1 Utsira Formation

The Utsira sand formation is a lower part of the Nordland Group, consist of a basinally deposit of late Miocene and early Pliocene age extends about 450 km from North to South and 90 km from West to East in the southern part of Viking graben – North Sea (Figure 3.2). The macroscopic and microscopic analysis of Utsira Sand show almost no signs of planar structure such as bedding planes which point to a rather chaotic deposition by turbidity currents (Lothe & Zweigel, 1999). The Utsira Sand comprises stacked overlapping 'mounds' of very low relief, interpreted as individual submarine fan-lobes and commonly separated by thin intra-reservoir mudstone or shaly horizons as described by (Chadwick et al., 2004). The isopach map (Figure 3.2) shows two maximum deposition within a sedimentary basin. One in the North where the thickness approaching 200 m and in the South where the thickness reach 300 m.
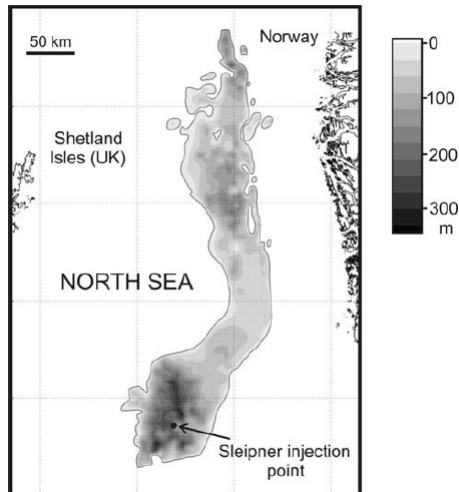
Figure 3.2: Location map of Sleipner injection point and the isopach map of Utsira sand (reservoir thickness). Source: (Chadwick et al., 2004)

The geophysical logs (gamma ray, resistivity and density) show clear boundaries on top and base of Utsira sand with clean sand dominating the reservoir (Figure 3.3). The thin intra-reservoir shale layers separate this highly porous and permeable clean sand bed. The thin shale layers characterized as spikes (peaks) by both gamma ray and resistivity logs. The thick shale is deposited in the top part of the formation, where thickness estimates vary from 4 to 7 m. The thick shale (termed 'Five Meter Shale') separates the uppermost sand unit (sand wedge) from the main reservoir beneath (Chadwick et al., 2004). These low permeability shale beds has a role on CO_2 migration path within reservoir, where it partially trap and distribute the CO_2 migration path laterally (Figure 3.4). However, these thin shale beds are difficult to discriminate from the conventional seismic reflection.

The Utsira sand is a fine-grain, weakly consolidated, highly porous (30%-40%) and very permeable (1-3 darcy) sandstone (Arts et al., 2008). The sand/shale ratio in the reservoir is generally between 0.7 and 1 (Arts et al., 2008). In Sleipner, Utsira sandstone is lying at depths between 800 m and 1100 m below sea level and dominated by quartz mineral (75%) with some feldspar (Table 3.1)

Table 3.1: Mineral percentage of Utsira sandstone based on whole-rock XRD analysis. Source: (Chadwick et al., 2004)

Mineral (%)					
Quartz	Calcite	K-Feldspar	Albite	Aragonite	Mica and Others
75	3	13	3	3	3
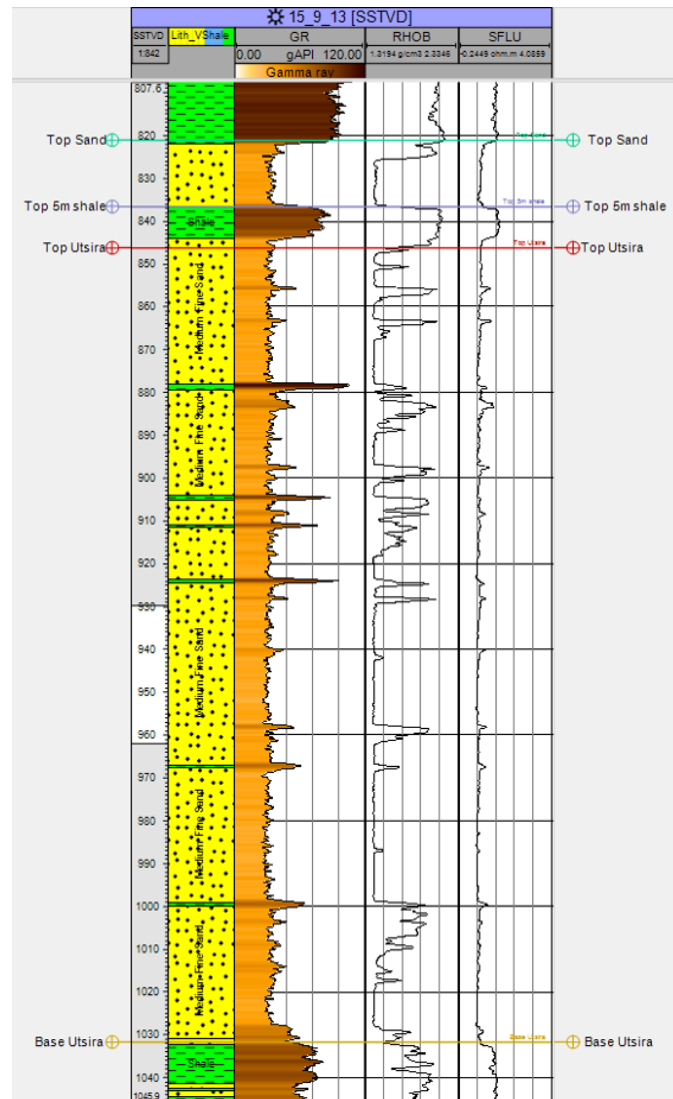
Figure 3.3: Geophysical well logs (well 15/913) at the Utsira sand. The gamma-ray(GR), density (RHOB) and resistivity (SFLU) log show peaks for intra reservoir mudstone.

3.2 Nordland Shale Group (Shale Drape)

The sealing unit of the Utsira sandstone is a shale drape, which is the lower part of the Nordland Group Shale, forms a shaly basin-restricted unit with thickness ranging between 50 and 100 m (Chadwick et al., 2000). This unit is deposited above the sand wedge or above the top of Utsira where the sand wedge is absent (R. Bøe & Zweigel, 2001). Cutting analysis show that this formation is dominated by clay and silt particle size (95%) with mineral composition comprises dominantly by Quartz (30%) and Mica (30%). The clay mineral is generally dominated by illite with minor kaolinite and traces smectite (Chadwick et al., 2004) (Table 3.2).

The XRD analysis shows that the shale drape unit has capillary entry pressures of between 2 and 5.5 MPa based on Krushin classification (Krushin, 1997). It is capable of trapping a CO_2 column several hundred metres high (Chadwick et al., 2004).

Table 3.2: Mineral percentage of Nordland Shale based on cutting analysis. Source: (Chadwick et al., 2004)

Mineral (%)						
Quartz	K-Feldspar	Calcite	Mica	Kaolinite	Smectite	Barite and Others
30	5	3	30	14	3	13

3.3 The Injection Site and Monitoring Program

The Injection is via a single deviated well (15/9-A-16), sub horizontal at the injection point which is located 1012 m below sea level, 200 m below the reservoir top (Chadwick & Eiken, 2014). The injection point is positioned below a dome of the Utsira formation, which should accordingly be filled first before CO_2 migrates laterally (Lothe & Zweigel, 1999). The storage site is considered to be a shallow depth setting for a storage environment (Chadwick et al., 2008) as the pressure and temperature conditions are likely to be close to the critical point above which CO_2 a more buoyant gas phase (Cavanagh & Haszeldine, 2014) (Figure 3.4). Due to buoyancy effects, the CO_2 from the injection point going upward to the top of the reservoir.
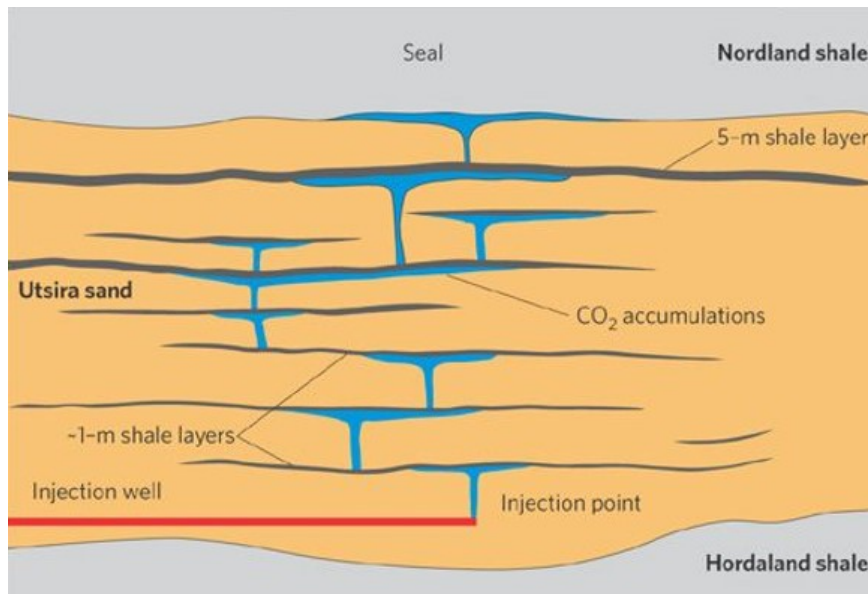
Figure 3.4: Illustration of CO_2 migration within Utsira reservoir. Source: (Bickle, 2009)

To improve the understanding of the CO_2 development inside the reservoir, several time-lapse monitoring program has been carried out at Sleipner. At Sleipner, ten 3D seismic surveys and four gravity surveys have been acquired to date (Furre et al., 2017). In 2008, A controlled source electromagnetic (CSEM) test line was acquired. None of the above monitoring technique have indicated any leakage from the Sleipner CO_2 injection site (Furre et al., 2017).

3.4 Rock-Fluids Properties as A Priori Information for Inversion

The inversion problem is non-unique. A number of possible models are estimated when data are available. It is impossible to find one unique solution for each calculation. In the sensitivity test (Subagjo, 2017), it was found that CO_2 properties are difficult to estimate when four parameters have to be inverted simultaneously. One solution is to optimize alternative information (a priori). The a priori information can be in the form of geological, geophysical, petro-physical (log) or logical information. In the inversion process, the a priori information is used as constraint to avoid the infinite numbers of possible models and to reduce uncertainty.

The grain properties for Utsira sandstone (K_S and ρ_S) are derived using Hashin Shtrikman bounds method (Hashin & Shtrikman, 1963) and volume weighted averaging method based on mineral composition in Table 3.1 and Table 3.2. The calculation is summarized in Appendix B. For simplicity, the grain properties for intra reservoir shale layers are assumed to have the same value as Nordland shale. The cementation factor is equal to 1, assuming Utsira sandstone is unconsolidated. Other a priori parameters are extracted based on the selected papers. The a priori properties of the Utsira sandstone and the Nordland shale used in the study are given in Table 3.3.

Table 3.3: The Utsira sandstone and Nordland shale grain and frame properties.

	Grain Properties		Frame Properties	
	K_S	ρ_S	m	k0
	(GPa)	(kg/m^3)	Cementation Factor	(m^2)
Utsira Sandstone	39.29	2663.5	1	2×10^{-12}
Nordland Shale	22.6	2390	1	1.47×10^{-17}
Source	Hashin Shtrikman	Volume Weighted Average		(Boait et al., 2012)

The reservoir properties used for resistivity modeling (Archie model of resistivity) are prepared from realistic petrophysical and idealized structural input. The resistivity parameters for Utsira sandstone are taken from (Bhuiyan et al., 2012).

Table 3.4: Reservoir parameters for resistivity modeling. Source: (Bhuiyan et al., 2012)

	Grain Properties	
R_W	n	m
(Ωm)	Saturation Exponent	Cementation Factor
0.2	2	1

In the reservoir, small changes in temperature and pressure conditions cause a significant CO_2 property changes which lead to large velocity and density changes (Ghaderi &

Landrø, 2009). The temperature in Utsira sandstone is ranging between 27°-37° C and the pressure vary from 8 Mpa at the top of reservoir to 11 MPa at the bottom (Furre, A.Kjær, & Eiken, 2015), (Furre & Eiken, 2014), (Ghaderi & Landrø, 2009). The fluid properties are summarized in Table 3.5.

Table 3.5: Fluid properties of brine and CO_2

	η (Pa.s)	ρ_f (kg/m^3)	K_f (GPa)
	Fluid Properties		
Brine	6.9×10^{-4}	1030	2.3
CO_2	6×10^{-5}	700	0.075
Source	(Yan, 2017)	(Furre & Eiken, 2014) (Furre et al., 2015)	(Lindeberg, 2013)

A priori information is also used to limit the range of possible solutions from inversion. For example, neutron porosity (NPHI) log from well 15/9-13 is used to limit the range porosity from inversion between 0% to 45%.

4 Data and Research Methodology

Two seismic surveys were acquired before (1994 vintage) and after the CO_2 injection (2008 vintage), while CSEM survey was acquired in 2008. Figure 4.1 shows the location of CO_2 plume in the top layer interpreted from conventional seismic reflection in 2008 (green cube). Two 2D lines (Inlines 1838 and 1874) were extracted from the 3D seismic cube and full waveform inversion (FWI) was applied to derive high-resolution velocity models (Romdhane & Querendez, 2014). CSEM inversion was used to derive resistivity model (L. Z. Bøe, Park, Vöge, & Sauvin, 2017).
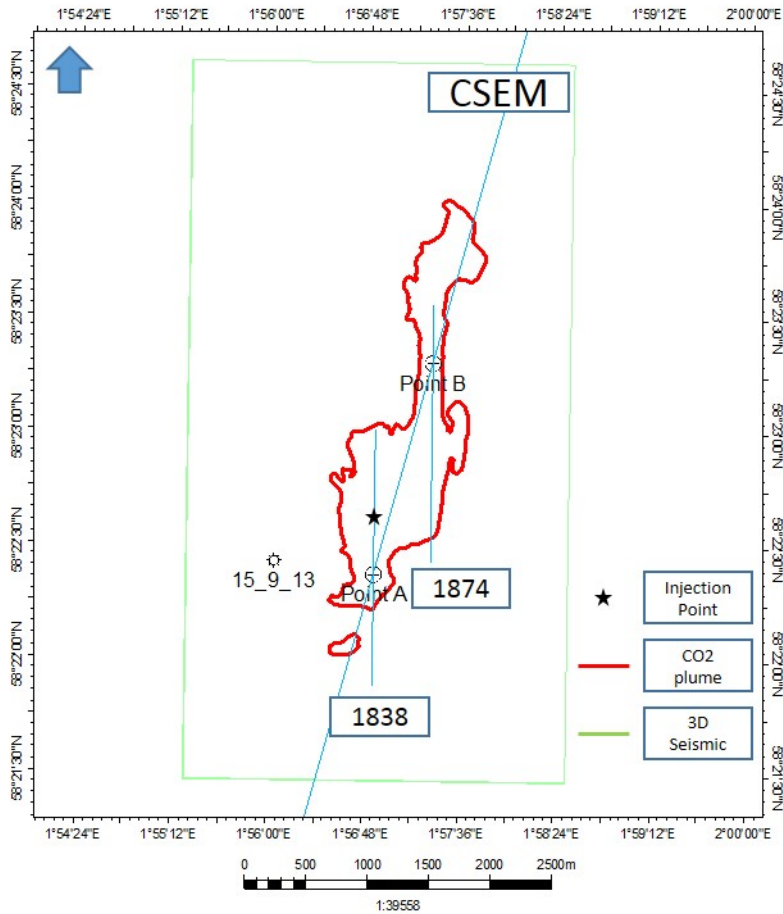
Figure 4.1: Basemap of the target area with seismic and EM lines. The study is focused at inline 1838 and 1874. Well 15/9-13 is used to define a priori grain properties

Points A and B are the intersection points of the velocity and resistivity model. The distance betwen point A and B is 1784 m. The CO_2 shown in Figure 4.1 (red line) was interpreted in 2008 at layer 9 (BIGCCS, 2008), which is the uppermost layer of the Utsira Sand. Well 15/9-13 is located 816 m on the west of point A and the distance between inline 1838 and 1874 is 450 m. The Injection point is located 433 m on the North of point A and 1380 m South West of Point B. The 2D section of resistivity model from CSEM line inside the 3D seismic cube is shown in Figure 4.2.
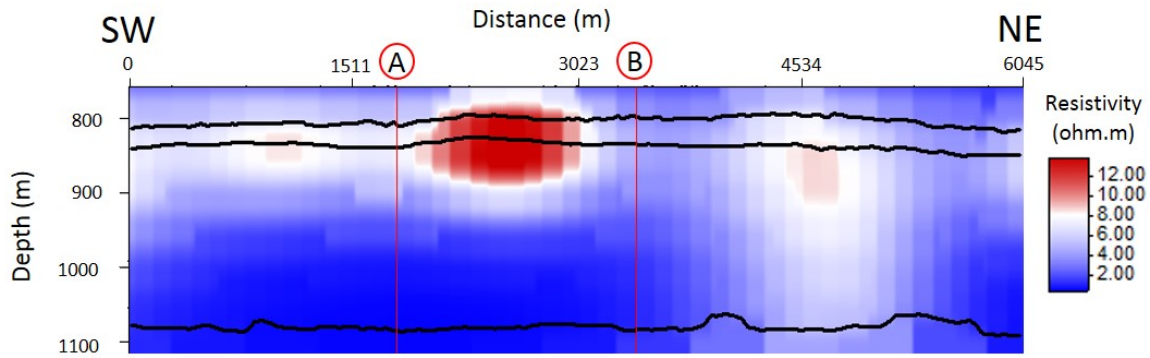
Figure 4.2: 2D section of resistivity model from CSEM. Points A and B are the intersection of CSEM line with inline 1838 and 1874, respectively (L. Z. Bøe et al., 2017)
.

4.1 Methods and Limitations

Three horizons have been interpreted in this area which are Top Sand Wedge, Top Utsira, and Base Utsira (BIGCCS, 2008). The workflow of the study is summarized in Figure 4.3. First, V_{shale} from well 15/9-13 is propagated to the 3D seismic cube (green line, Figure 4.1). The seismic data that is used is post-stack depth migrated (PSDM) seismic volume covering an area of 18.15 km^2. The V_{shale} is used to calculate grain bulk modulus (K_S), grain density (ρ_S), and permeability (k0). These properties, together with known fluid properties, will be used as a priori to invert the frame properties. The frame properties (K_D, G_D, and porosity ϕ) of the reservoir are inverted using P-wave velocity model derived by FWI before CO_2 injection (1994 vintage). These three parameters are assumed to be not affected by the CO_2 injection and used as a priori to invert fluid saturation and Brie exponent (e). For monitoring, the inversion used combination of P-wave velocity and resistivity model after injection (2008 vintage).
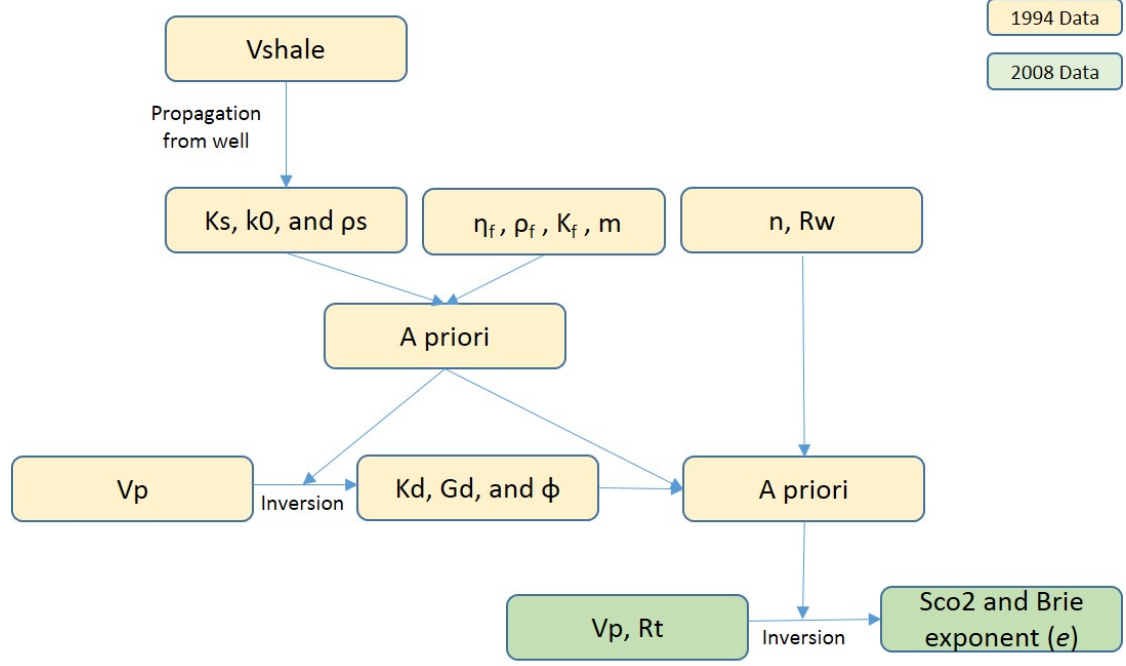
Figure 4.3: Study work-flow for 1D and 2D inversion

The effective grain bulk modulus (K_S), grain density (ρ_S), and permeability (k0) are computed using arithmetic average over values in shale and sand (Equation 4.1, 4.2, 4.3). These parameters will be used as a priori for the inversion:

$$K_S = (V_{\text{shale}})K_{\text{shale}} + (1 - V_{\text{shale}})K_{\text{sand}} \tag{4.1}$$

$$\rho_S = (V_{\text{shale}})\rho_{\text{shale}} + (1 - V_{\text{shale}})\rho_{\text{sand}} \tag{4.2}$$

$$k0 = (V_{\text{shale}})k0_{\text{shale}} + (1 - V_{\text{shale}})k0_{\text{sand}} \tag{4.3}$$

Where K_{shale}, K_{sand}, ρ_{shale}, and ρ_{sand} are the bulk moduli and densities of shale and sand fractions calculated using Hashin-Shtrikman method (Hashin & Shtrikman, 1963), (Mavko et al., 1998) (Appendix B). The grain and frame properties for clean sand (Utsira sand) and shale (Nordland shale) are given in Table 3.3. The intersection points of the velocity and resistivity lines (points A and B) are used as location for 1D inversion. However, there are several data limitations that have to be pointed out.

1. The logging activity from well (15/9-13) was conducted before CO_2 injection.

2. CSEM survey was acquired after CO_2 injection (2008).

3. The resistivity model derived from CSEM line is not in the same inline as velocity model from FWI lines.

There is a subtle difference to the work-flow in sensitivity tests (Subagjo, 2017). In this study, joint rock physics inversion is focused on the combination of P-wave velocity (Vp) and resistivity (Rt) as input. Due to the difference location of resistivity and velocity model, the 1D profile of resistivity at points A and B are propagated toward inline 1838 and 1874.

4.2   3D petrophysical and resistivity model

A geological model for Sleipner area is generated to obtain a V_{shale} 3D model. The grid resolution for the model is 25 m x 25 m. The V_{shale} is populated using V_{shale} log from well 15/9-13. Four horizons are interpreted and used as lithological constraints to propagate the petrophysical property (shale volume, V_{shale}) from well 15/9-13 to the entire seismic cube. This model is made under assumption that lateral changes inside reservoir is small. 3D model of V_{shale} at Utsira sandstone used in this study is shown in Figure 4.4.
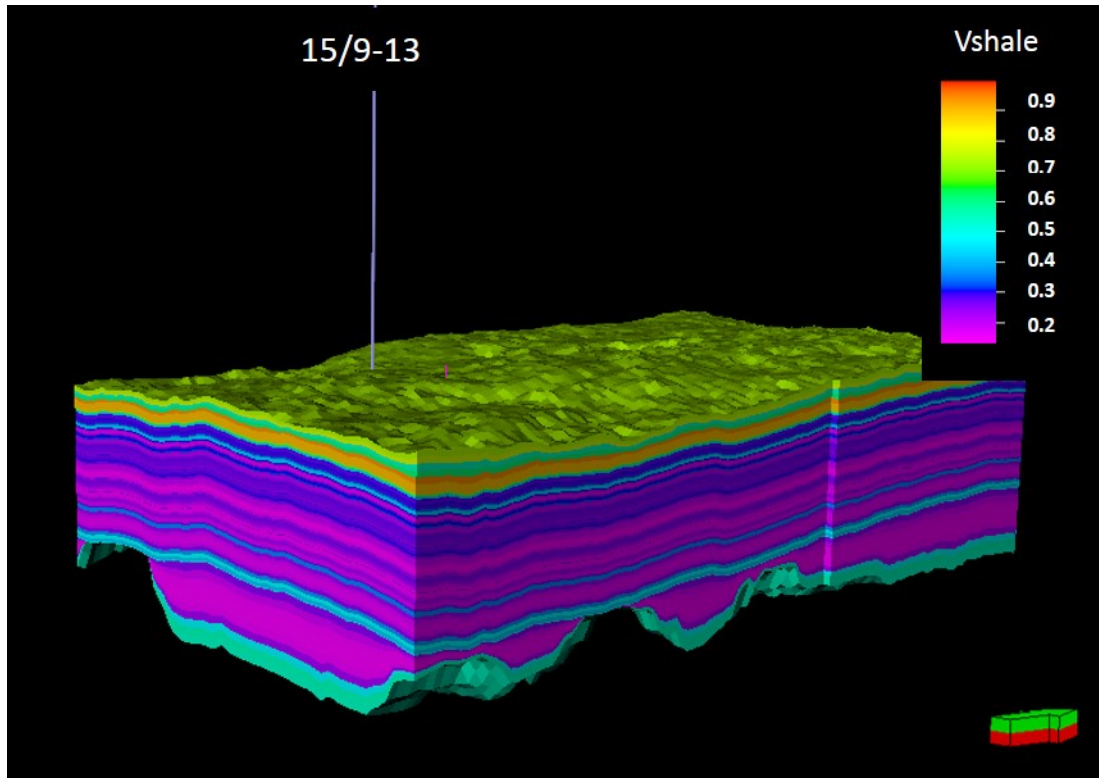
Figure 4.4: 3D model of V_{shale} at Utsira sandstone. The interpreted horizons are used as constraints to propagate the petrophysical property (V_{shale}) from well 15/9-13.

To build 3D resistivity model of the study area, the same grid as V_{shale} 3D model is used and two stages are performed to propagate the resistivity. First, the background resistivity (before injection) model is generated by using deep resistivity data (ILD) from well 15/9-13 before injection. The properties from ILD log are distributed following the layers from interpreted horizons to the entire cube. This background resistivity model is created under assumption that lateral change inside the reservoir is small and the reservoir is filled with brine (Figure 4.5). Outside the Utsira sandstone (Nordland and Hordaland shale), only one layer is specified and the resistivity is set as constant based on value from ILD log (average value in that layer).
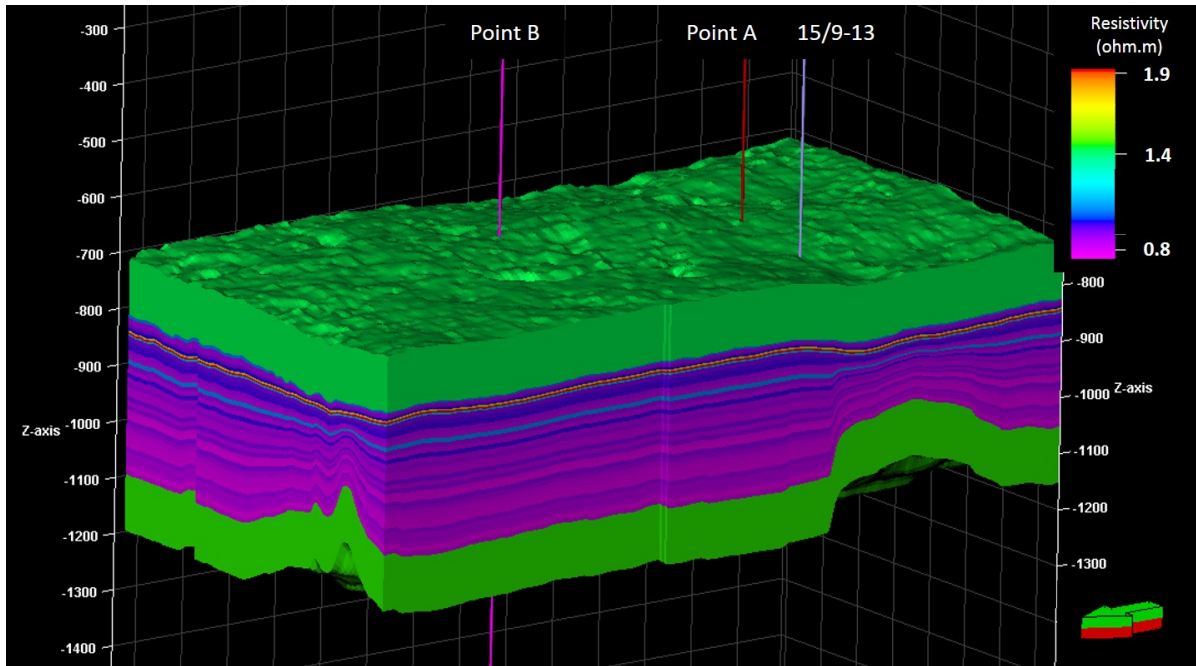
Figure 4.5: 3D model of background resistivity at Utsira sandstone. The interpreted horizons are used as constraint to propagate the petrophysical properties (ILD) from well 15/9-13. Outside the Utsira sandstone the resistivity value is set as constant (green color).

In the next step, the geobody of the CO_2 plume are extracted from 2008 seismic data using industry-based software Petrel®. The difference with the first model is that the resistivity is not propagated from ILD log at well 15/9-13. Here, the resistivity is propagated from points A and B which derived from CSEM line (Figure 4.2). The resistivity at point A and point B are propagated inside the geobody using Gaussian random function simulation (Figure 4.6). This model is made under assumptions that the geobody is filled with CO_2 and brine. Outside of the geobody, the resistivity is set as zero.
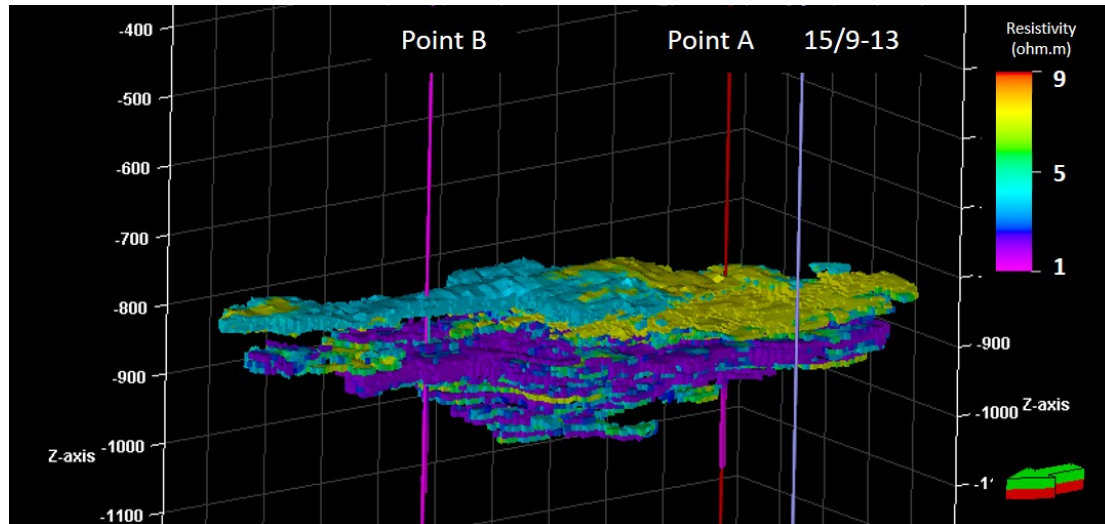
Figure 4.6: 3D model of resistivity at interpreted CO_2 plume. The CO_2 plume is interpreted by extracted the geobody using Petrel®. Outside this plume, the resistivity is set as zero.

The resistivity model inside CO_2 geobody is merged with the background resistivity derived in the first step. The merging process is done by summing both resistivity models (Fig.4.5 and Fig.4.6) so that the resistivity value inside the geobody is kept while outside this area, the background resistivity is used. Resistivity at inlines 1838 and 1874 are sliced from this 3D cube and smoothing technique have been performed to derive more realistic resistivity response. In this study, smoothing technique has been done using the Seismic Unix utility smooth2 (Stockwell, 2001). Smoothing for 1D profile is done in vertical direction (z-axis) while for 2D is done in both vertical and horizontal (x-axis) directions.

4.3 1D and 2D seismic and resistivity data

In this part, 1D and 2D sections of velocity and resistivity are presented. The basemap can be seen in Figure 4.1 and this study is focused in reservoir area (Utsira sandstone) which thickness is approximately between 200-300 meter (Chadwick et al., 2004). Three horizons have been interpreted in both lines. In this study, the five meter shale layer is interpreted to be one single body with the sand wedge.

4.3.1 Baseline (1994 vintage)

To reduce the time consumption during inversion, only 700 offsets are selected from a single inline. The distance between offsets is 3 meter so the total length for each selected region is 2100 meter (Figure 4.1). The inversion is performed from depth 745 meter to 1195 meter (± 50 meter above interpreted Top Sand Wedge and 120 meter below Base Utsira).

The 2D sections of velocity model before injection are shown in Figures 4.7 and 4.8 for inline 1838 and 1874, respectively. Point A, which is the intersection of inline 1838

and CSEM line is located at x = 2436 m, while point B is located at x = 3841 m of inline 1974 (red vertical line, Fig. 4.7 and 4.8)
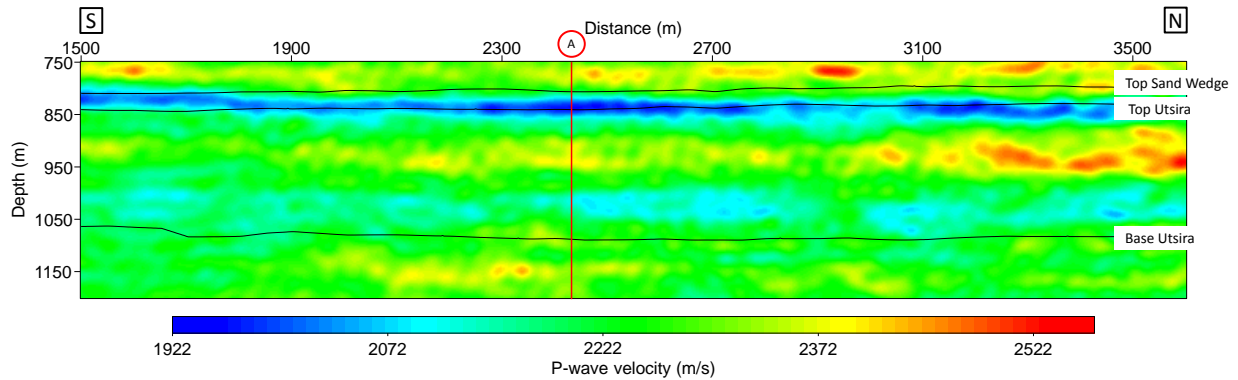
Figure 4.7: 2D section of Vp at inline 1838 before CO_2 injection (1994 vintage). Point A is at x = 2436 m. Three horizons are interpreted which are Top Sand Wedge, Top Utsira, and Base Utsira.
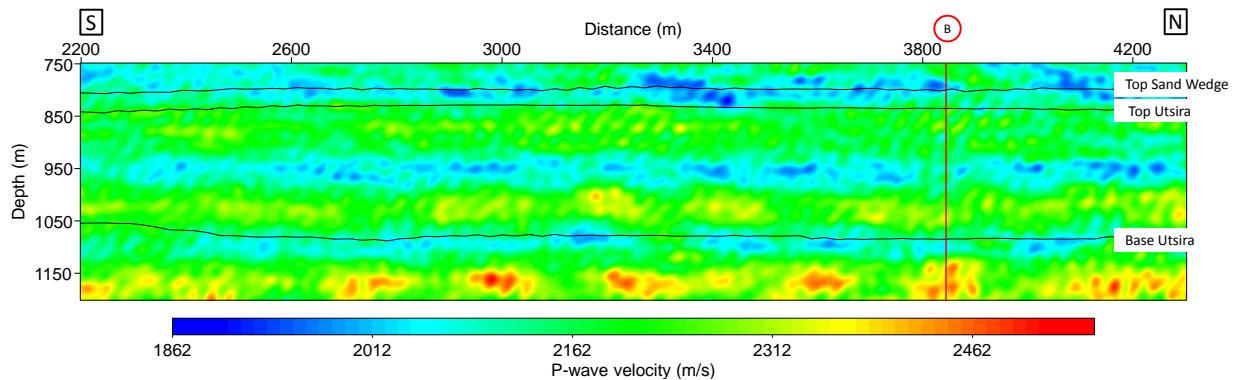
Figure 4.8: 2D section of Vp at inline 1874 before CO_2 injection (1994 vintage). Point B is at x = 3841 m. Three horizons are interpreted which are Top Sand Wedge, Top Utsira, and Base Utsira.

4.3.2 Monitor (2008 vintage)

In addition to P-wave velocity (Figure 4.9 for inline 1838 and Figure 4.10 for inline 1874), resistivity is derived from CSEM line (Figure 4.2). 1D trace of Point A and Point B are extracted and are given in Figure 4.11. As explained, 1D profiles are used to propagate the resistivity model toward inlines 1838 and 1874. The 2D resistivity models are shown in Figure 4.12 for inline 1838 and Figure 4.13 for inline 1874.
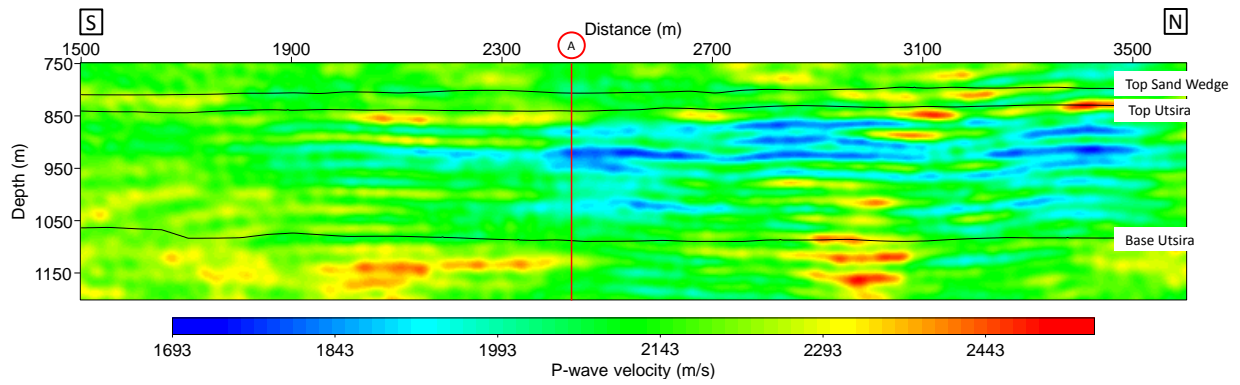
Figure 4.9: 2D section of Vp at inline 1838 after CO_2 injection (2008 vintage). Point A is at x = 2436 m. Three horizons are interpreted which are Top Sand Wedge, Top Utsira, and Base Utsira.
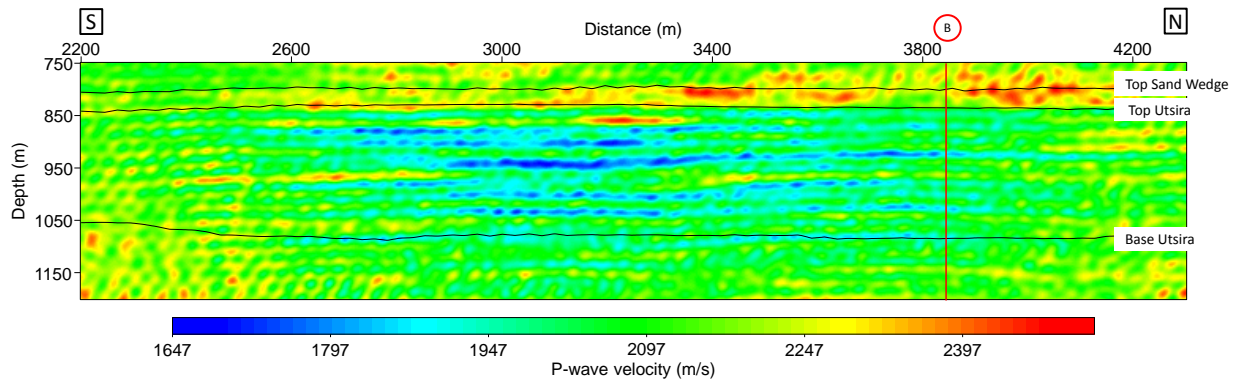
Figure 4.10: 2D section of Vp at inline 1874 after CO_2 injection (2008 vintage). Point B is at x = 3841 m. Three horizons are interpreted which are Top Sand Wedge, Top Utsira, and Base Utsira.
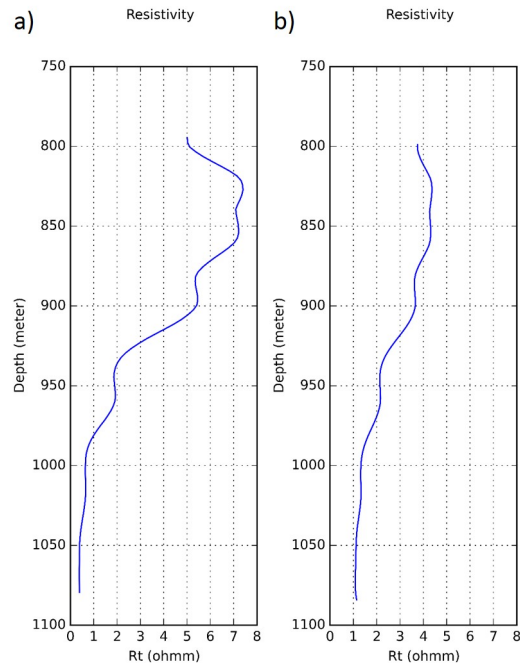
Figure 4.11: 1D profiles of resistivity model a t (a) point A and (b) point B.
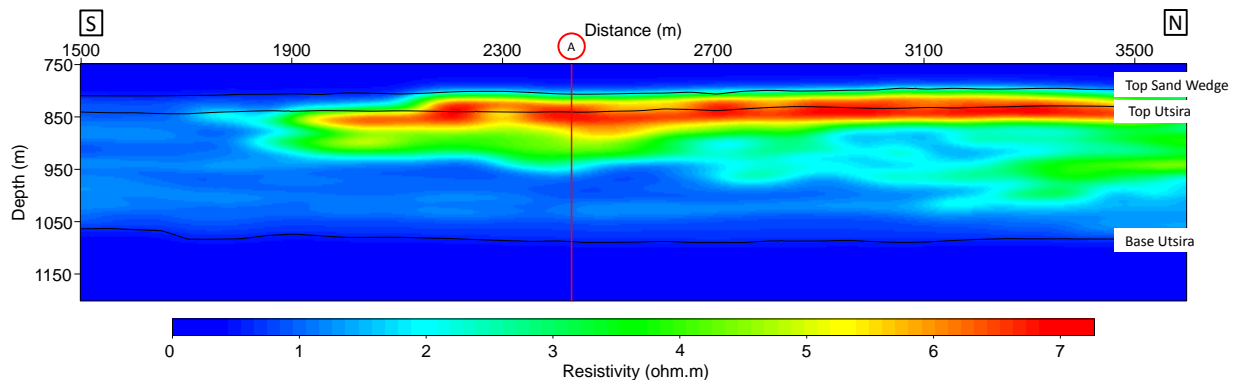
Figure 4.12: 2D section of resistivity at inline 1838 after CO_2 injection (2008 vintage. Point A is at x = 2436 m. Three horizons are interpreted which are Top Sand Wedge, Top Utsira, and Base Utsira.
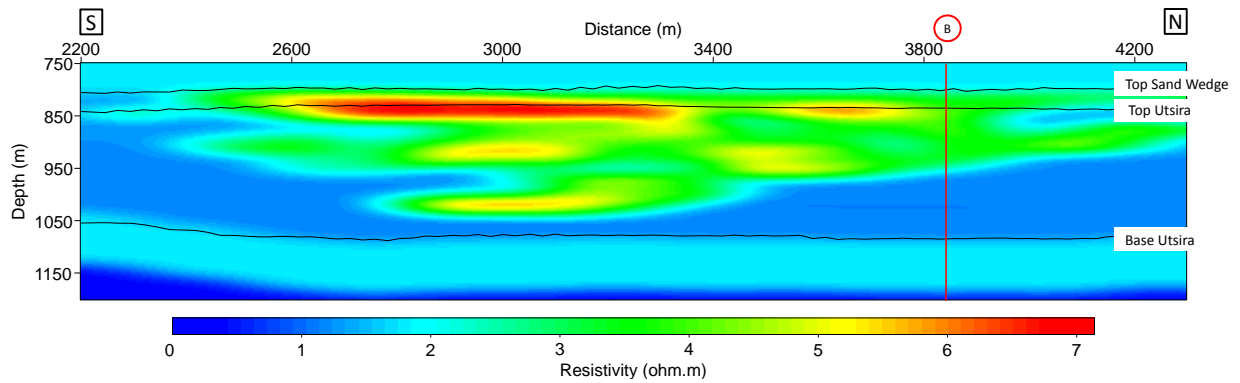
Figure 4.13: 2D section of resistivity at inline 1874 after CO_2 injection (2008 vintage). Point B is at x = 3841 m. Three horizons are interpreted which are Top Sand Wedge, Top Utsira, and Base Utsira.

For 2D inversion, the geometrical size of 2D resistivity model is made identical to P-wave velocity model. Total 700 offsets from depth 745 m to 1195 m are sliced from the 3D model at the same location as P-wave velocity model.

5 Results

Interpretation for 1D profile is focused in point A. Moreover, for 2D line, the interpretation is focused at inline 1838. For the sake of brevity, some figures are given in Appendix. Uncertainty in 1D profile is shown in dotted line.

5.1 1D Inversion

The input for inversion are the combination of P-wave velocity (Vp) and resistivity (Rt). It is not possible to observe the resistivity changes caused by CO_2 because the CSEM survey was acquired only after the injection. So, the effect of CO_2 can be observed by comparing the P-wave velocity before and after the injection.

P-wave velocity (Vp) decreases significantly after CO_2 injection. Figure 5.1a shows a major decrease at depth 900 m to 950 m in point A. In addition, both Vp after injection in points A and B are ranging between 1900 m/s and 2100 m/s (red line). It dropped from around 2200 m/s - 2300 m/s when CO_2 was not introduced in the reservoir (blue line). The decreases of Vp caused by CO_2 have been predicted in the sensitivity test (Figure 2.5). It also shows that when CO_2 saturation is higher than 50%, the decrease of Vp is weak. In addition to that, when higher Brie exponent is chosen, Vp decreases even faster.
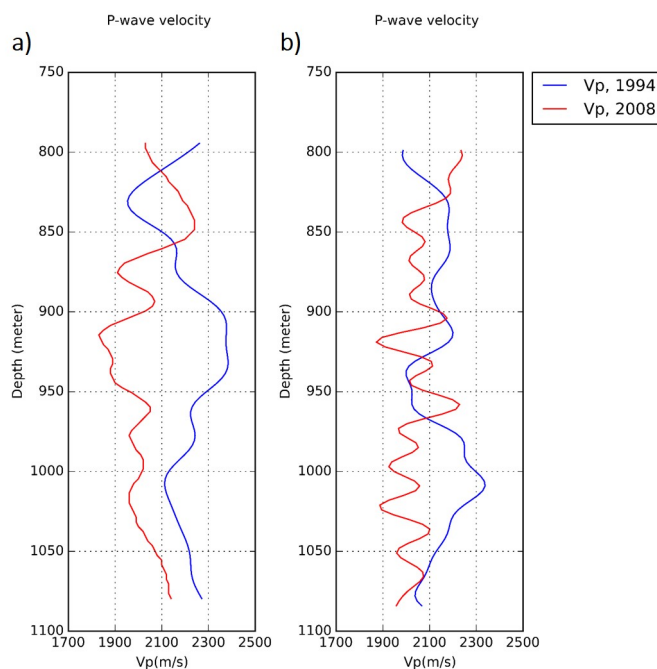
Figure 5.1: 1D profile of P-wave velocity before and after CO_2 injection at (a) point A and (b) point B. Blue line is 1D profile of Vp before injection (1994 data) and red line is 1D profile of Vp after injection (2008 data).

5.1.1 Estimation of frame moduli and porosity in Points A and B

The estimation of frame properties (drained bulk modulus K_D, drained shear modulus G_D, and porosity ϕ) are performed by using Vp obtained from FWI as input. In the inversion, the solid properties (Bulk grain moduli K_S and density ρ_S), fluid properties (fluid bulk modulus K_F, viscosity η, density ρ_F), and dynamic permeability (k0) are known. Figure 5.2 shows the 1D profile of V_{shale} at well 15/9-13 (left) and V_{shale} at points A and B (right). The interpreted horizons drive the depth and thickness of the layers which make 1D profile in point A slightly different with that in point B.

The solid properties and dynamic permeability (K_S, ρ_S, k0) are computed based on the shale content V_{shale} from well (15/9-13) using Equation (4.1),(4.2), and (4.3). Therefore, the trend of 1D profile of these parameters (Figure 5.3) is heavily influenced by the trend of V_{shale} at the well. Other a priori information can be seen in Table 3.3, Table 3.4, and Table 3.5.
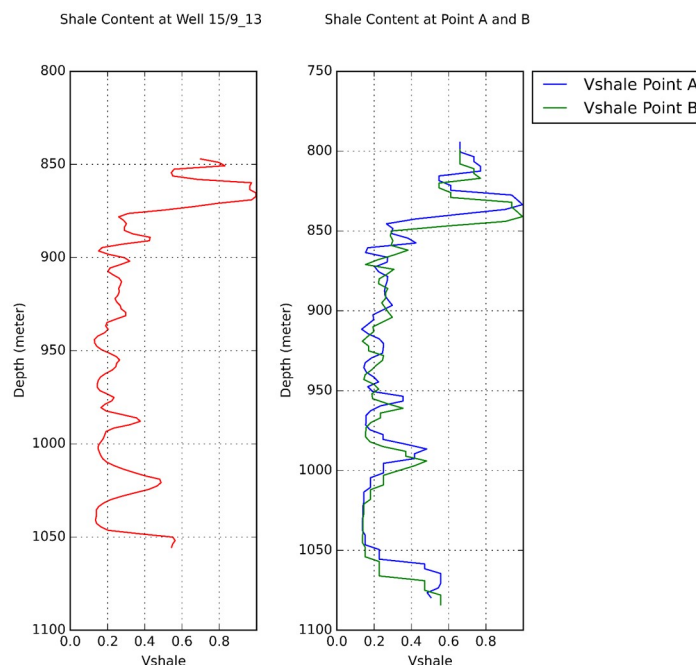
Figure 5.2: Shale content (V_{shale}) at Well (15/9-13) (red line), Point A (blue line), and Point B (green line)

Figure 5.2 shows that the five meter shale can be identified in the top of formation with the thickness varying from 6 m in the well and become thicker to the East (9 m in point B, Table 5.1). The shale content (V_{shale}) of this layer is ranging between 0.95 to 1. The corresponding layer is also observed in 1D profile of grain's Bulk modulus (K_S), density (ρ_S), and permeability (k0) in point A (Fig.5.3) and point B (Fig.5.6). Unlike the a priori information 1D profile, the five meter shale is not characterized from P-wave velocity 1D profile obtained by FWI.

Table 5.1: Horizons depth in Well 15/9-13, point A, and point B

Horizons	15/913 (m)	Point A (m)	Point B (m)
Top Sand (Wedge)	846	808	800
Top five meter shale	862	821	823
Top Utsira	868	827	832
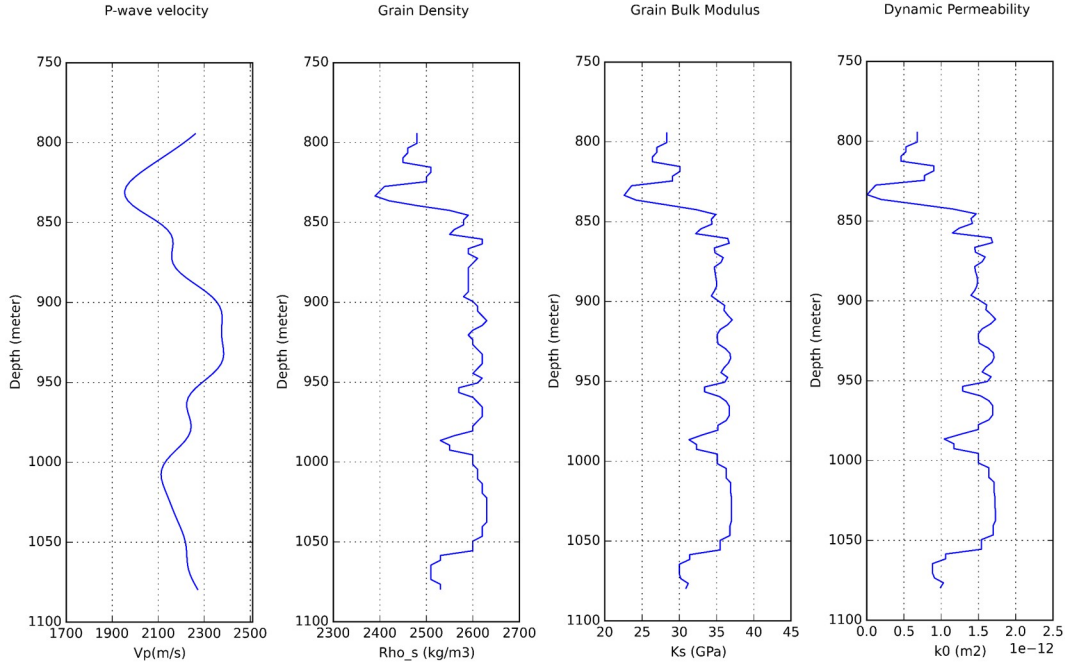
Figure 5.3: 1D profile of P-wave velocity and apriori information at Point A. The trend of ρ_S, K_S, and k0 are controlled by the trend of V_{shale} from well.

As discussed in Chapter 2, a priori information are required to limit the possible solutions from inversion. However, the inversion for baseline model is still under-determined where only one input (Vp) is used to invert three parameters (K_D, G_D, and ϕ). Figure 5.4 shows the inversion result of frame moduli (K_D and G_D) and porosity ϕ. The blue line is the mean of the best estimated models (misfit lower than 0.1) and dotted red line is the mean of best models plus/minus uncertainty. The range for porosity inversion is obtained from NPHI log from well 15/9-13, while inversion range for grain Bulk and shear modulus are taken from sensitivity test (Subagjo, 2017) and previous studies (Yan, 2017). The ranges for the inversion in the baseline model are given in Table 5.2. The five meter shale is not observed from the inversion result. There are two reasons for this. First, the input (Vp) has lower frequency (resolution) than the a priori which derived from the log. Second, the vertical sampling (3 m) cannot capture this geological event.

5. Results

Table 5.2: Inversion parameter range for K_D, G_D, and porosity

Parameters	Minimum Value	Maximum Value
Porosity, ϕ	0	0.45
Frame Bulk Modulus, K_D (Pa)	1 x 10^8	10 x 10^9
Frame Shear Modulus, G_D (Pa)	1 x 10^8	10 x 10^9
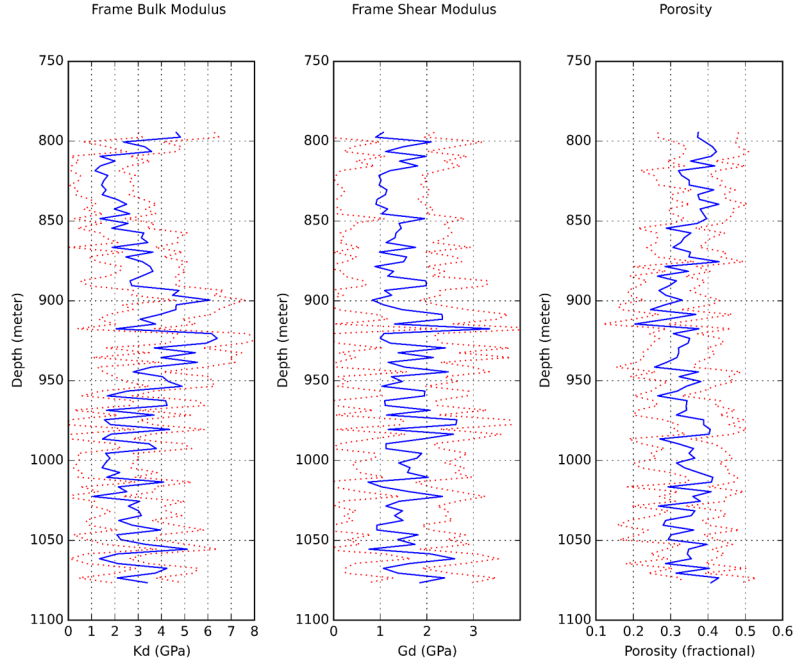
Figure 5.4: 1D profile of K_D, G_D and porosity at Point A. The dotted red line is the mean value plus minus uncertainty.

A priori information acts as constraint that reduces the non-uniqueness problem in the inversion. To see if there is strong correlation between each parameters is by plotting these parameters along two axes. Figure 5.5 shows the plot between these parameters. It is difficult to see the correlations between these properties. As discussed, these parameters will be used as a priori to constraint the inversion of saturation and Brie exponent (e) in the next step.
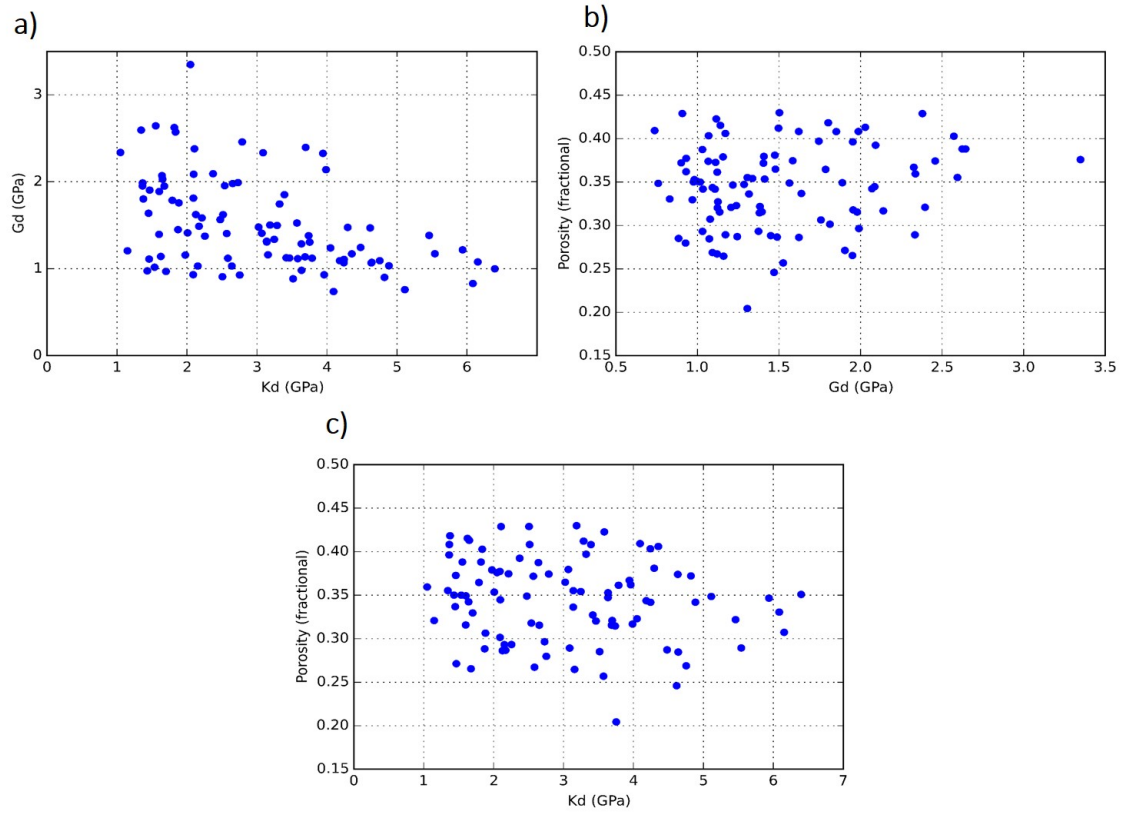
Figure 5.5: Scatter plot of 1D profile of inversion results in Point A (a) G_D vs K_D (b) ϕ vs G_D and (c) ϕ vs K_D

The same procedures is applied for point B. The 1D profiles of input (Vp), a priori information (K_S, ρ_S, k0), and the inversion result (K_D, G_D, ϕ) are given in Figure 5.6.
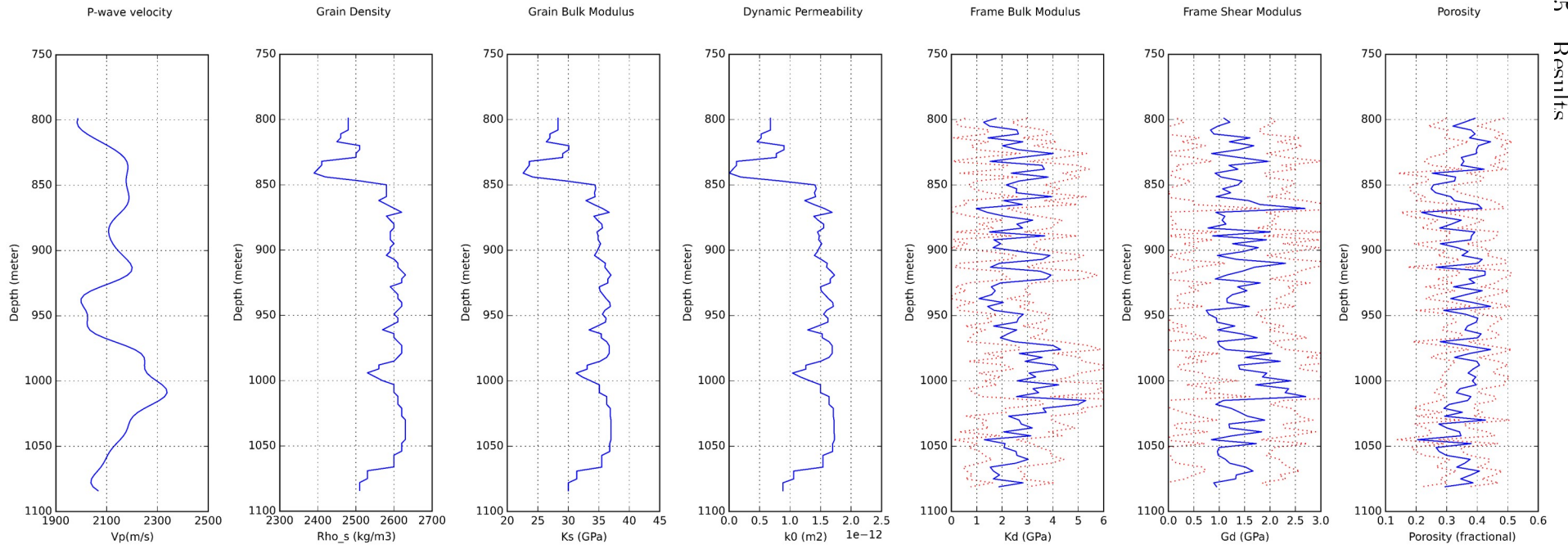
Figure 5.6: 1D profile of Vp, grain density, grain bulk modulus, permeability, and inverted porosity and K_D, G_D at Point B. The dotted red line is the mean value plus minus uncertainty.

5.1.2 Estimation of CO_2 saturation and Brie exponent (e) in Point A and B

The estimation of CO_2 saturation and Brie exponent is performed under two cases. First case is by using one input (P-wave velocity or resistivity only) and the second case is by combining resistivity (Rt) and P-wave velocity (Vp). For each case, three scenarios are applied:

1. Brie exponent is known and inverting only CO_2 saturation.

2. Inverting both CO_2 saturation and Brie exponent simultaneously.

3. Inverting porosity (ϕ) together with CO_2 saturation and Brie exponent simultaneously. In this scenario, only K_D and G_D are computed in the baseline model.

Inversion range for CO_2 saturation and Brie exponent (e) are shown in Table 5.3. Prior to inversion, the 1D profile of K_D, G_D, and ϕ are smoothed to match the resolution of the Vp obtained by FWI and Rt derived from CSEM. Smoothing is only performed to the frame moduli and porosity from inversion in the baseline model. The 1D profile of K_D, G_D, and ϕ after smoothing are shown in red line, Figure 5.7.
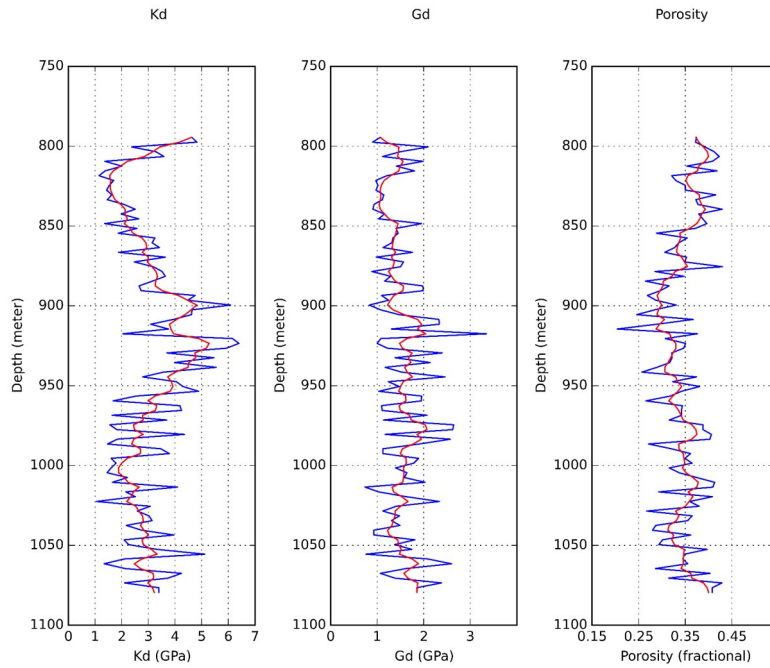
Figure 5.7: Smoothed of 1D profile of a priori at point A. Blue line are the original log from inversion and red line are the smoothed of the logs.

Table 5.3: Inversion parameter range for CO_2 saturation and Brie exponent (e)

Parameters	Minimum Value	Maximum Value
CO_2 saturation	0	1
Brie exponent (e)	1	40

Case 1 : Estimation of CO_2 saturation and Brie exponent using 1 input

Fluid properties of brine and CO_2 inside Utsira are given in Table 3.5. Reservoir parameters for resistivity modeling are given in Table 3.4 and rock frame moduli are inverted in the baseline model (smoothed, Figure 5.7). Figure 5.8 shows 1D profiles of Vp and Rt as input for inversion in point A.
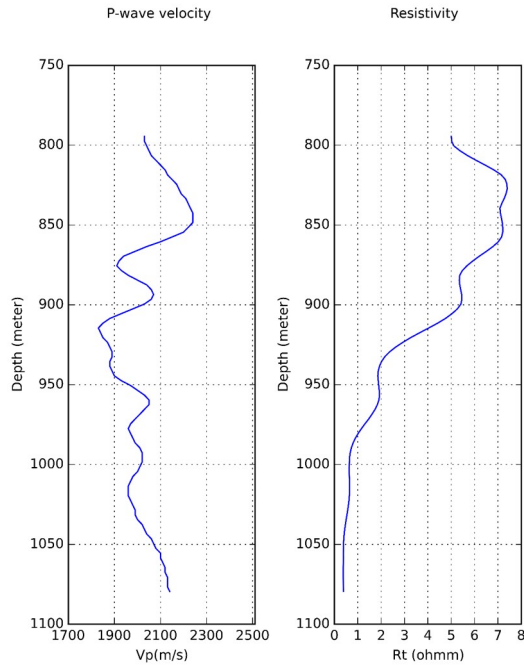
Figure 5.8: 1D profile of P-wave velocity (Vp) and Resistivity (Rt) after injection at point A.

CO_2 saturation and Brie exponent in point A are inverted simultaneously using Vp and the result is given in Figure 5.9a. Figure 5.9b is the comparison of CO_2 saturation using different Brie exponent (e equal to 1,5,40). The accumulation of CO_2 are observed at depth 800, 870, 910, 930, 970, 980, 1000, 1070 m (Fig.5.9a).
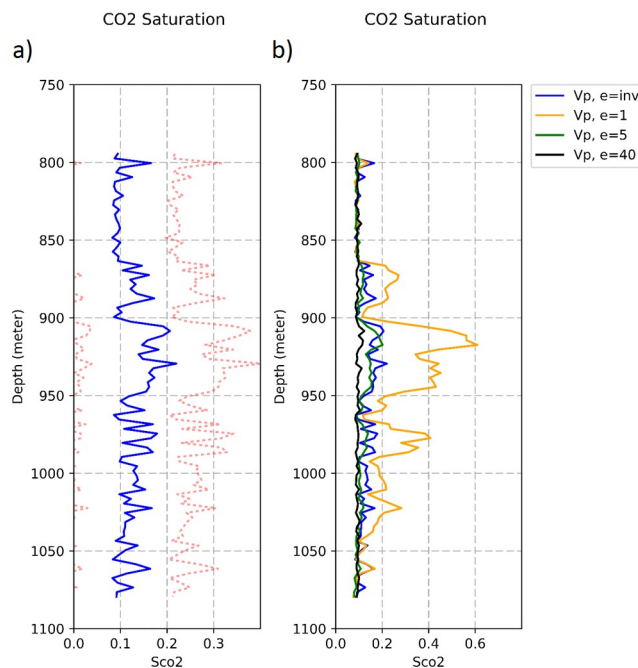
Figure 5.9: CO_2 saturation inverted from Vp at point A. (a) CO_2 saturation if inverted together with Brie exponent (e). The dotted red line is the mean value plus minus uncertainty. (b) CO_2 saturation if Brie exponent (e) is known. The CO_2 saturation in (a) is also shown here for comparison.

Figure 5.9b shows the inverted CO_2 saturation using different Brie exponent. In this scenario, Brie exponent is assumed known and the inversion system became well-determined. It shows that in uniform saturation ($e=40$) the CO_2 saturation is low, between 8%-12% for all depth. When Brie exponent is inverted jointly with CO_2 saturation, the saturation is around 10% in the upper part of the formation and go up to 21% in the middle of the formation (depth 900 m to 950 m) with uncertainty between $\pm10\%$ - $\pm25\%$. When considering full patchy mixing ($e=1$), the saturation reach $\pm60\%$ at depth 930 m. All plots in Figure 5.9b show low CO_2 saturation around depth 800 m to 860 m $\pm10\%$.

The 1D profile of CO_2 saturation when Brie exponent inverted is quite similar to CO_2 saturation when e is set to 5, implying intermediate distribution type of brine and CO_2 between uniform and patchy mixing. This is also confirmed by the Brie exponent that is inverted together with CO_2 saturation (Figure 5.10). It shows that Brie exponent varies from 6 to 20 with the mean value of around 7. However, sensitivity test (Figure 2.6) confirms that Brie exponent is not well estimated when using only Vp as input for inversion.
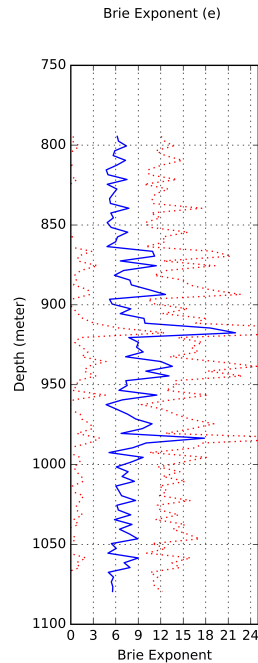
Figure 5.10: Brie exponent (e) inverted from Vp at point A. Brie exponent is inverted simultaneously with CO_2 saturation. The dotted red line is the mean value plus minus uncertainty

In the case where porosity inverted together with Brie exponent and CO_2 saturation, the inversion system becomes under-determined where Vp is used to estimate 3 parameters simultaneously. The result is not shown here for brevity and can be seen in Figure C.1 (Appendix C) To conclude, the CO_2 saturation from this case shows similar trend to the one at Figure 5.9a except at depth 925 m when CO_2 saturation reach 85%. It also shows 5% higher CO_2 saturation around depth 800 m to depth 850.

In point B, Top Utsira sand is interpreted at depth 829 m. The 1D profiles of Vp, K_D, G_D, ϕ, and inverted CO_2 saturation and Brie exponent (e) at this point are shown in Figure 5.11. The smoothed logs of a priori information (red curves, K_D, G_D, ϕ) are used in inversion. Figure 5.11 shows 12% to 17% CO_2 accumulation at the top of formation (depth 830 m to 875 m). Other CO_2 accumulation are found at depth 890, 920 and 1000 m. The CO_2 saturation reach 20% at depth 1030 m. The Brie exponent in point B varies from 5 to 14 with the mean value of around 7.
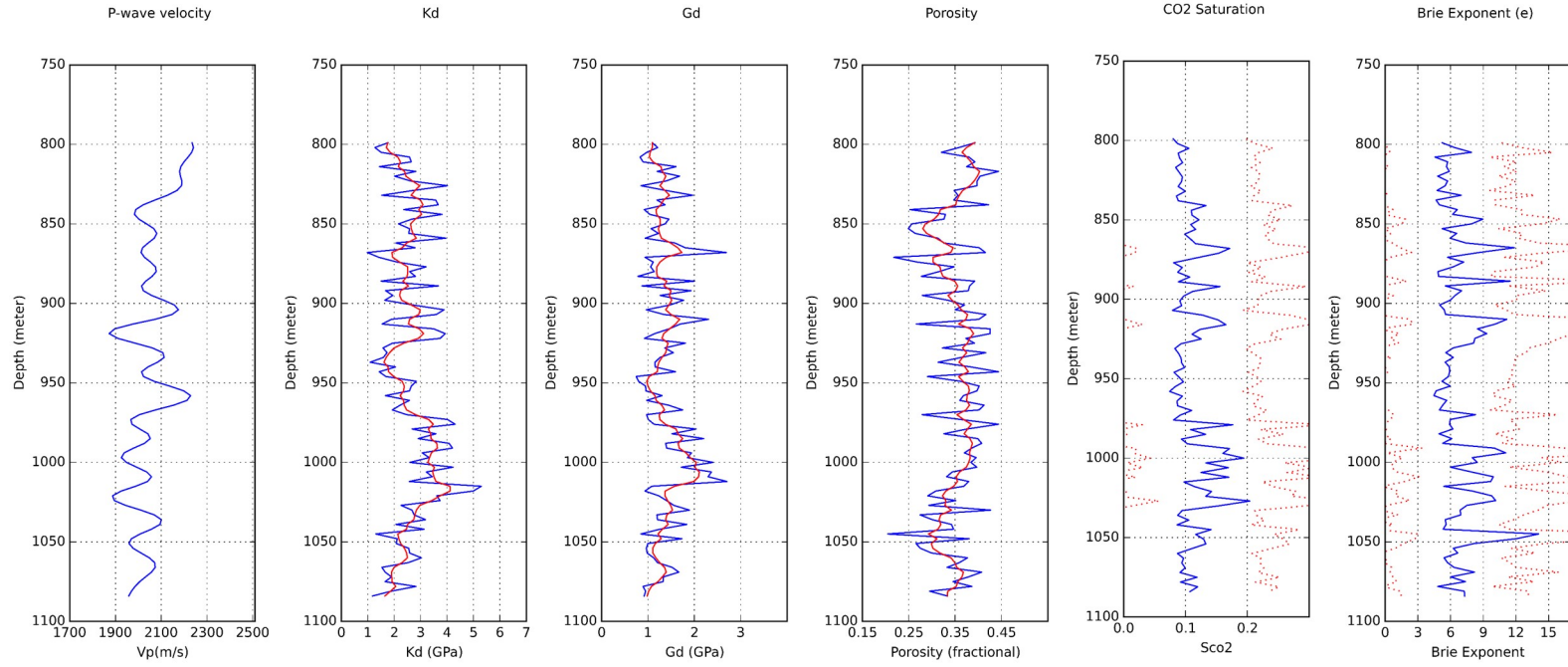
Figure 5.11: 1D profile of Vp, a priori, and inverted CO_2 saturation and Brie exponent (e) from Vp at point B. The dotted red line is the mean value plus minus uncertainty. The red line in K_D, G_D, ϕ logs are used as a priori in the inversion.

When estimating CO_2 saturation using only resistivity (Rt), the inversion system becomes well-determined. This is because resistivity is unable to invert Brie exponent. Moreover, there is also a test where porosity is inverted together with CO_2 saturation. In the later case, the inversion system become under-determined.

The 1D profile of resistivity (Rt) as input and porosity as a priori in point A is shown in Figure 5.12. Reservoir parameters for the inversion are given in table 3.4. It is important to remind that the porosity used as a apriori to estimates CO_2 saturation is inverted from Vp in baseline model. This porosity is smoothed for the inversion (red curve, Figure 5.12). The CO_2 saturation inverted from resistivity is shown in Figure 5.12. As expected, high resistivity coincides to high CO_2 saturation. The CO_2 saturation reach $\pm 70\%$ at depth 820 m and decreases gradually to 30% at depth 975 m. At depth 980 m, the CO_2 saturation drops to around 10% and below depth 1025 m, no CO_2 is accumulated.
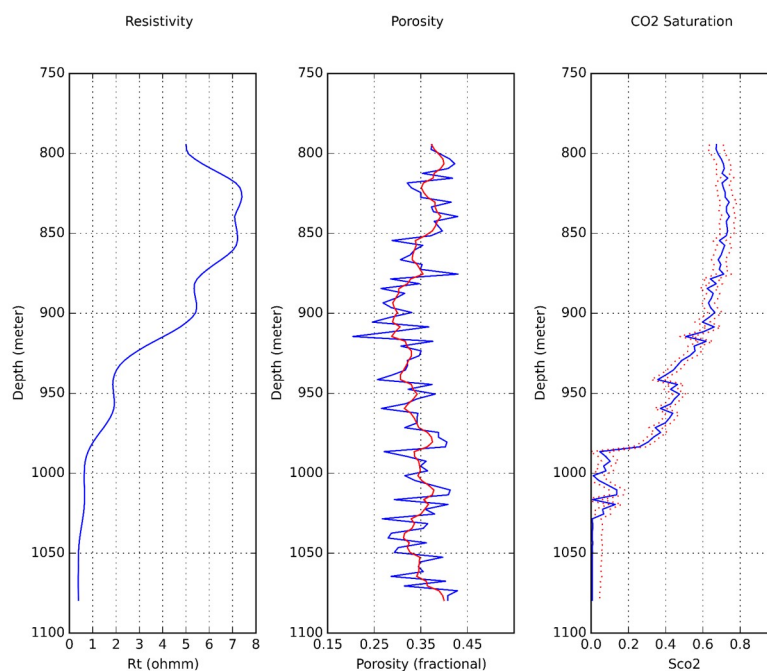
Figure 5.12: 1D profiles of resistivity (Rt) as input, porosity (ϕ) as a priori, and inverted CO_2 saturation at point A. The dotted red line is the mean value plus minus uncertainty.

Inversion system becomes under-determined when Rt is used to invert CO_2 saturation and porosity (Figure 5.13a). It shows that when CO_2 saturation is low ($< 10\%$), the trend is quite similar to that when inverted alone. The CO_2 saturation is down to around 20% at depth 800, 850, 900, 925, and 930 m. Another test is conducted by taken the porosity as equal to 0.37 (Furre et al., 2015). Figure 5.13b shows the comparison of fluid saturation inverted from this case. It shows that if porosity is constant, the CO_2 saturation is not showing small oscillations and the frequency of CO_2 saturation log is quite similar to the input. The tests show that the trend of CO_2 saturation is heavily influenced by the input. Small oscillations are observed in CO_2 saturation trend as a result of using porosity inverted from Vp in baseline model
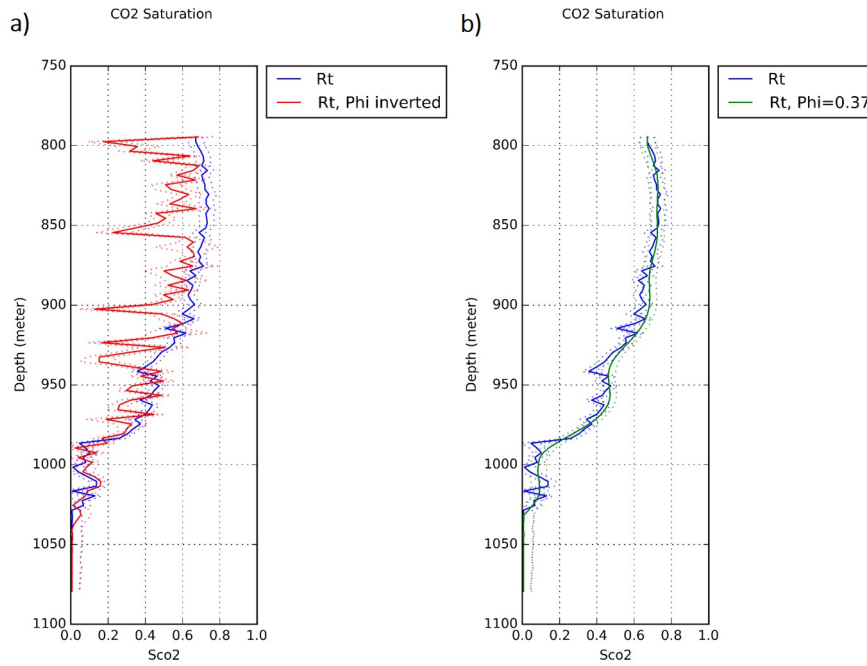
Figure 5.13: Comparison of inverted CO_2 saturation from resistivity as input. (a) CO_2 saturation inverted together with porosity (red curve) compare to CO_2 saturation when porosity is used as a priori (blue curve). (b) CO_2 saturation inverted with porosity is assume constant (0.37) as in (Furre et al., 2017) (green curve). The dotted line is the mean value plus minus uncertainty.

In point B, 1D profiles of Rt, porosity, and CO_2 saturation are shown in Figure 5.14. Similar to point A, the trend of CO_2 saturation in point B is influenced by input (Rt) with small oscillations as a result of using porosity inverted from Vp in baseline model. The saturation reach 65% at the top formation and decreases gradually to around 30% at the formation base.
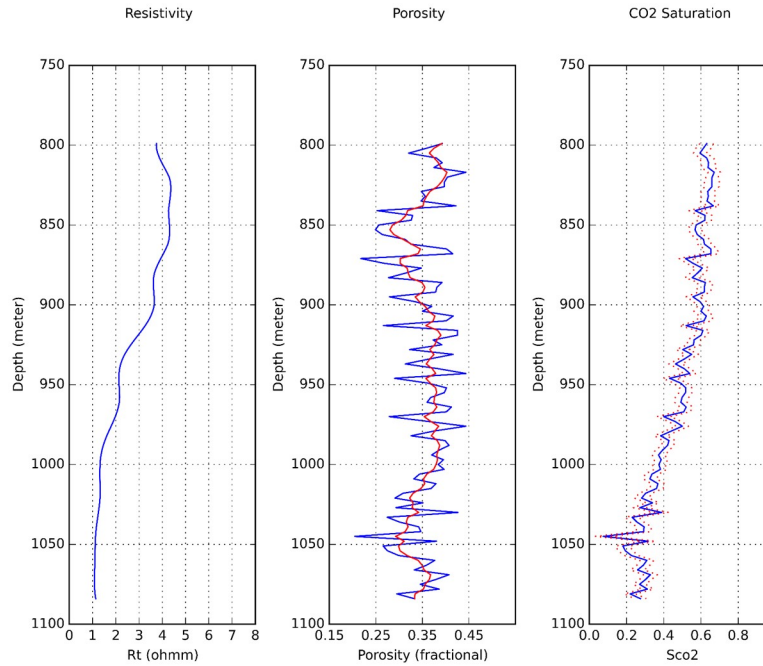
Figure 5.14: 1D profile of resistivity (Rt) as input, porosity (ϕ) as a priori, and inverted CO_2 saturation at point B. The dotted red line is the mean value plus minus uncertainty.

Case 2 : Estimation of CO_2 saturation and Brie exponent (e) using 2 inputs

1D profiles of P-wave velocity (Vp) and resistivity (Rt) in point A are given in Figure 5.8. The CO_2 saturation inverted from Vp and Rt is given in Figure 5.15a. It shows that the trend of 1D profile of CO_2 saturation is driven more by resistivity than P-wave velocity. The trend of CO_2 saturation inverted from Vp and Rt is close to CO_2 saturation inverted from only Rt (Fig.5.15b) when saturation is more than 20% (Depth 800 m - 975 m). When CO_2 saturation is small, the trend is closer to the result inverted from Vp. It shows that below depth 975 m, CO_2 saturation inverted from Vp and Vp + Rt are around 12% while CO_2 saturation inverted from Rt is close to 0%.

Figure 5.15c shows the CO_2 saturation if Brie exponent is known. The inversion system become over-determined where two constrained (Vp and Rt) are used to invert one parameter (CO_2 saturation). It shows a difference at low CO_2 saturation at depth 980 m - 1025 m.
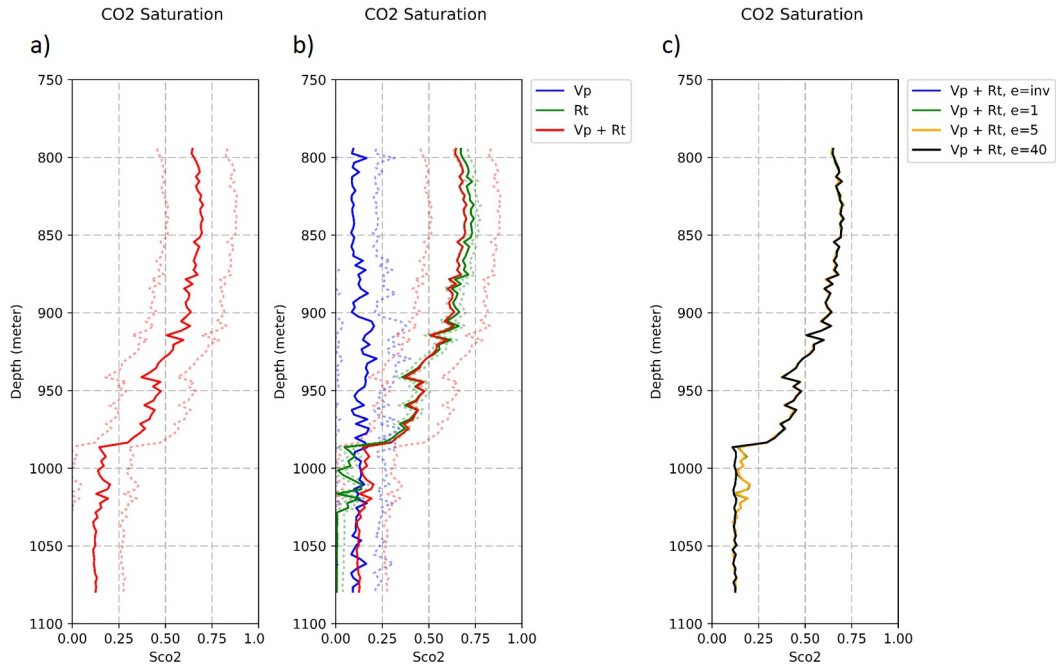
Figure 5.15: (a) CO_2 saturation inverted from Vp and Rt at point A. (b) saturation inverted from Vp, Rt, and Vp + Rt. The dotted line is the mean value plus minus uncertainty. (c) CO_2 saturation inverted from Vp + Rt if e is known. The CO_2 saturation in (a) is also shown here for comparison.

When porosity is inverted together with CO_2 saturation and Brie exponent, the saturation drops. CO_2 saturation from this scenario ranges from 20% to 57% at the top and middle of formation (Figure 5.16, red curve). When saturation is low ($< 20\%$) at depth below 975 m, the CO_2 saturation trend is close to CO_2 saturation if inverted from Vp + Rt when porosity is known (Figure 5.16, blue curve). The test shows that low CO2 saturation ($< 15\%$) is well estimated even when the inversion system is under-determined.
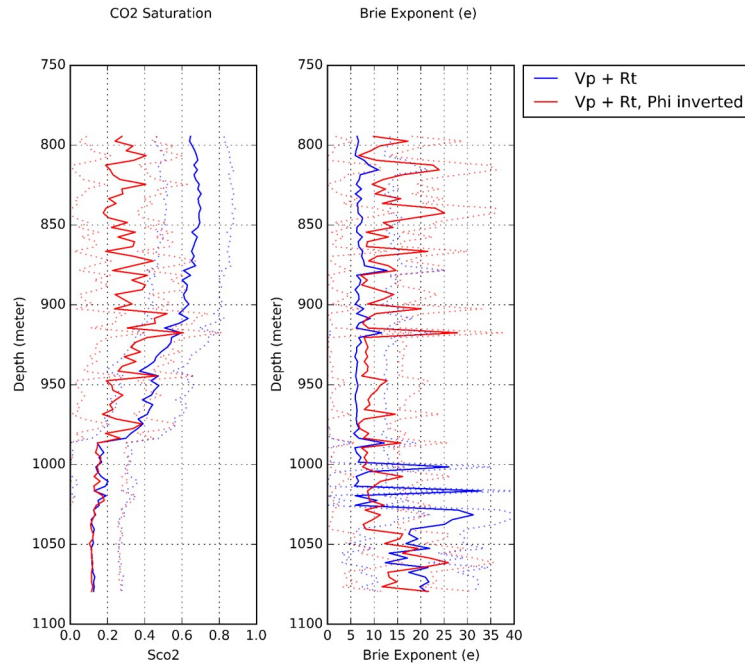
Figure 5.16: Comparison of inverted CO_2 saturation and Brie Exponent from Vp and Rt as input at point A. (a) CO_2 saturation inverted together with porosity (red curve) compared with CO_2 saturation when porosity is used as a priori (blue curve). (b) Brie Exponent inverted from Vp and Rt when porosity is inverted together (red curve). The dotted line is the mean value plus minus uncertainty.

The objective of this thesis is to estimate fluid saturation and its mixing type inside the reservoir. In the sensitivity test, the combination of P-wave velocity and resistivity can estimate both parameters better than using P-wave velocity alone. Therefore, Brie exponent is inverted simultaneously with CO_2 saturation and the result at point A is shown in Figure 5.17. Brie exponent is around 7 from depth 800 m to 975 m. Below this depth, Brie exponent increases between 15 and 25. The uncertainty of inverted Brie exponent is ranging from 5 to 10.
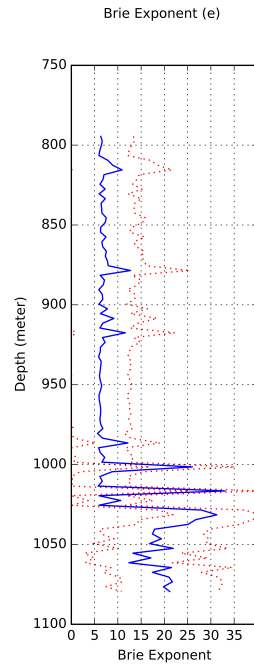
Figure 5.17: Brie exponent inverted from Vp+Rt at point A. Brie exponent is inverted simultaneously with CO_2 saturation. The dotted red line is the mean value plus minus uncertainty.

Figure 5.18 shows 1D profiles of Vp, Rt, inverted CO_2 saturation and Brie exponent (e) at point B. It shows $\pm 60\%$ CO_2 saturation from depth 800 m to depth 900 m before it downs gradually to $\pm 30\%$ at the formation base. Brie exponent is ranging from 6 to 10 with the average value of around 7.
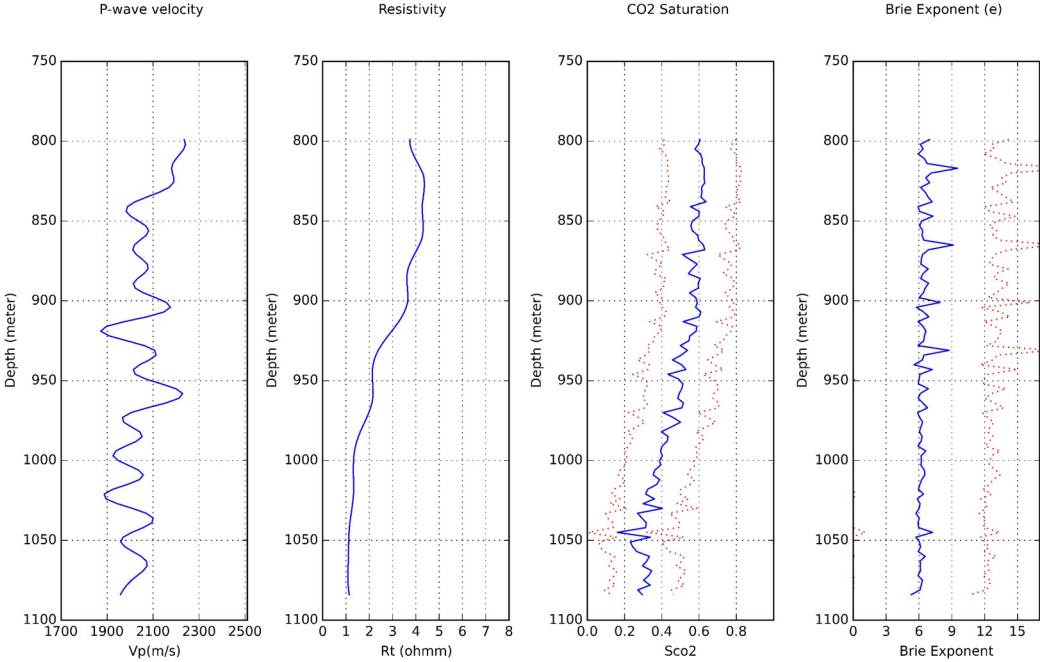
Figure 5.18: 1D profile of Vp and Rt as input, and inverted CO_2 saturation and Brie exponent at point B. The dotted red line is the mean value plus minus standard deviation

The difference of CO_2 saturation from inversion involving resistivity as input in points A and B is that in point B, the predicted CO_2 saturation is always above 20% from top to the base of formation, while in point A CO_2 saturation can reach 0% at the formation base.

5.2 2D Inversion

For 2D inversion, the same procedures as in 1D inversion are applied to the target region along inline 1838 and 1874. Here, 700 offsets from depth 745 m to 1195 m were stacked. The uncertainty of inversion result also shown in 2D section. For baseline model, Vp as input for inversion is shown in Figure 4.7 for inline 1838 and Figure 4.8 for inline 1874. For brevity, some figures are given in Appendix. The area of study is limited to Utsira formation (From Top Sand Wedge to Base Utsira). In this study, the five meter shale layer and the sand wedge are considered to be one single body.

5.2.1 Estimation of frame moduli at Inline 1838

Inline 1838 of K_S, $k0$, and ρ_S are shown in Figure D.1 (Appendix D). Inverted K_D, G_D, and porosity (ϕ) for inline 1838 are shown in Figure 5.19. Figure 5.19a shows two region with low K_D value at depth 800 m to 870 m and around depth 950 m to 1050 m. The K_D in these areas are approximately below 2.5 GPa and correlate to high porosity value ($> 34\%$, Figure 5.19e). This is the signature of unconsolidated sands in Utsira formation. While high K_D, G_D and low ϕ are showing the shale layers. High G_D is observed at depth 850 m to 950 ($\pm$ 2 GPa, Figure 5.19c). The uncertainty is between 1 and 2 GPa for K_D (Figure 5.19b) and between 1 and 1.3 GPa for G_D (Figure 5.19d), while for porosity the uncertainty is ranging from 7.5% to 10% (Figure 5.19f).
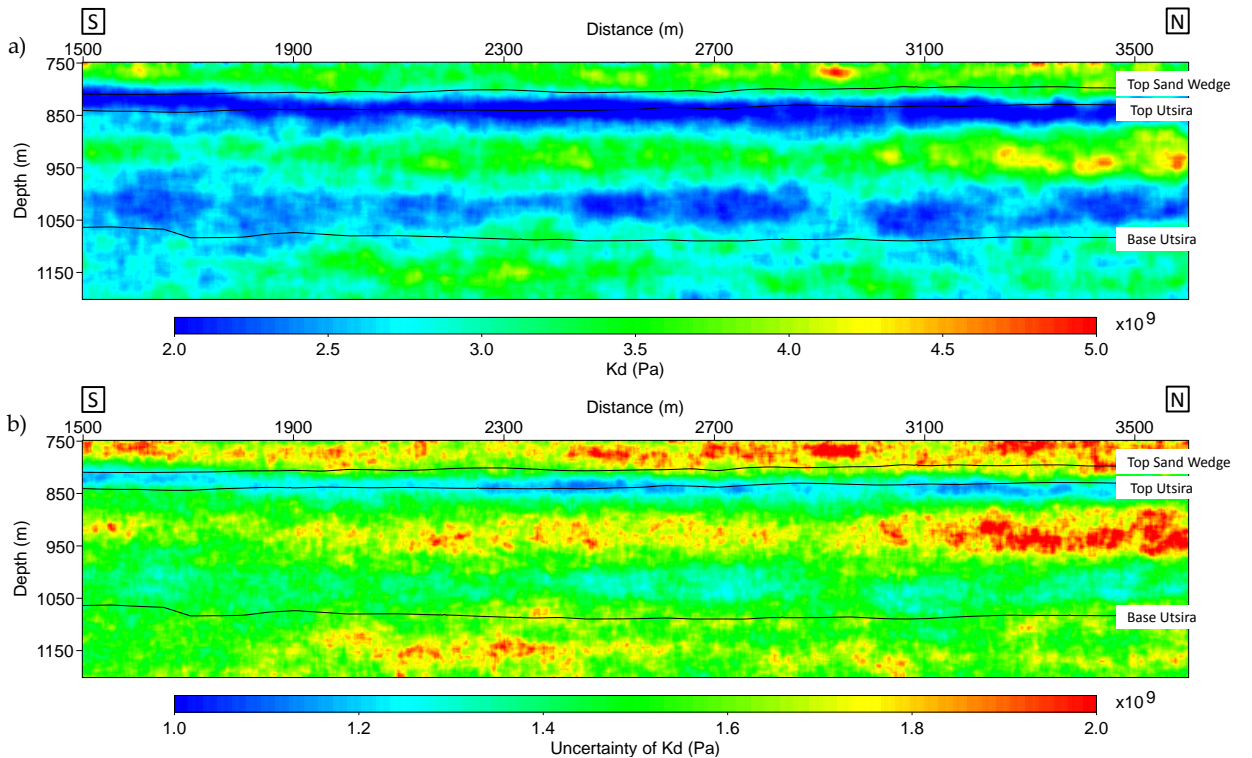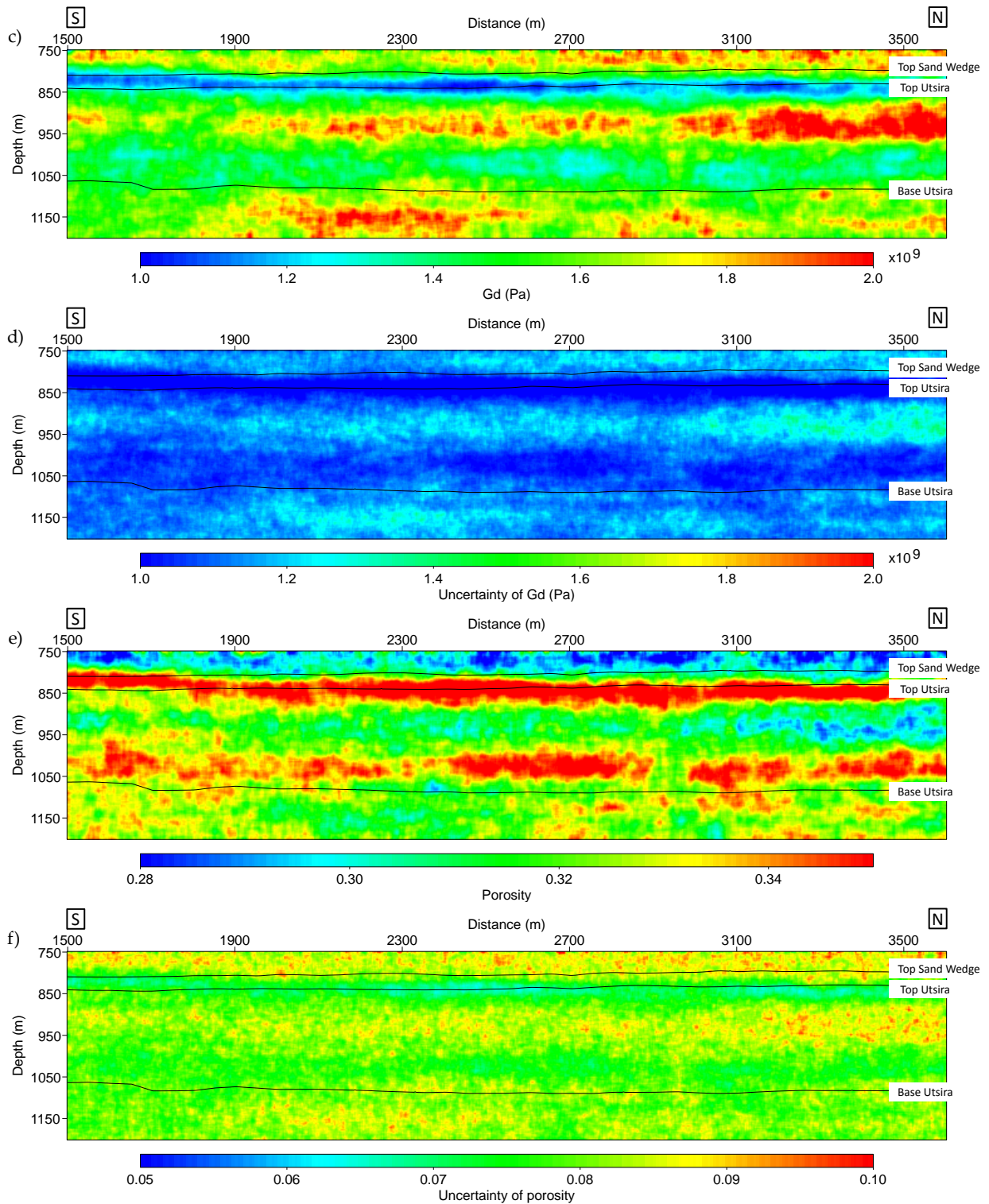
Figure 5.19: 2D profile of (a) Frame bulk modulus (K_D) and (b) uncertainty of K_D, (c) frame shear modulus (G_D) and (d) uncertainty of G_D, (e) porosity (ϕ) and (f) uncertainty of ϕ at inline 1838.

5.2.2 Estimation of frame moduli at Inline 1874

Inline 1874 of K_S, $k0$, and ρ_S are shown in Figure D.2, Appendix D. Inverted K_D, G_D, and porosity (ϕ) for inline 1874 is shown in Figure 5.20. Figure 5.20a shows low K_D values at depth 950 m ($\pm$ 1.8 GPa). Similar to inline 1838, this region correlate to high porosity ($\pm$ 37%, Figure 5.20e) and low G_D ($\pm$ 1.1 GPa, Figure 5.20c). The uncertainty is between 1 and 1.8 GPa for K_D (Figure 5.20b) and between 0.9 and 1.2 GPa for G_D (Figure 5.20d), while for porosity the uncertainty is ranging from 6% to 9% (Figure 5.20f)
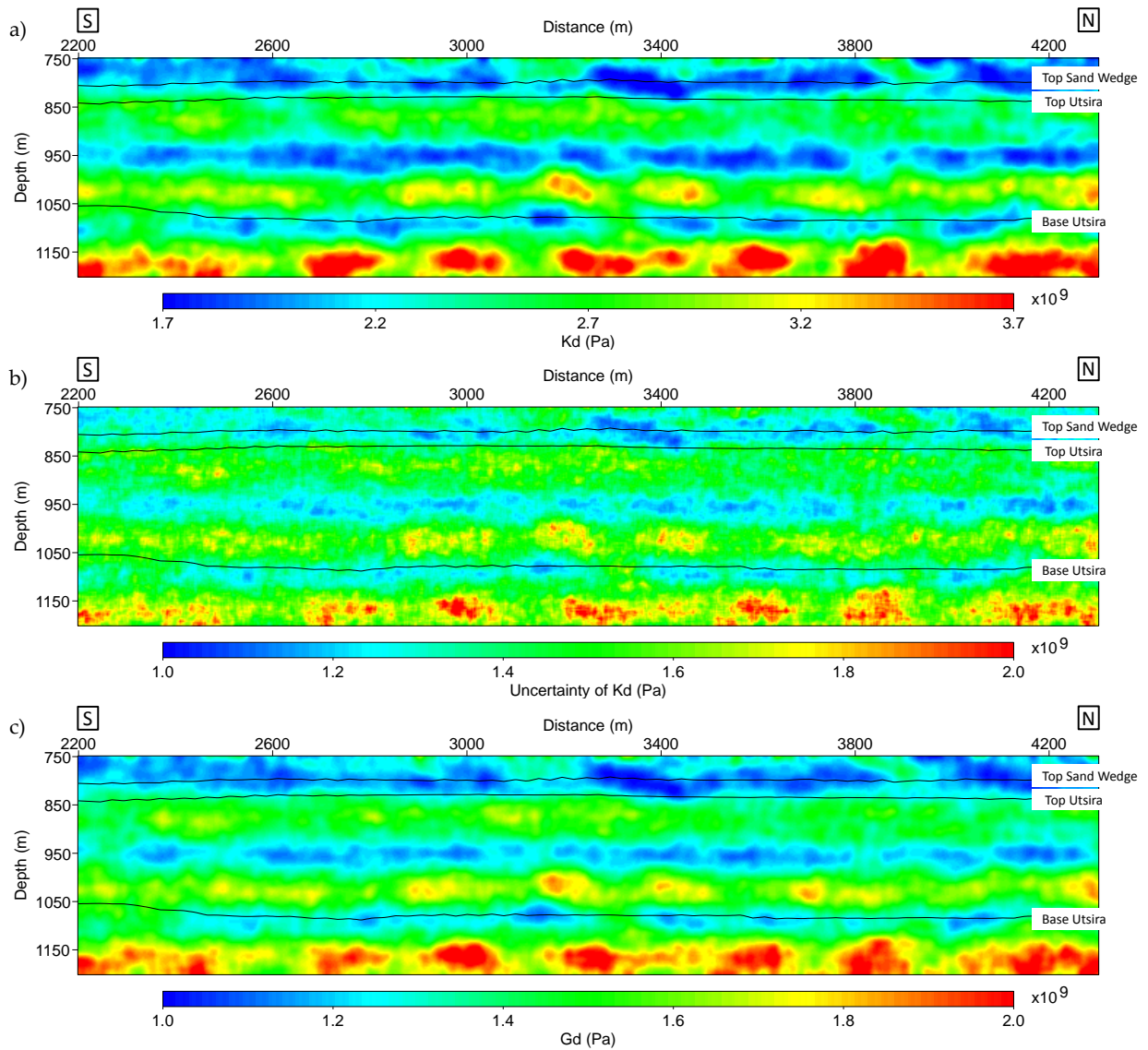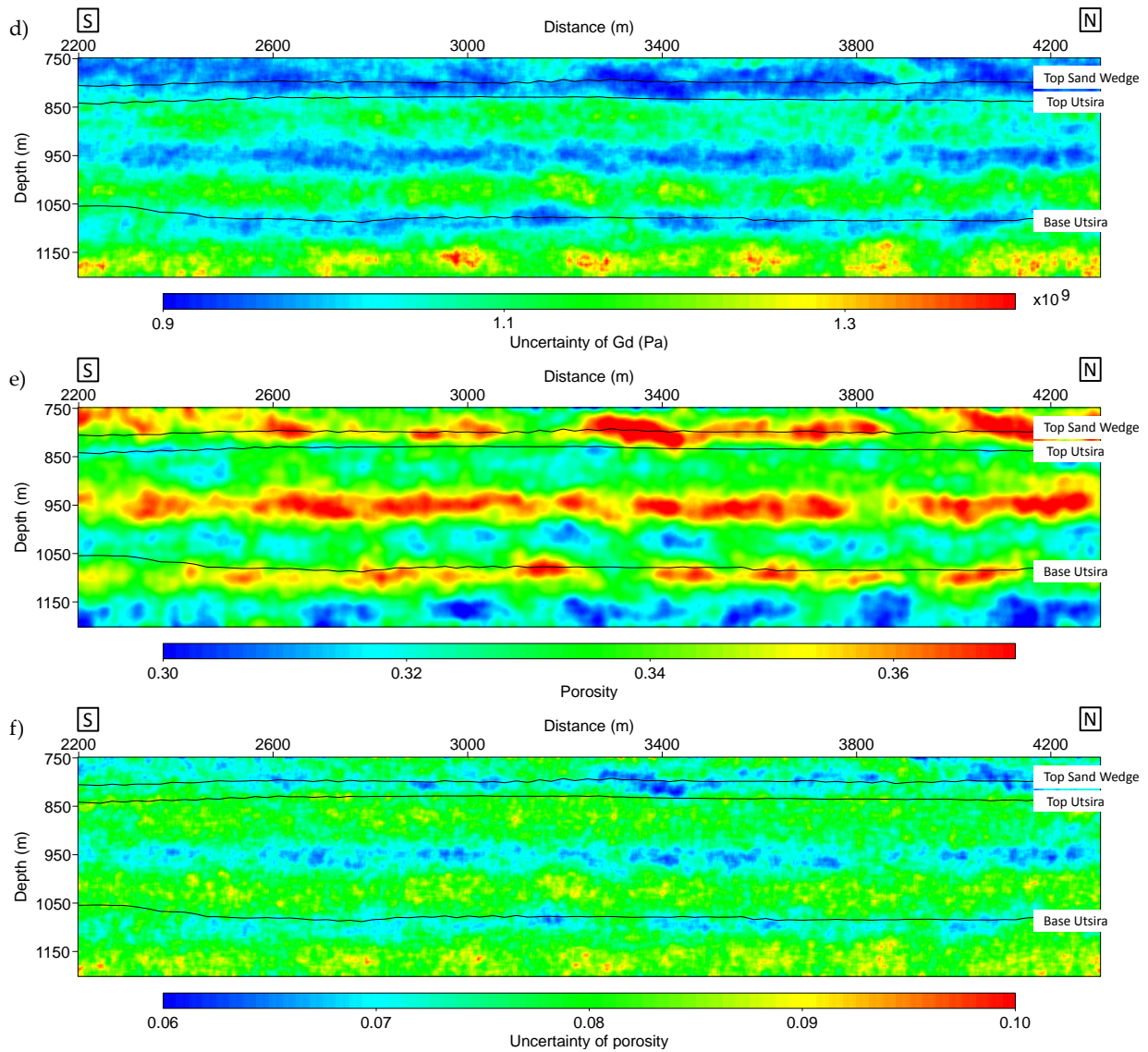
Figure 5.20: 2D profile of (a) Frame bulk modulus (K_D) and (b) uncertainty of K_D, (c) frame shear modulus (G_D) and (d) uncertainty of G_D, (e) porosity (ϕ) and (f) uncertainty of ϕ at inline 1874.

5.2.3 Estimation of CO_2 saturation and Brie exponent (e) at Inline 1838

2D sections of Vp and Rt as input for inversion to estimate CO_2 saturation and Brie exponent (e) at Inline 1838 is shown in Figure 4.9 and Figure 4.12, respectively. The 2D profiles of a priori for inversion are shown in Figure D.1 and Figure 5.19. Grain and fluid properties are shown in Tabel 3.3, Table 3.4, and Table 3.5. The 1D profile at x=2500 at this inline is selected to analyze the accumulation of CO_2 located in the middle of the plume.

Estimation of CO_2 saturation

2D profiles of inverted CO_2 saturation are shown in Figure 5.21. Figure 5.21a and 5.21b

show inverted CO_2 saturation and uncertainty using Vp as input, while Figure 5.21c and 5.21d are the CO_2 saturation inversion and uncertainty using Rt as input. CO_2 saturation from combination of Vp and Rt is shown in Figure 5.21e and the uncertainty is shown in Figure 5.21f.
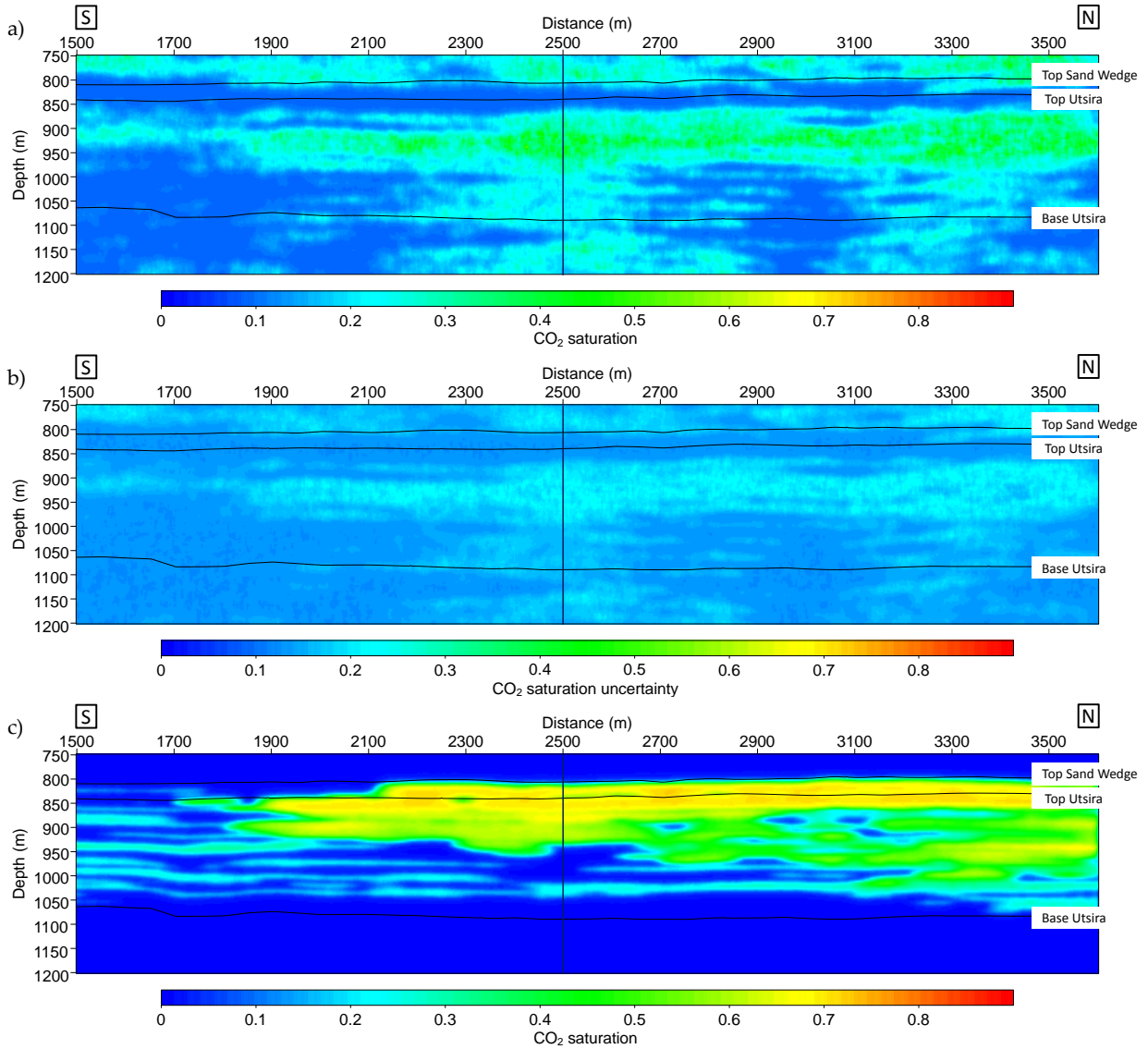
Figure 5.21: 2D profile of CO_2 saturation and uncertainty at inline 1838 using (a & b) Vp as input, (c & d) Rt as input, and (e & f) Vp + Rt as input.

The inversion result from Vp, Rt, and Vp + Rt show that CO_2 was accumulated from around x = 1800 to the North part of the line. Below Top Utsira, The CO_2 saturation inverted from Vp was around 15% and increases with depth to approximately 35%. After depth 1000 m, CO_2 saturation starts to decrease. At the sand wedge (below Top Sand Wedge and above Top Utsira), the CO_2 saturation inverted from Vp is small ($\pm$ 5-10%, Fig. 5.21a). However, this pattern is not seen from CO_2 saturation inverted from Rt (Fig. 5.21c) and Vp + Rt (Fig. 5.21e). Here, CO_2 saturation accumulated at sand wedge is around 60%. Similar to 1D profile, the spread of CO_2 saturation is highly affected by resistivity as input. It shows that high resistivity correlates to high CO_2 saturation.

Estimation of Brie exponent (e)

Brie exponent is inverted together with CO_2 saturation and the 2D results of Brie exponent at inline 1838 are shown in Figure 5.22. Figure 5.22a and Figure 5.22c shows the Brie exponent inverted from Vp and Vp+Rt, respectively. The uncertainty is shown in Figure 5.22b and Figure 5.22d.

Figure 5.22: 2D profiles of Brie exponent and uncertainty at inline 1838 using (a & b) Vp as input, (c & d) Vp + Rt as input.

The 1D profiles of CO_2 saturation and Brie exponent are shown in Figure 5.23. The Utsira formation is from depth 800 m to depth 1050 m. This is taken at x = 2500, inline 1838 (Black vertical line, Fig. 5.21 and Fig. 5.22).

Figure 5.23: 1D profiles of CO_2 saturation and Brie exponent at x=2500, inline 1838. The result inverted from Vp is shown in blue curve. The result inverted from Rt is shown in green curve. The result inverted from Vp + Rt is shown in red curve. The Utsira formation is from depth 800 m to depth 1050 m. The dotted line are the mean value plus minus uncertainty

CO_2 saturation inverted using Vp as input is ranging from 10% to 40%, while using Rt as input the range becomes bigger, from 0% to around 65%. At high CO_2 saturation (> 60%), the difference of result inverted from Rt and Vp+Rt is small. Below depth 925 m, the difference is bigger. Moreover, the uncertainty inverted from Rt (Fig. 5.21d) is much smaller than the uncertainty of CO_2 saturation inverted from Vp + Rt. Figure 5.23 also shows that high CO_2 saturation (> 60%) correlates to low Brie exponent ±7.

### 5.2.4 Estimation of CO_2 saturation and Brie exponent (e) at Inline 1874

Vp and Rt as input for inversion to estimate CO_2 saturation and Brie exponent (e) at Inline 1874 are shown in Figure 4.10 and Figure 4.13, respectively. The 2D profile of a priori for inversion are shown in Figure D.2 and Figure 5.20. Grain and fluid properties are shown in Tabel 3.3, Table 3.4, and Table 3.5. The 1D profile at x=3200 at this inline was selected to analyze the accumulation of CO_2 located in the middle of the plume.

Estimation of CO_2 saturation

2D profiles of inverted CO_2 saturation are shown in Figure 5.24. Figure 5.24a and 5.24b show inverted CO_2 saturation and uncertainty using Vp as input, while Figure 5.24c and 5.24d are the inversion result and uncertainty using Rt as input. Inversion result from combination of Vp+Rt are shown in Figure 5.24e and the uncertainty is shown in Figure 5.24f.
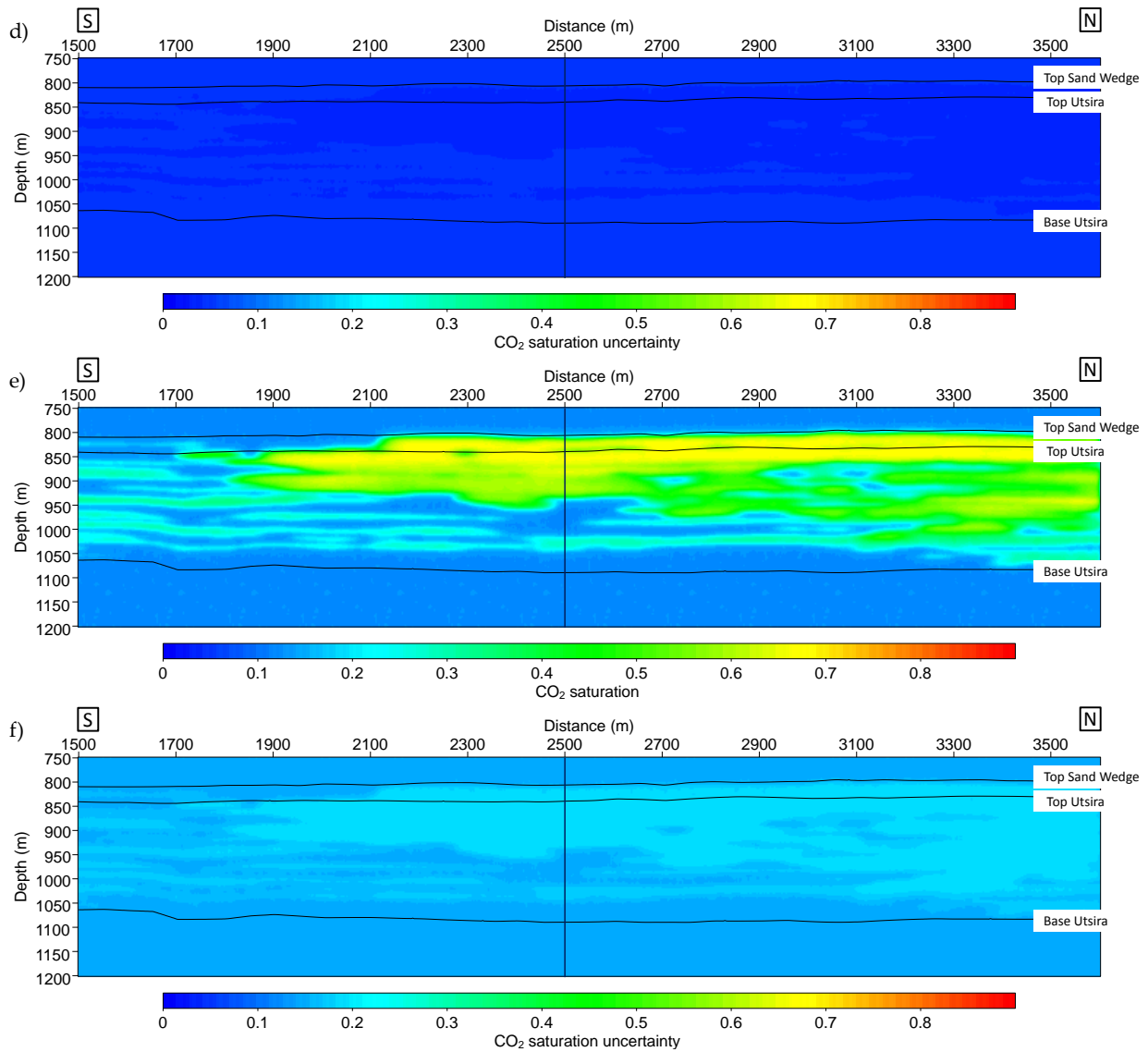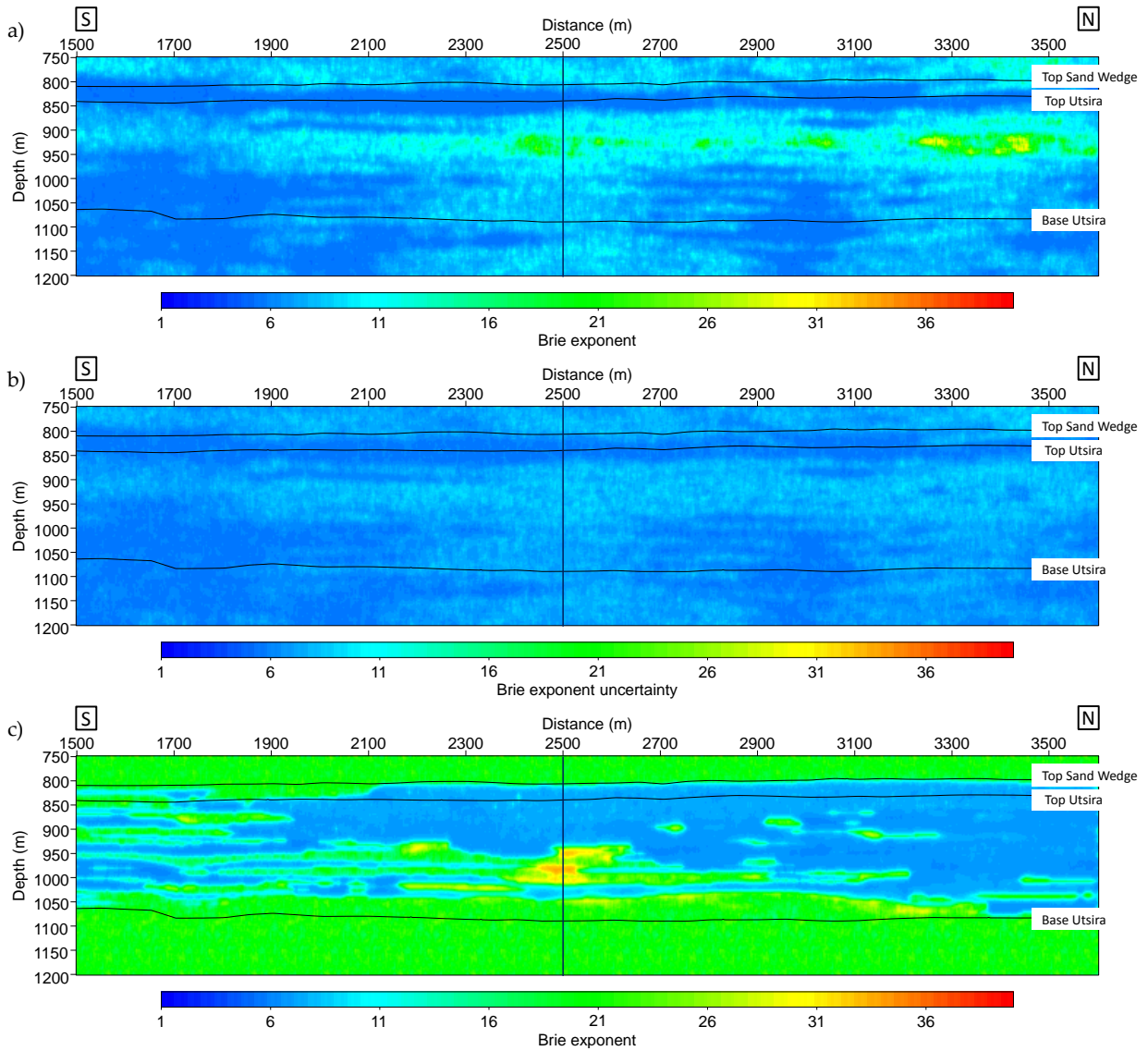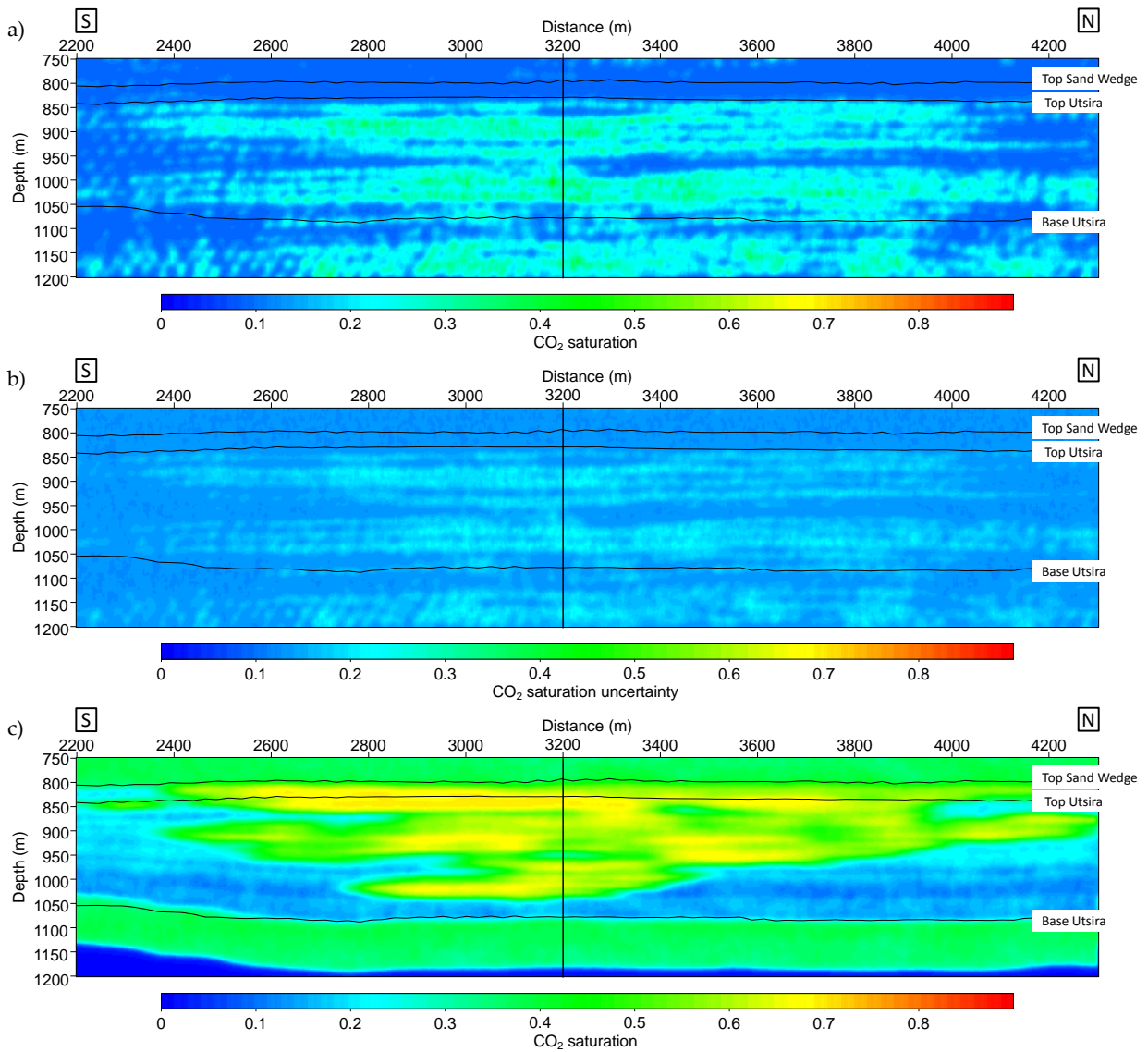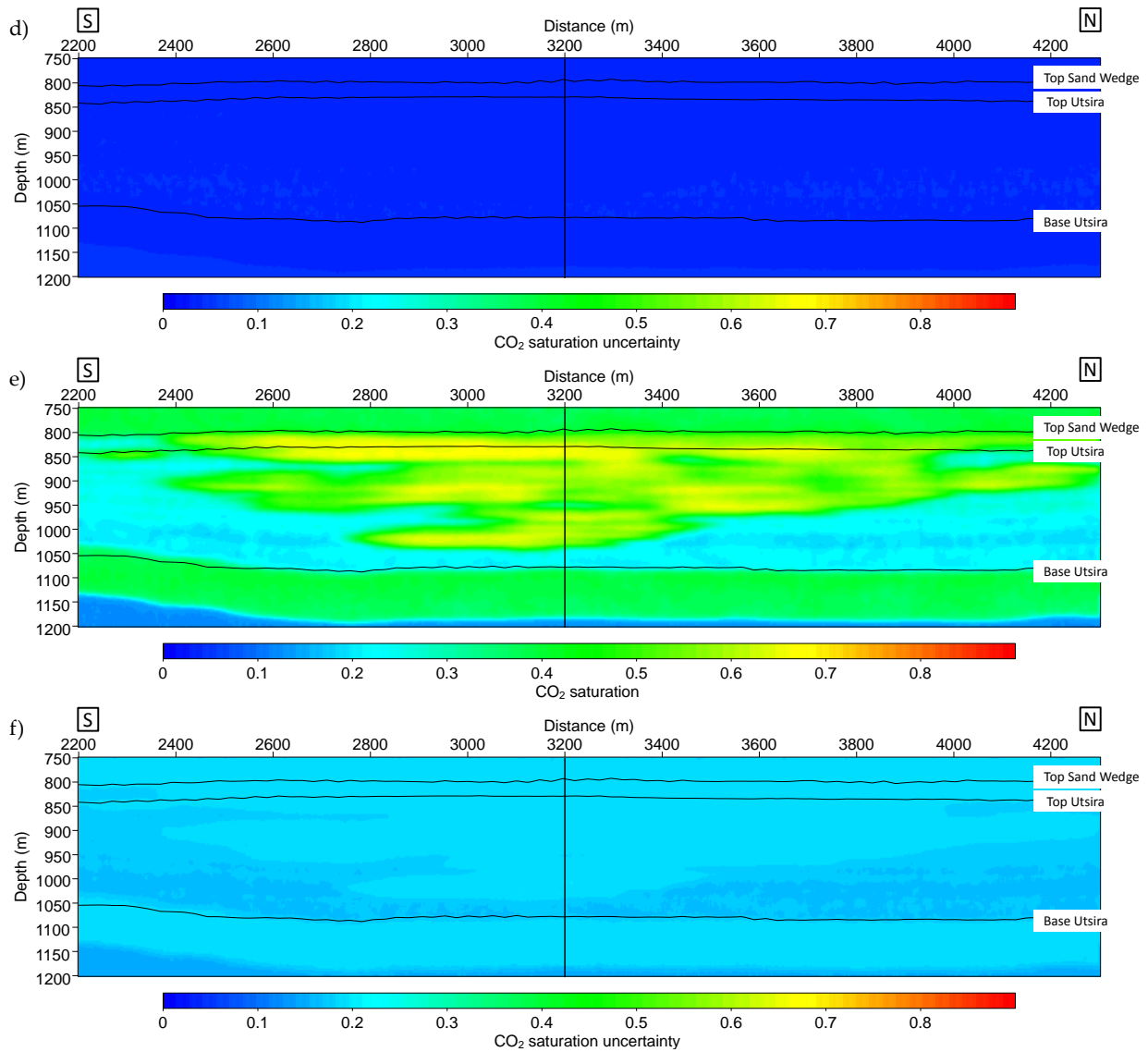
Figure 5.24: 2D profiles of CO_2 saturation and uncertainty at inline 1874 using (a & b) Vp as input, (c & d) Rt as input, and (e & f) Vp + Rt as input.

The inversion result from Vp as input (Figure 5.24a) shows small accumulation of CO_2 at the sand wedge. However, inversion results from Rt (Figure 5.24c) and Vp + Rt (Figure 5.24e) show the opposite. This is similar to that for inline 1838. The saturation trends and values are highly driven by resistivity as input. The uncertainty of CO_2 inverted from Rt (Fig. 5.24d) is very small compare to the uncertainty of CO_2 inverted from Vp (Fig. 5.24b) and Vp + Rt (Fig. 5.24f). It shows that the uncertainty of CO_2 is less than 10% if inverted using only Rt. However, Rt alone is unable to invert Brie exponent.

Estimation of Brie exponent (e)

Brie exponent is inverted together with CO_2 saturation and are shown in Figure 5.25. Figure 5.25a and Figure 5.25c show the Brie exponent inverted from Vp and Vp+Rt, respectively. The uncertainty is shown in Figure 5.25b for inversion using Vp and Figure 5.25d for inversion using Vp+Rt.

5. Results
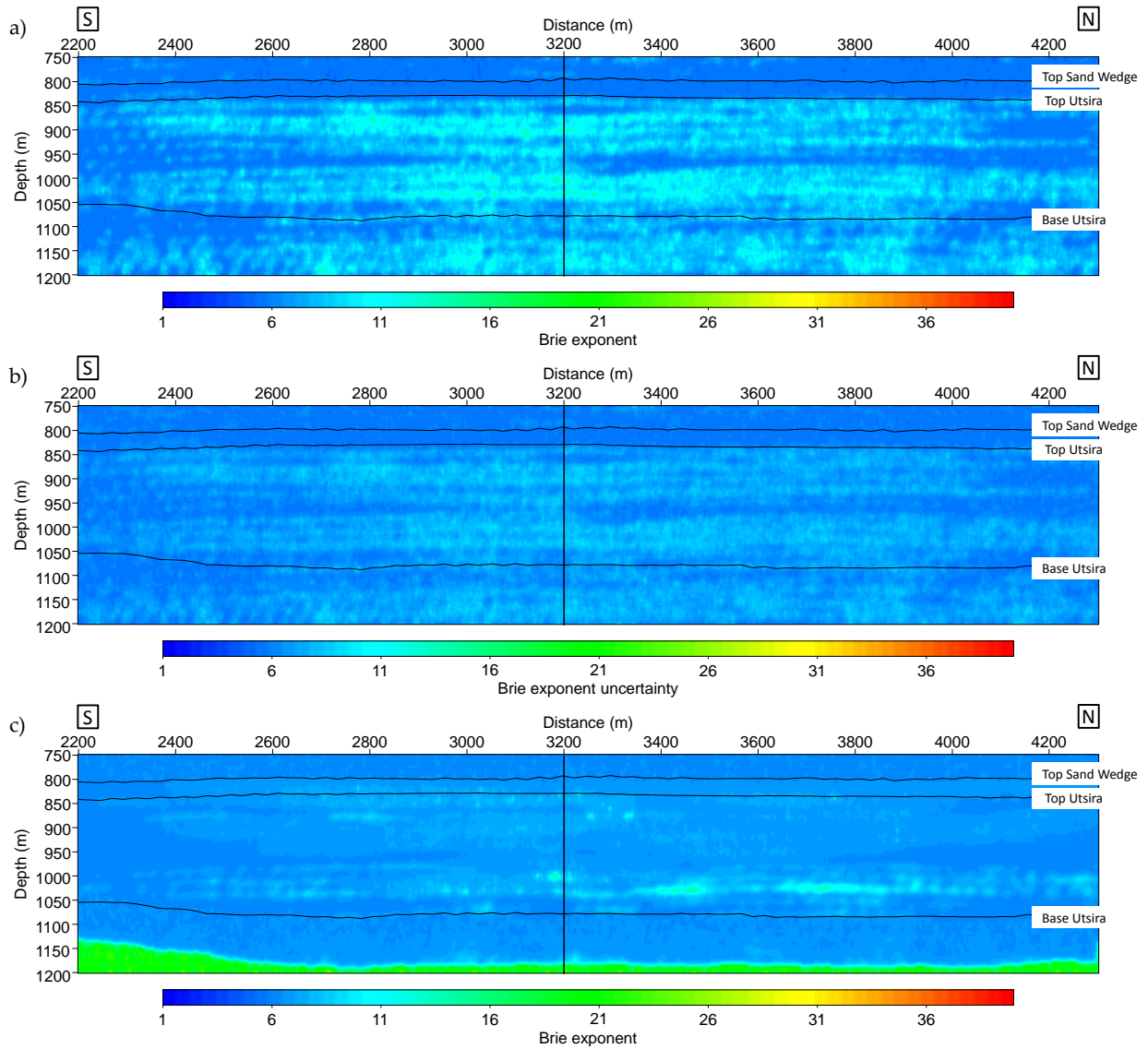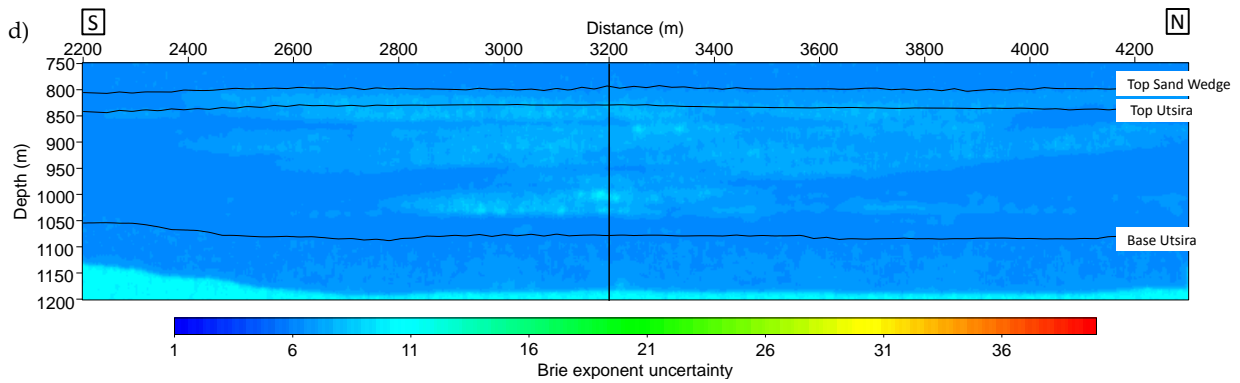
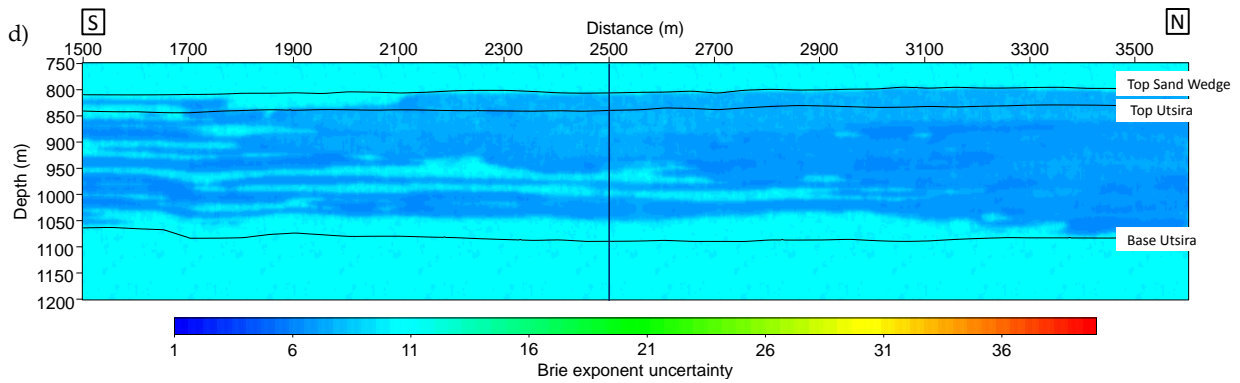**Figure 5.25:** 2D profiles of Brie exponent and uncertainty at inline 1874 using (a & b) Vp as input, (c & d) Vp + Rt as input.

The 1D profiles of CO_2 saturation and Brie exponent taken at x = 3200, inline 1874 (Black vertical line, Fig. 5.24 and Fig. 5.25) are shown in Figure 5.26. The Utsira formation is from depth 800 m to depth 1050 m. Similar to point B, the saturation always above 10% from Top Sand Wedge to Base Utsira. At this point, the CO_2 saturation inverted from Vp is ranging from 10% to 30%, while CO_2 saturation inverted from Rt and Vp+Rt are ranging from 10% to 60%. Moreover, Brie exponent inverted from Vp is ranging from 5 to 12, while Brie exponent inverted from Vp+Rt is ranging from 6 to 10 with the average value of around 7.
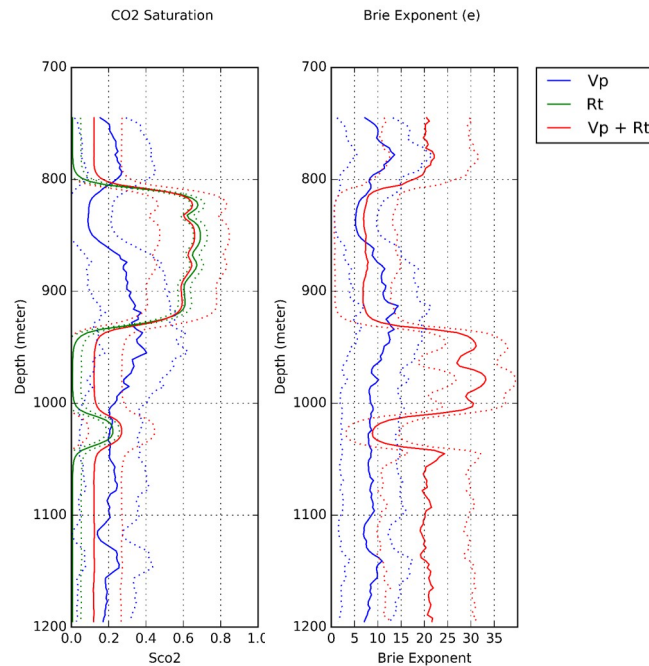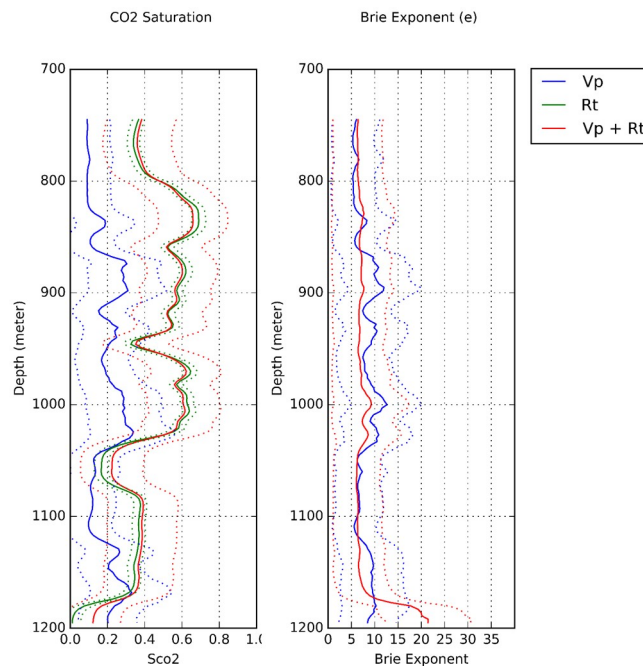

Figure 5.26: 1D profile of CO_2 saturation and Brie exponent at x=3200, inline 1874. The result inverted from Vp is shown in blue curve. The result inverted from Rt is shown in green curve. The result inverted from Vp + Rt is shown in red curve. The Utsira formation is from depth 800 m to depth 1050 m. The dotted line are the mean value plus minus uncertainty.

5.2.5 Estimation of CO_2 saturation using Vp if Brie exponent (e) is constant (Inline 1838)

This sub-chapter presents the 2D profiles of CO_2 saturation if Brie exponent is set as constant. Here, three values of e (1, 5, 40) are used and the inversion system become well-determined. The CO_2 saturation from this scenario are given in Fig. 5.27a, Fig. 5.27c, Fig. 5.27e for inversion using e equal to 1,5,40 respectively
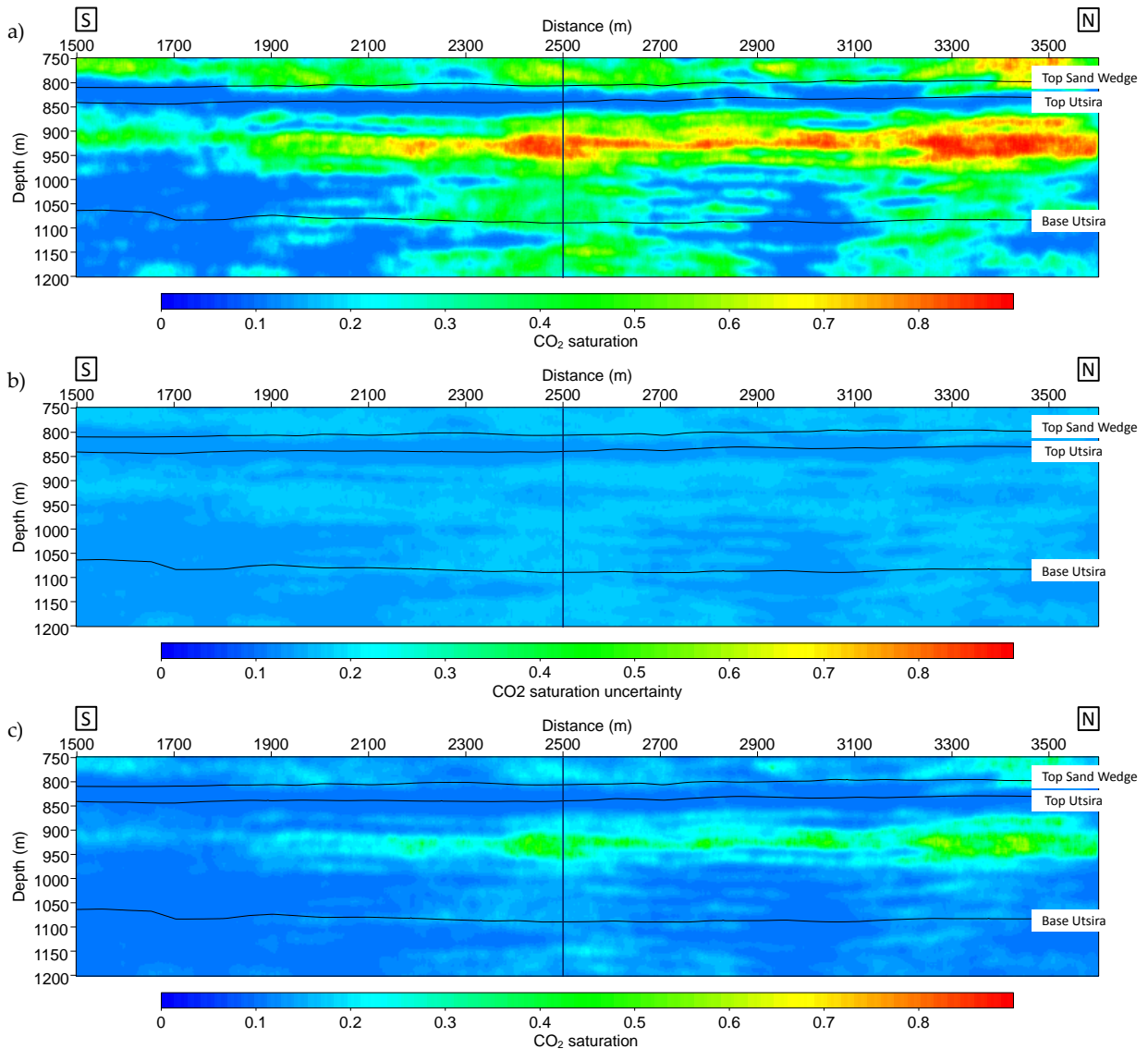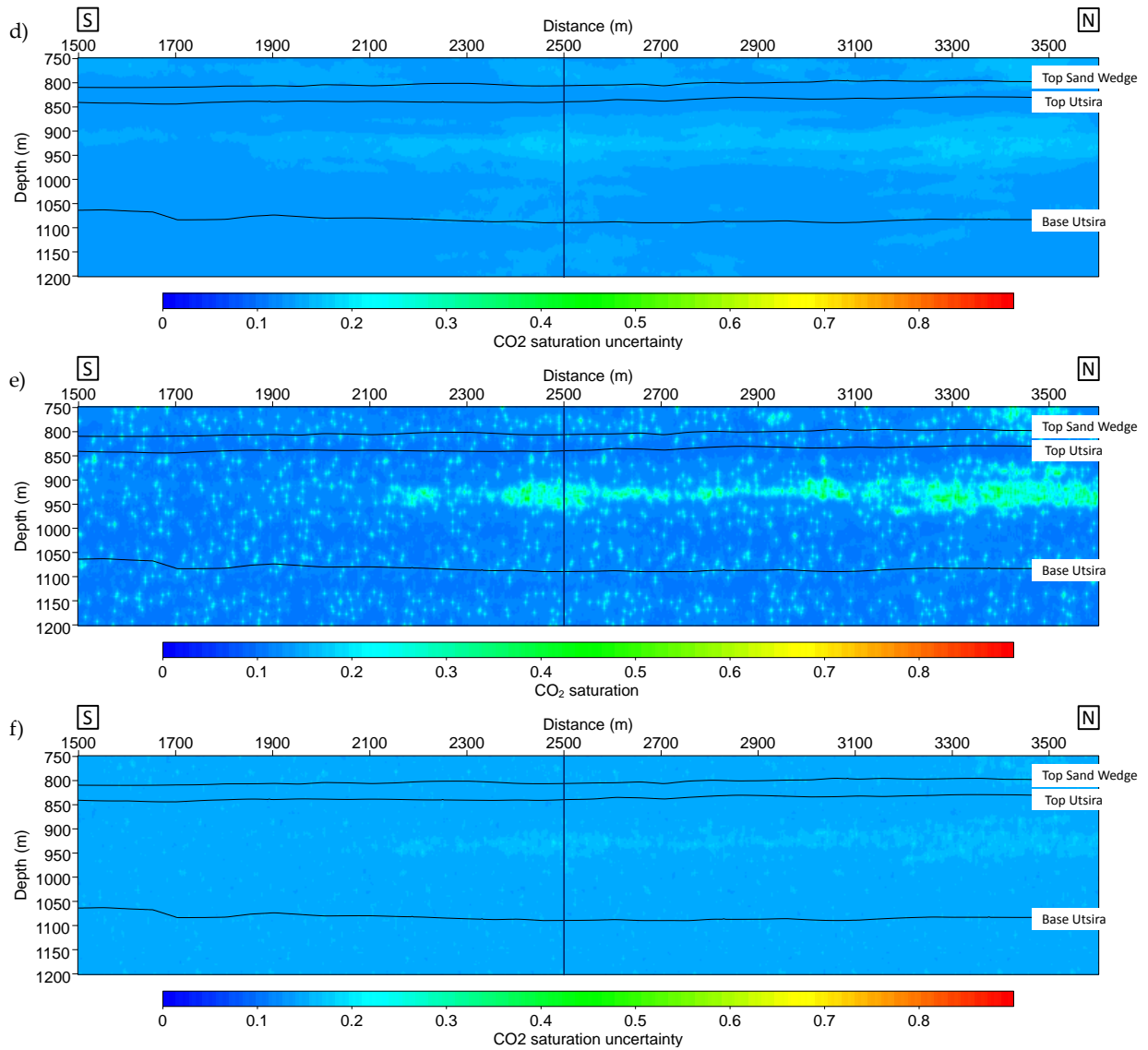
Figure 5.27: 2D profiles of CO_2 saturation and uncertainty inverted using Vp at inline 1838 with (a & b) Brie exponent = 1, (c & d) Brie exponent = 5, and (e & f) Brie exponent = 40.

It can be seen from all 2D sections that CO_2 is mostly accumulated at depth between 875 m and 975 m. 1D profile at x=2500 (black vertical line) is given in Figure 5.28. The Utsira formation is from depth 800 m to depth 1050 m.

Figure 5.28: 1D profiles of CO_2 saturation inverted using Vp at x=2500, inline 1838 with constant Brie exponent. The CO_2 saturation with inverted e is also shown here for comparison. The Utsira formation is from depth 800 m to depth 1050 m. The dotted line are the mean value plus minus uncertainty.

In this scenario, fully patchy mixing (e equal to 1) between CO_2 and brine gives CO_2 saturation ranging from 50% to 80% and at uniform mixing (e equal to 40) the saturation is ranging from 10% to 20%. The CO_2 saturation when e is inverted together is also shown here for comparison (blue curve, Fig. 5.28).

This scenario is also applied for Inline 1874. For brevity, the figures are given in Appendix E. Figure E.1 shows the 2D results of the inversion from this scenario at Inline 1874 and Figure E.2 shows the 1D profiles taken at x=3200 at Inline 1874.

5.2.6 Estimation of CO_2 saturation using Vp and Rt if Brie exponent (e) is constant (Inline 1838)

This sub-chapter presents the 2D profiles of CO_2 saturation if Brie exponent is set as constant. Here, three values of e (1, 5, 40) are used and the inversion system become over-determined. 2D profiles of CO_2 saturation and its uncertainty are shown in Figure 5.29. It shows that the CO_2 accumulation trend and uncertainty are driven by resistivity.
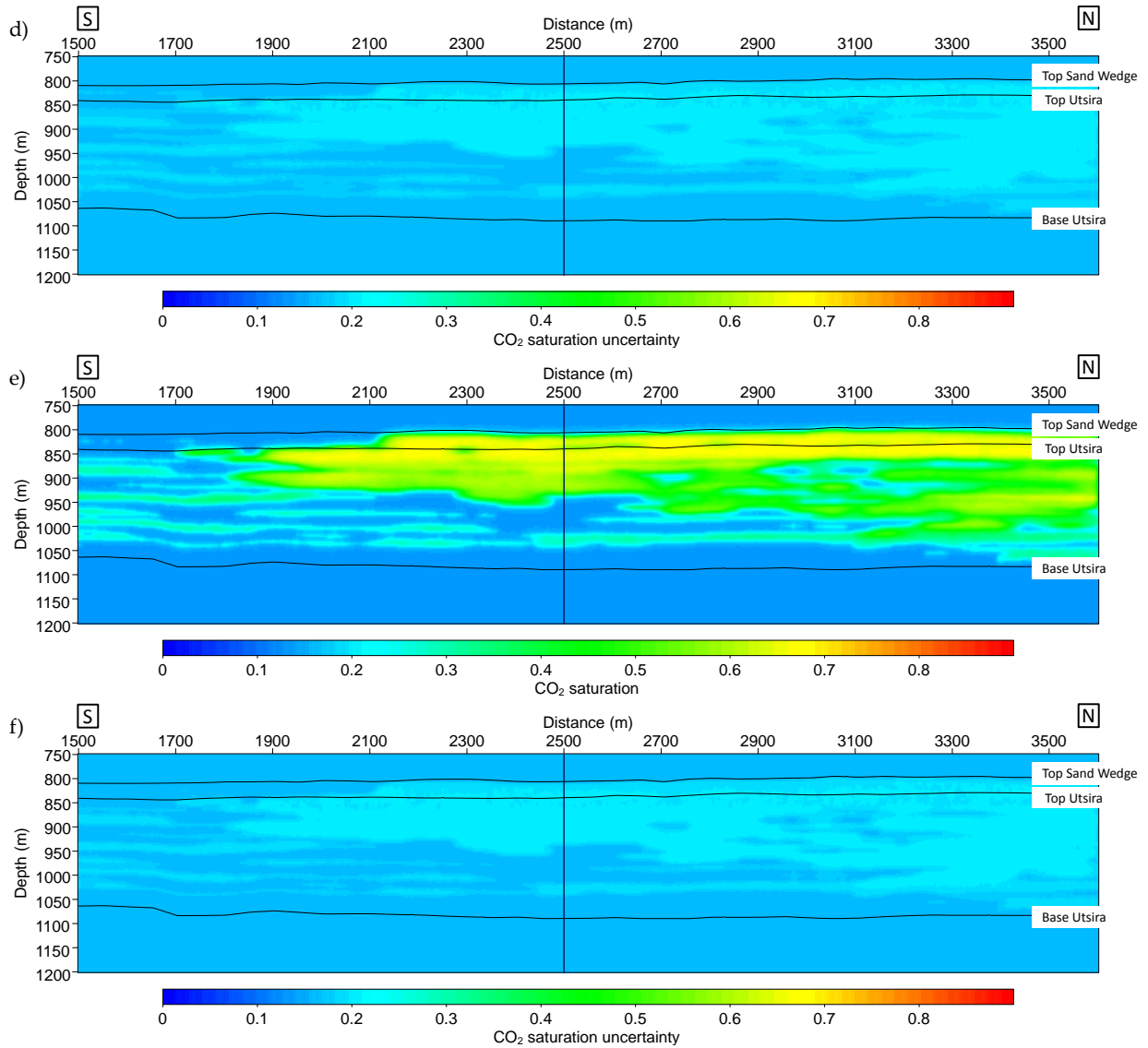
Figure 5.29: 2D profile of CO_2 saturation and uncertainty inverted using Vp + Rt at inline 1838 with (a & b) Brie exponent = 1, (c & d) Brie exponent = 5, and (e & f) Brie exponent = 40.

1D profile at x=2500 (black vertical line) is given in Figure 5.30. The CO_2 saturation when e is inverted together is also shown here for comparison (blue curve, Fig. 5.30). The Utsira formation is from depth 800 m to depth 1050 m. It shows little difference between CO_2 saturation inverted from this scenario. Different to CO_2 saturation inverted from Vp (with fixed e), this case shows that if Rt is involved as input, different Brie exponent does not give big impact to saturation trend.
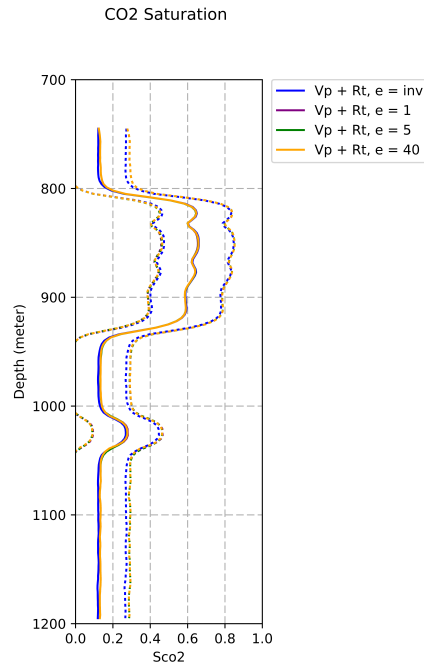
Figure 5.30: 1D profile of CO_2 saturation inverted using Vp + Rt at x=2500, inline 1838 with constant Brie exponent. The CO_2 saturation with inverted e is also shown here for comparison. The dotted line are the mean value plus minus uncertainty.

This scenario is also applied for Inline 1874. For brevity, the figures are given in Appendix F. Figure F.1 shows the 2D results of the inversion from this scenario at Inline 1874 and Figure F.2 shows the 1D profiles taken at x=3200 at Inline 1874.

5.2.7 Estimation of CO_2 saturation and Brie exponent (e) if porosity is inverted together (Inline 1838)

This sub-chapter presents the 2D profiles of CO_2 saturation, porosity, and Brie exponent if inverted together. Figure 5.31 shows 2D profiles of CO_2 saturation inverted from Vp, Rt, and Vp+Rt. Figure 5.34 shows 2D profiles of porosity inverted from Vp, Rt, and Vp+Rt. Figure 5.36 shows 2D profiles of Brie exponent inverted from Vp and Vp+Rt.

Estimation of CO_2 saturation
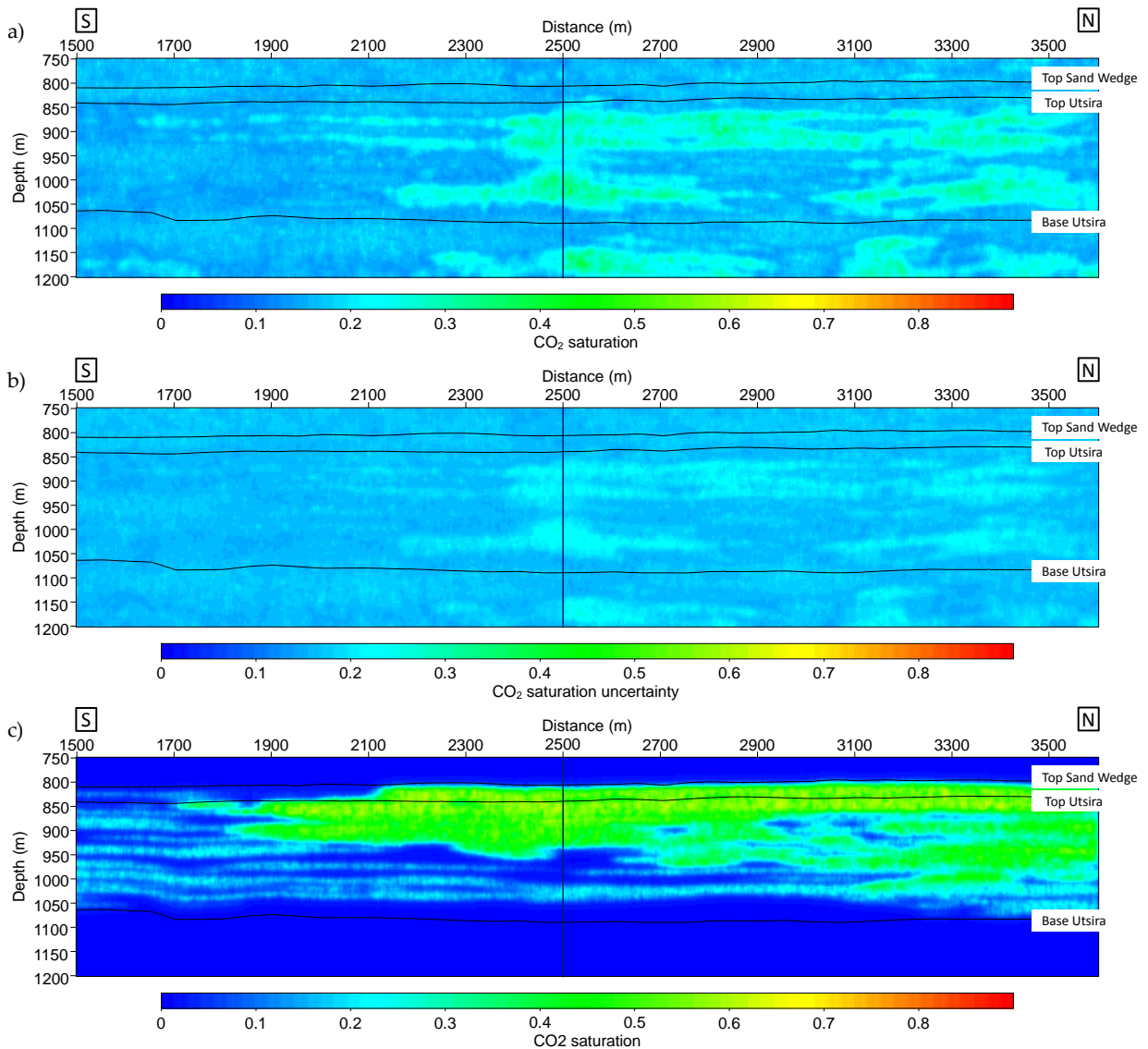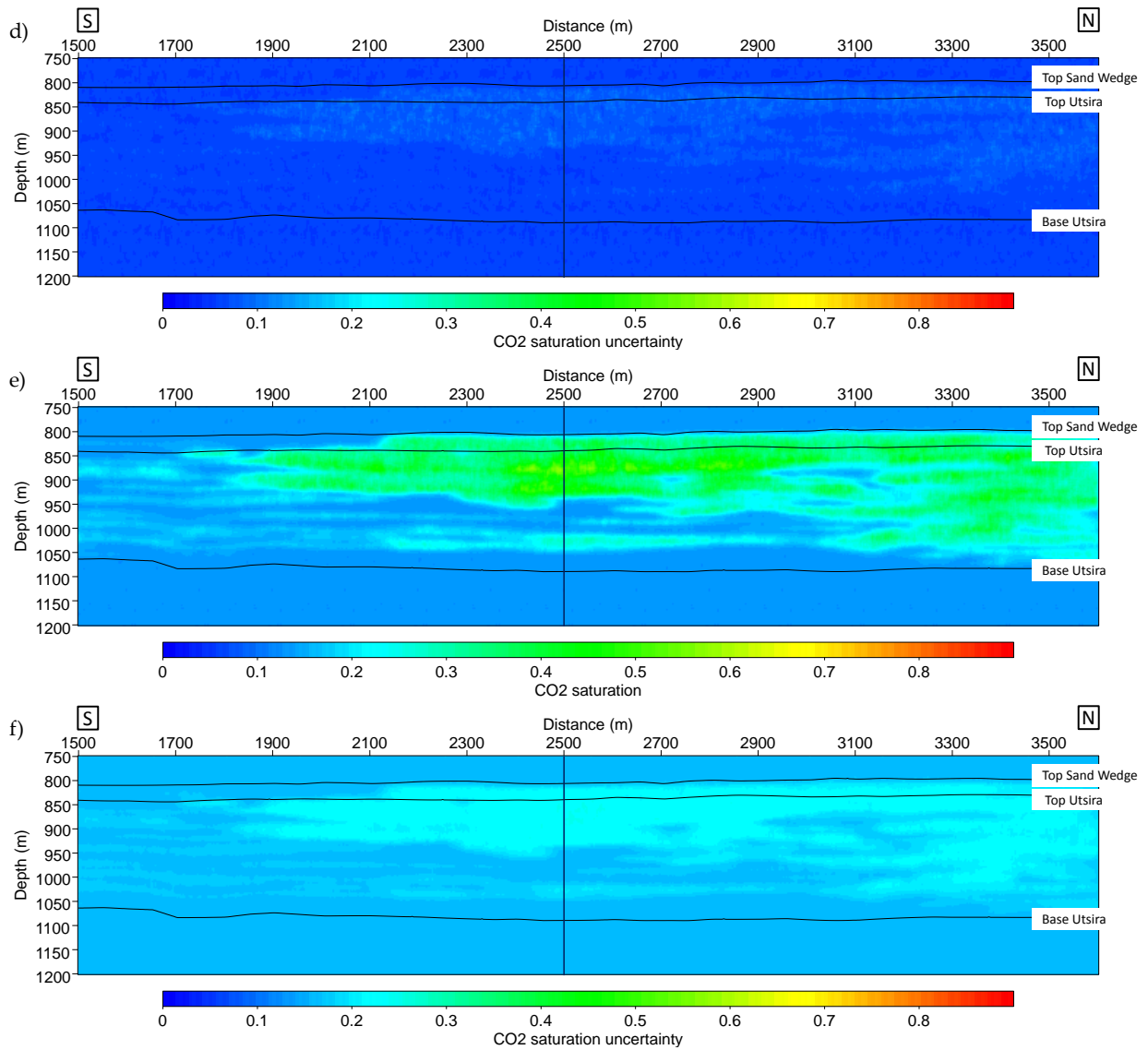
Figure 5.31: 2D profiles of (a & b) CO_2 saturation and uncertainty inverted using Vp, (c & d) CO_2 saturation and uncertainty inverted using Rt, (e & f) CO_2 saturation and uncertainty inverted using Vp + Rt.

1D profiles at x=2500 (black vertical line) are given in Figure 5.32. The Utsira formation is from depth 800 m to depth 1050 m

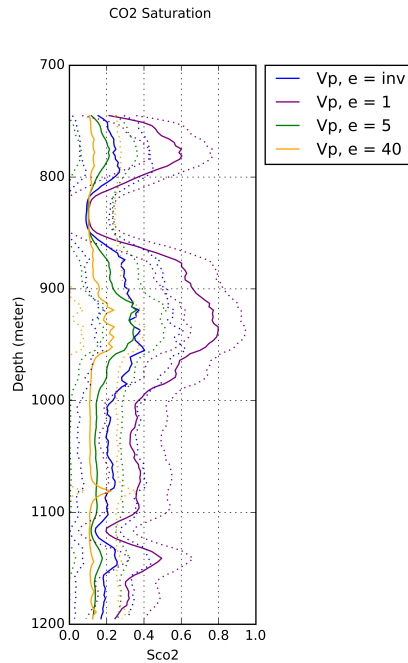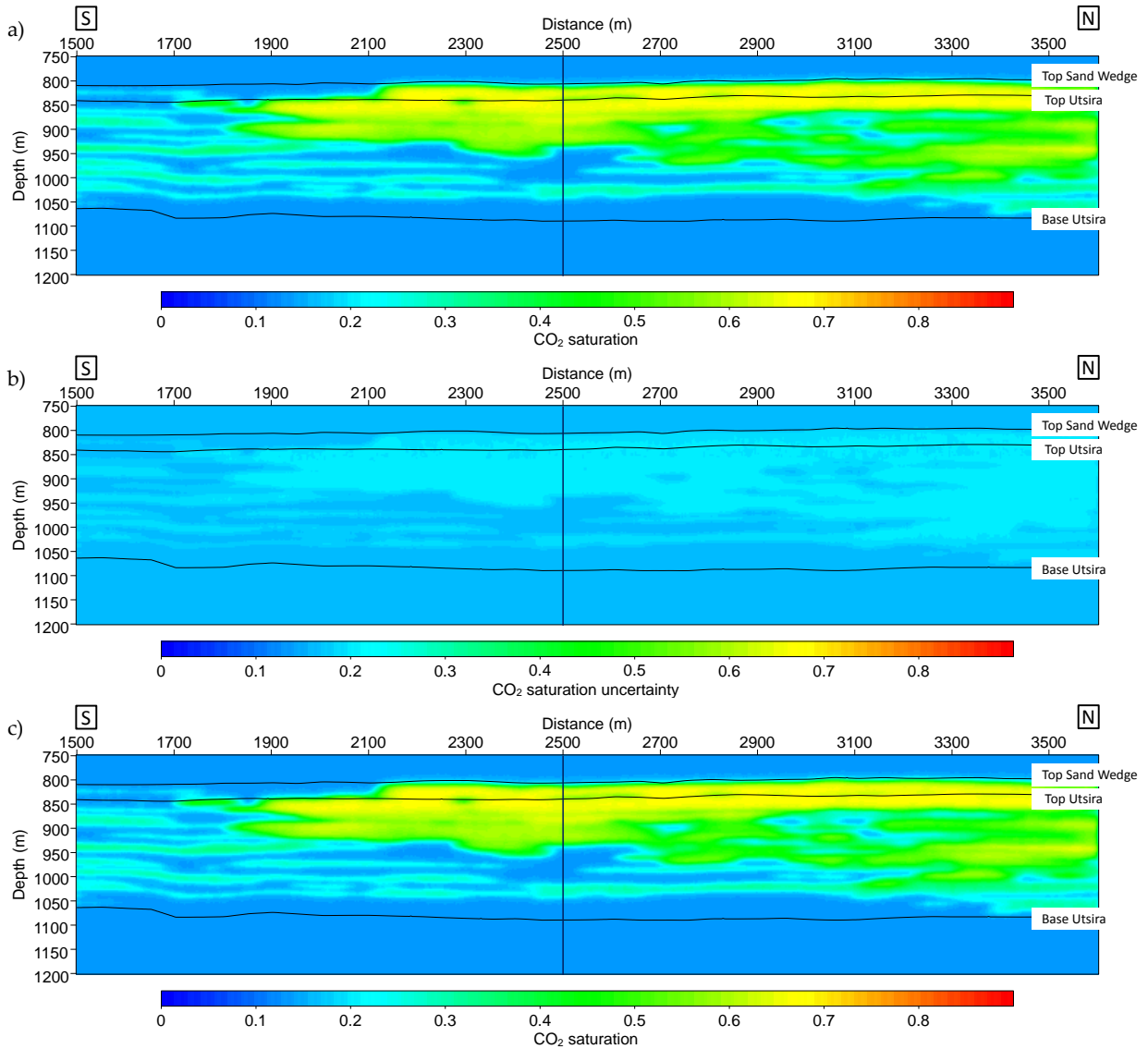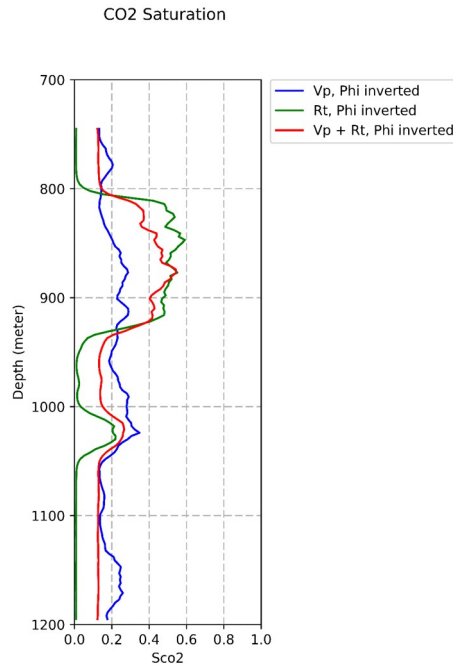**Figure 5.32:** Comparison of 1D profile of CO_2 saturation if porosity is inverted together at x=2500, inline 1838 using Vp, Rt, and Vp+Rt. The Utsira formation is from depth 800 m to depth 1050 m

It can be seen that CO_2 saturation inverted using Rt can reach 0% at depth 950 m to 1020 m. At the same depth, inversion using Vp estimate higher CO_2 saturation compare to saturation inverted using Rt and Vp+Rt. Both inversion using Rt and Vp+Rt estimate high CO_2 saturation ($> 30\%$) at depth 810 m to 910 m. Figure 5.33 shows the comparison of CO_2 saturation inverted from Vp, Rt, and Vp+Rt from two different scenarios. First is CO_2 saturation when porosity is inverted in the baseline model and the second is CO_2 saturation when porosity is inverted in the monitor model.
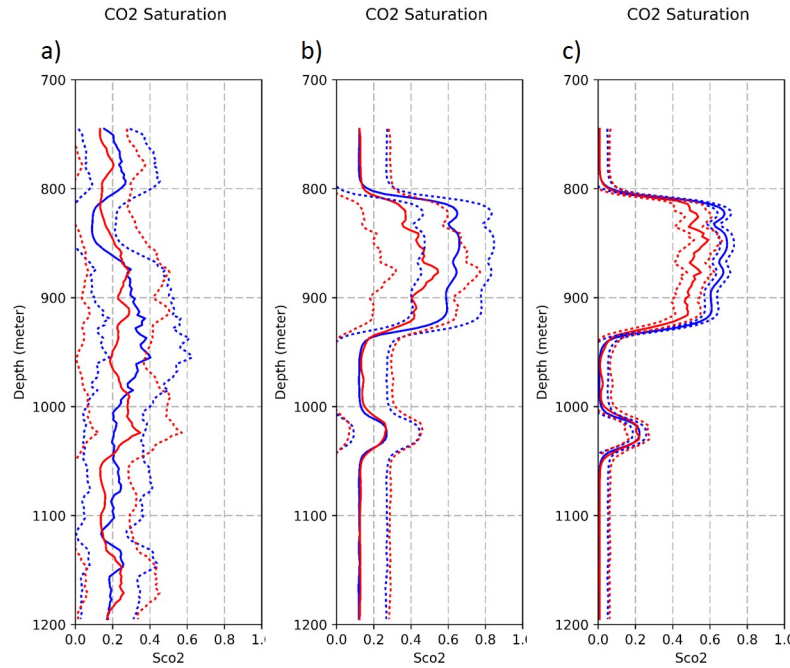
Figure 5.33: 1D profile of CO_2 saturation if porosity is inverted together at x=2500, inline 1838 using (a) Vp as input (b) Vp+Rt as input (c) Rt as input. Red curves are the CO_2 saturation if porosity is inverted together. CO_2 saturation if porosity is known (a priori) are also shown here for comparison (blue curves). The dotted line are the mean value plus minus uncertainty.

Figure 5.33 shows the comparison of CO_2 saturation if porosity is inverted together (red curve, Fig. 5.33) and CO_2 saturation when porosity is known (blue curve, Fig. 5.33). The Utsira formation is from depth 800 m to depth 1050 m. It shows that when inversion is using Vp as input, CO_2 saturation are ranging from 10% to 40%. This range is similar to that when porosity is not inverted together. When resistivity is added (Vp+Rt) and porosity is inverted together, it shows reduction when CO_2 saturation is high. At low CO_2 saturation, the difference is small. Inversion using Rt reduces uncertainty quite considerably. When porosity is inverted together using Rt, the saturation is lower compare to that when porosity is known at the top part of formation (Depth 810 m - 920 m).

Estimation of porosity

This sub-chapter presents the 2D profiles of porosity if inverted together with CO_2 saturation and Brie exponent inverted from Vp, Rt, Vp+Rt (Figures 5.34a,c,e). Figures 5.34b,d,f show the uncertainty of the porosity inverted from Vp, Rt, Vp+Rt, respectively.
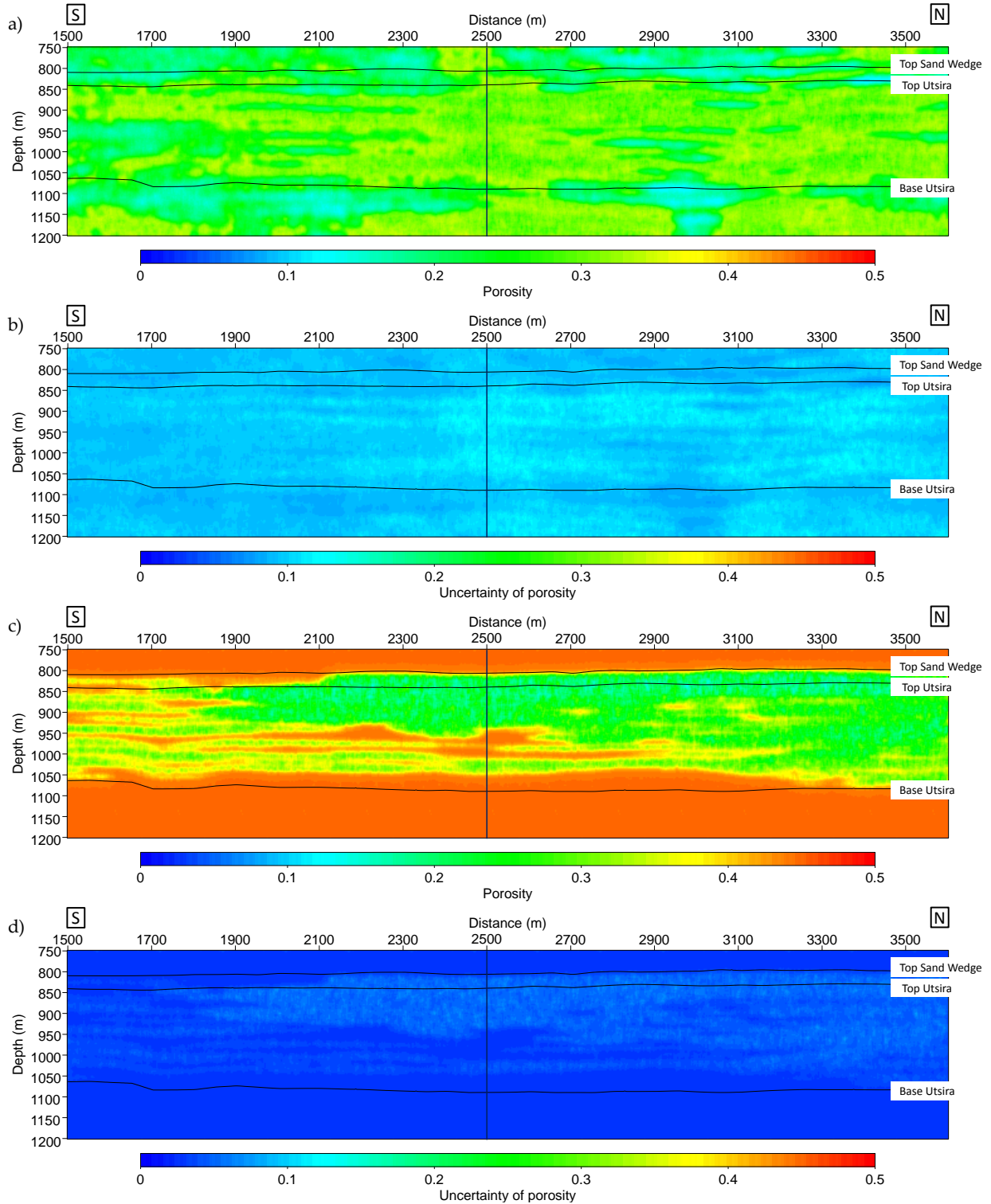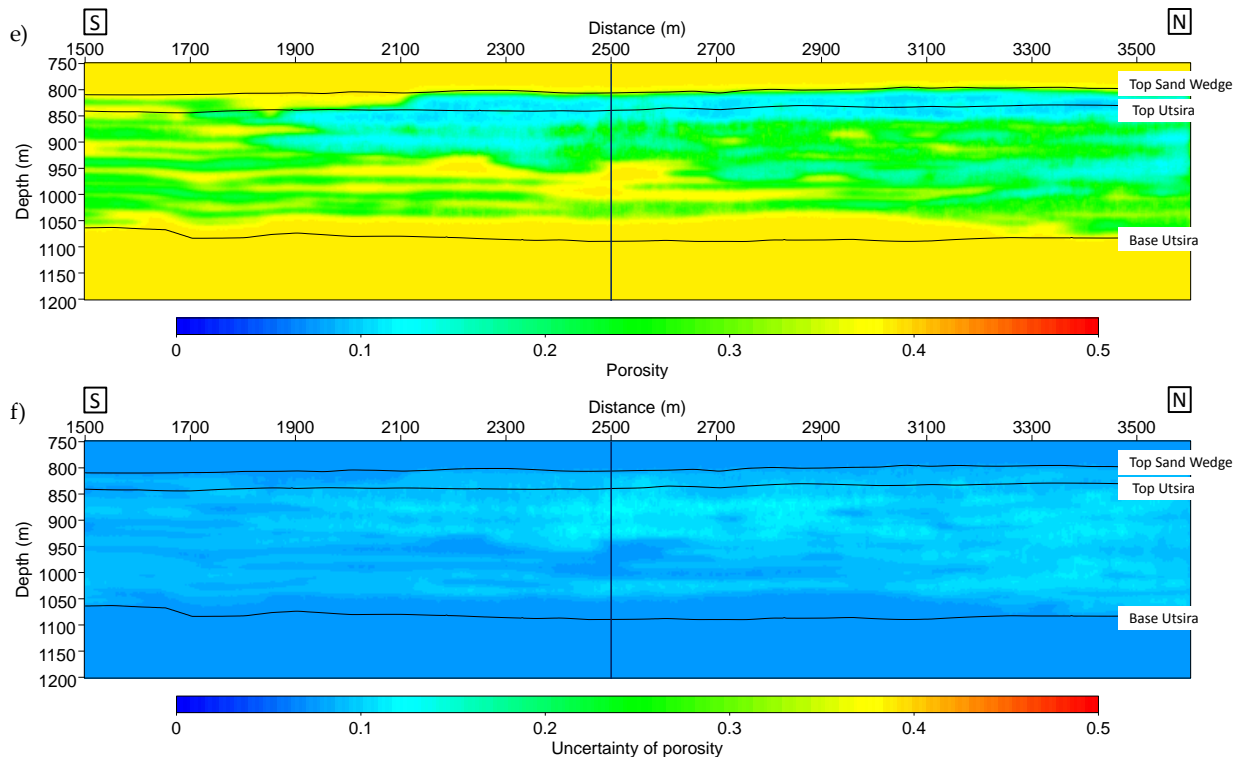
Figure 5.34: 2D profiles of porosity and uncertainty at inline 1838 if inverted together with CO_2 saturation and Brie exponent (a & b) Using Vp, (c & d) Using Rt, (e & f) Using Vp + Rt.

2D sections of porosity inverted Rt and Vp+Rt show that porosity trend is driven by resistivity as input. The Utsira formation is from depth 800 m to depth 1050 m. 1D profiles at x=2500 (black vertical line) are given in Figure 5.35.
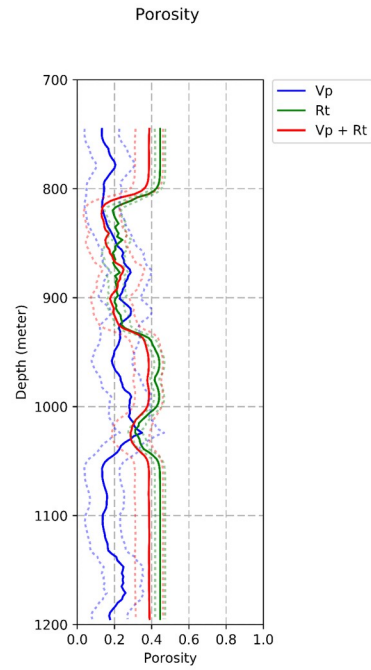
Figure 5.35: Comparison of 1D profiles of porosity if inverted together with CO_2 saturation and Brie exponent at x=2500, inline 1838 using Vp, Rt, and Vp+Rt. The dotted line are the mean value plus minus uncertainty.

Figure 5.35 shows that porosity inverted from Vp, Rt, and Vp+Rt are between 15% and 22% at depth 810 m to 910 m. After depth 925 m, the porosity inverted from Rt and Vp+Rt increase to around 40%. The Utsira formation is from depth 800 m to depth 1050 m.

Estimation of Brie exponent (e)

This sub-chapter presents the 2D profiles of Brie exponent if inverted together with CO_2 saturation and porosity.
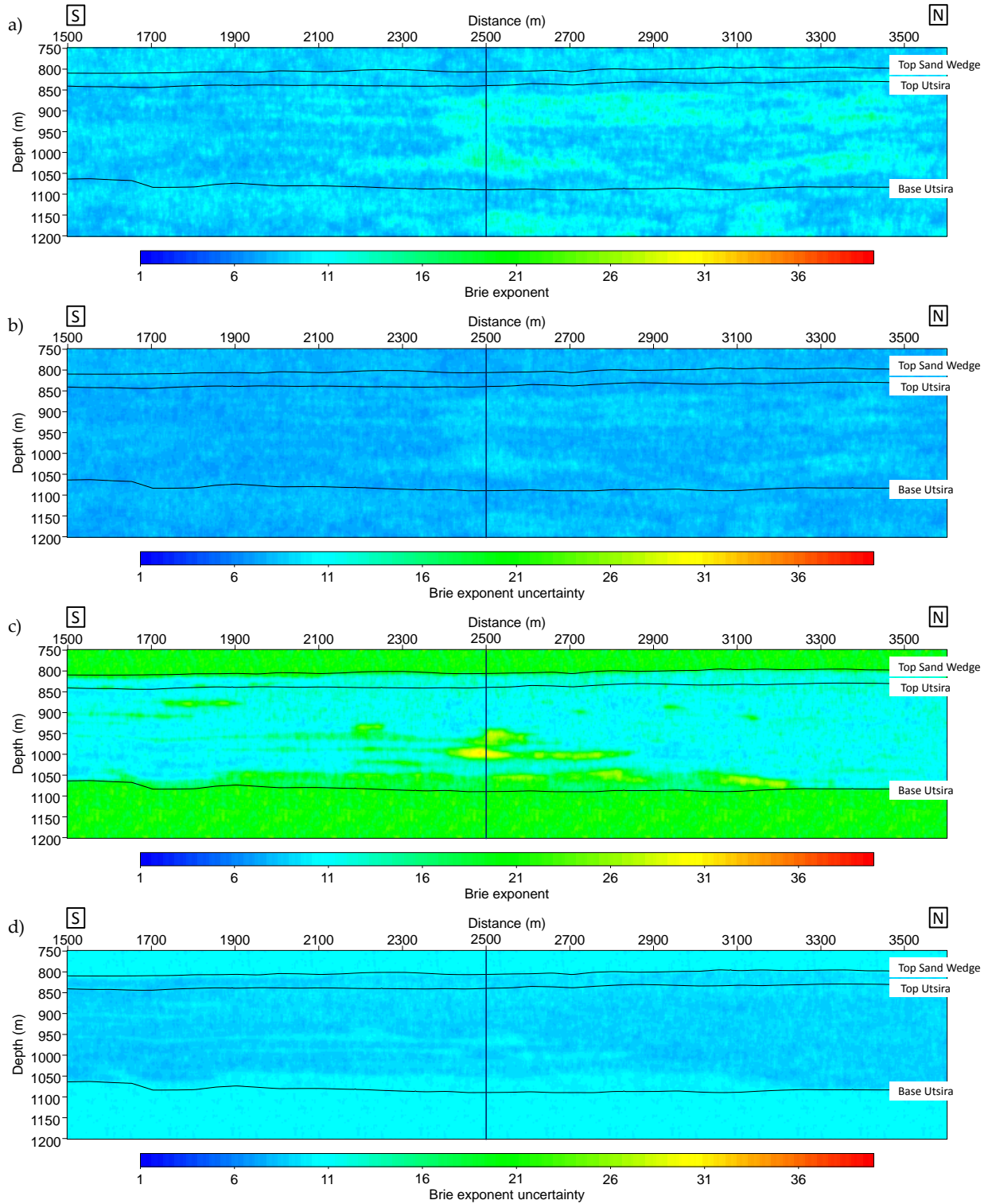
Figure 5.36: 2D profiles of Brie exponent (e) at inline 1838 if porosity inverted together with CO_2 saturation and Brie exponent (a & b) Using Vp (c & d) Using Vp + Rt.

1D profiles at x=2500 (black vertical line) are given in Figure 5.37.
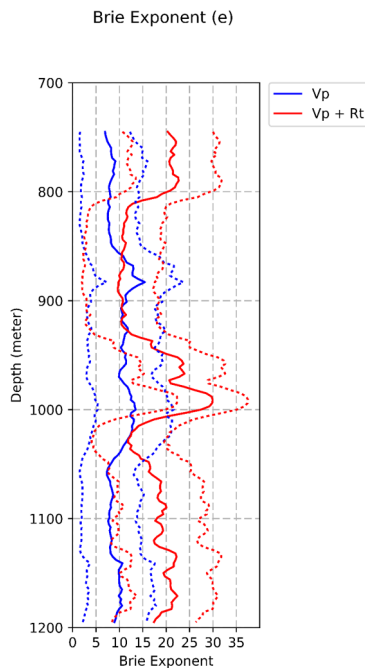
Figure 5.37: Comparison of 1D profiles of Brie exponent if inverted together with CO_2 saturation and porosity at x=2500, inline 1838 using Vp and Vp+Rt. The Utsira formation is from depth 800 m to depth 1050 m. The dotted line are the mean value plus minus uncertainty.

Figure 5.37 shows that Brie exponent inverted from Vp is ranging from 7 to 16, while Brie exponent inverted from Vp+Rt is ranging from 8 to 30. The uncertainty of Brie exponent inverted from Vp is between 4-10, while Brie exponent inverted from Vp+Rt, the uncertainty is between 6 and 12.

This scenario is also applied for Inline 1874. For brevity, the figures are given in Appendix G. Figure G.1 shows the 2D profiles of CO_2 saturation inverted using this scenario. Figure G.3 shows the 2D profiles of porosity inverted using this scenario. Figure G.5 shows the 2D profiles of Brie exponent inverted using this scenario. Figures G.2, G.4, and G.6 show the 1D profiles taken at x=3200 at Inline 1874 for CO_2 saturation, porosity, and Brie exponent, respectively.

6 Discussions

6.1 CO$_2$ Saturation

In this study, some tests have been conducted to quantify the CO$_2$ saturation and analyze the distribution type of the CO$_2$ and brine mixture inside the reservoir. The estimation of saturation CO$_2$ is conducted by several tests and the results are summarized in Table 6.1. Input for inversion is crucial in estimating CO$_2$ saturation. Several tests show that saturation of CO$_2$ becomes high when Rt is involved as input. CO$_2$ saturation inverted using Vp is, in general, smaller than CO$_2$ saturation when Rt is involved as input. When porosity is inverted together with saturation and Brie exponent, CO$_2$ saturation decreases. All inversions using Rt, Vp, and Vp + Rt show lower CO$_2$ saturation (Test 2,4,9, Table 6.1) compared to CO$_2$ saturation if porosity is known (Test 1,3,8, Table 6.1).

These tests show that porosity has a strong effect in estimating CO$_2$ saturation and should be well estimated. In general, porosity inverted from this scenario is lower than porosity inverted in the baseline model, especially at the top of formation (Figure 6.1). Table 6.2 shows highest porosity values inverted from different scenario at inline 1838 and inline 1874.
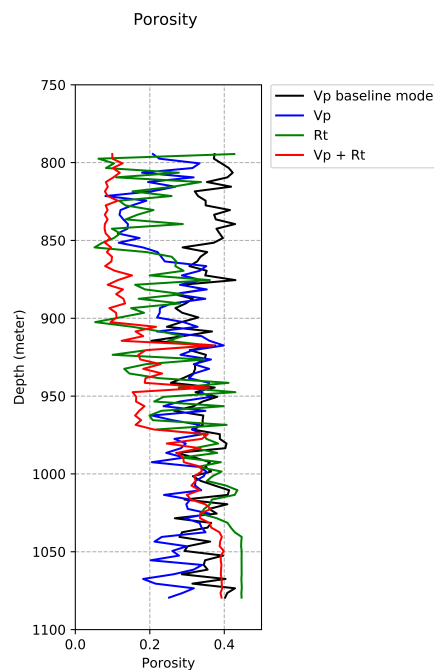
Figure 6.1: Comparison of 1D profiles of porosity derived in the baseline model and monitor model

Table 6.1: CO_2 saturation results under different inversion scenario. The CO_2 saturation shown in the table are the highest saturation and uncertainty at Inline 1838 and Inline 1874.

Test	Input	Inverted Parameter	CO_2 saturation & uncertainty (Inline 1838)	References	CO_2 saturation & uncertainty (Inline 1874)	References
1	Rt	S_{CO2}	72% ±5%	Figures 5.21c and 5.21d	70% ±5%	Figures 5.24c and 5.24d
2	Rt	S_{CO2}, ϕ	63% ±13%	Figures 5.31c and 5.31d	62% ±11%	Figures G.1c and G.1d
3	Vp	S_{CO2}, e	53% ±25%	Figures 5.21a and 5.21b	45% ±18%	Figures 5.24a and 5.24b
4	Vp	S_{CO2}, e, ϕ	40% ±29%	Figures 5.31a and 5.31b	54% ±25%	Figures G.1a and G.1b
5	Vp (e=1)	$S_{CO2},$	88% ±17%	Figure 5.27a and 5.27b	81% ±18%	Figure E.1a and E.1b
6	Vp (e=5)	S_{CO2}	60% ±17%	Figures 5.27c and 5.27d	45% ±17%	Figures E.1c and E.1d
7	Vp (e=40)	S_{CO2}	50% ±19%	Figures 5.27e and 5.27f	40% ±19%	Figures E.1e and E.1f
8	Vp and Rt	S_{CO2}, e	68% ±20%	Figures 5.21e and 5.21f	66% ±17%	Figures 5.24e and 5.24f
9	Vp and Rt	S_{CO2}, e, ϕ	57% ±25%	Figures 5.31e and 5.31f	60% ±25%	Figures G.1e and G.1f
10	Vp and Rt (e=1)	S_{CO2}	67% ±21%	Figures 5.29a and 5.29b	66% ±20%	Figures F.1a and F.1b
11	Vp and Rt (e=5)	S_{CO2}	68% ±21%	Figures 5.29c and 5.29d	67% ±20%	Figures F.1c and F.1d
12	Vp and Rt (e=40)	S_{CO2}	68% ±20%	Figures 5.29e and 5.29f	66% ±21%	Figures F.1e and F.1f

Table 6.2: Porosity (ϕ) results under different inversion scenario. The ϕ shown in the table are the highest ϕ and uncertainty value at Inline 1838 and Inline 1874.

No	Input	Inverted Parameter	Porosity (ϕ) (Inline 1838)	References	Porosity (ϕ) (Inline 1874)	References
1	Rt	S_{CO2}, ϕ	0.44 $\pm$0.07	Figures 5.31c and 5.31d	0.37 $\pm$0.07	Figure G.3c and G.3d
2	Vp	S_{CO2}, e, ϕ	0.33 $\pm$0.12	Figures 5.31a and 5.31b	0.36 $\pm$0.13	Figure G.3a and G.3b
3	Vp and Rt	S_{CO2}, e, ϕ	0.38 $\pm$0.12	Figures 5.31e and 5.31f	0.33 $\pm$0.12	Figure G.3e and G.3f
4	Vp (baseline model)	K_D, G_D, ϕ	0.42 $\pm$0.15	Figures 5.19e and 5.19f	0.39 $\pm$0.15	Figure 5.20e and 5.20f

If Vp is used as input, Brie exponent plays important role in estimating saturation. If e is inverted, CO_2 saturation can reach 53%. The inversion considering fully patchy mixing distribution ($e=1$) results in high CO_2 saturation (88%), while for perfect uniform mixing distribution ($e=40$), the inverted saturation becomes low (50%). The inversion result if saturation and Brie exponent are inverted simultaneously is similar to the result if e is equal to 5, suggesting that the fluid mixing type in Utsira is somewhere between uniform and patchy. However, when Rt is added, Brie exponent have less effect on saturation estimates. All CO_2 saturations using Vp + Rt with fixed Brie exponent ($e=1,5,40$) and when e is inverted show that the trend of CO_2 plume and maximum CO_2 saturation are almost similar ($\pm68\%$). It shows that resistivity as input is dominating CO_2 saturation estimation.

In general, CO_2 saturation at Inline 1838 is higher than at Inline 1874. Figures 5.15 and 5.18 show that CO_2 saturation inverted from Vp + Rt in point B (crosspoint of CSEM and seismic inline 1874) is lower than that in point A (Inline 1838). This can be explained as the distance from injection point to point B is 1380 m, while to point A is 433 m. However, at x=2500 m in inline 1838, CO_2 saturation inverted from Vp + Rt (Figure 5.23, red curve) is, mainly, lower than at x=3200 m in inline 1874 (Figure 5.26, red curve) although the distance is closer to the injection point. This is probably related to CO_2 lateral movement below the thin shale layers before encountering a higher permeability area to migrate vertically. The time-lapse seismic data shows that CO_2 movement tend to follow the topography of the formation (Furre et al., 2017). After several years, CO_2 spreads and accumulates below a structural high at 3 km North-East of the injection point (Furre et al., 2017).

6.2 Fluid mixing type

A study by (Bergmann & Chadwick, 2015) shows that once a region has been swept by CO_2, its permeability to CO_2 flow will increase, leading to a real reduction of CO_2 saturation in the deeper reservoir. The loss of CO_2 in the deeper part can cause a change in the vertical distribution of the CO_2 saturation in the plume (Bergmann & Chadwick, 2015), suggesting the fluid mixing characteristic is varying over time and space.

To understand the trade-off between fluid saturation and its mixing type in Utsira, CO_2 saturation and Brie exponent are plotted together in Figure 6.2. Each dot represents inverted CO_2 saturation and Brie exponent value at the same depth. The red dots in Figure 6.2a are the inversion results from Vp and Rt in point A and the blue dots are the inversion results from Vp. Figure 6.2b shows the same plot for point B.
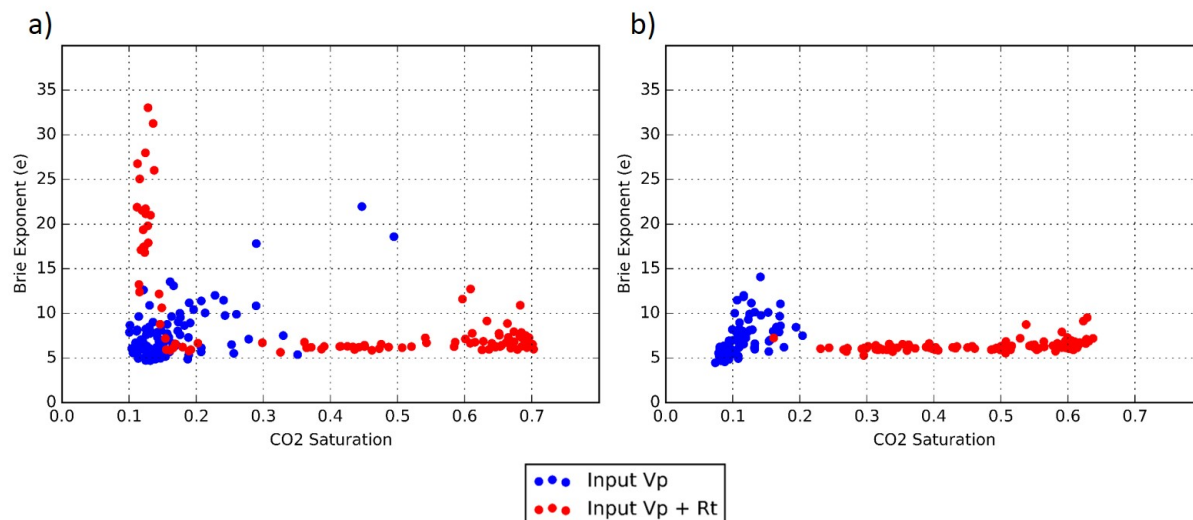
Figure 6.2: CO_2 saturation vs Brie Exponent at (a) Point A and (b) Point B. Blue dots represent the inversion result using Vp only and red dots represent the inversion result using Vp and Rt.

While the inversion results from Vp are difficult to distinguish the saturation from its mixing type, inversion results using Vp and Rt show clear separation in CO_2 saturation where the saturation above 15% is associated to Brie exponent (e) between 6 and 9. This is supported by the same plot in point B. Here, the CO_2 saturation is always above 15% and the Brie exponent is ranging between 6 and 8, similar to that in point A. For low CO_2 saturation (10%-13%) in point A, Brie exponent is rather difficult to determine, ranging from 12 to 32. The same plots for x=2500 in inline 1838 and x=3200 m in inline 1874 are given in Appendix H (Figure H.1). In the case where porosity is inverted together with saturation and Brie exponent, the inversion system using Vp + Rt as input becomes under-determined and CO_2 saturation is lower than that when the system is well-determined. In this scenario, both inversions using Vp and Vp + Rt show that Brie exponent is more disperse and the relationship between saturation and Brie exponent becomes unclear (Figure 6.3).
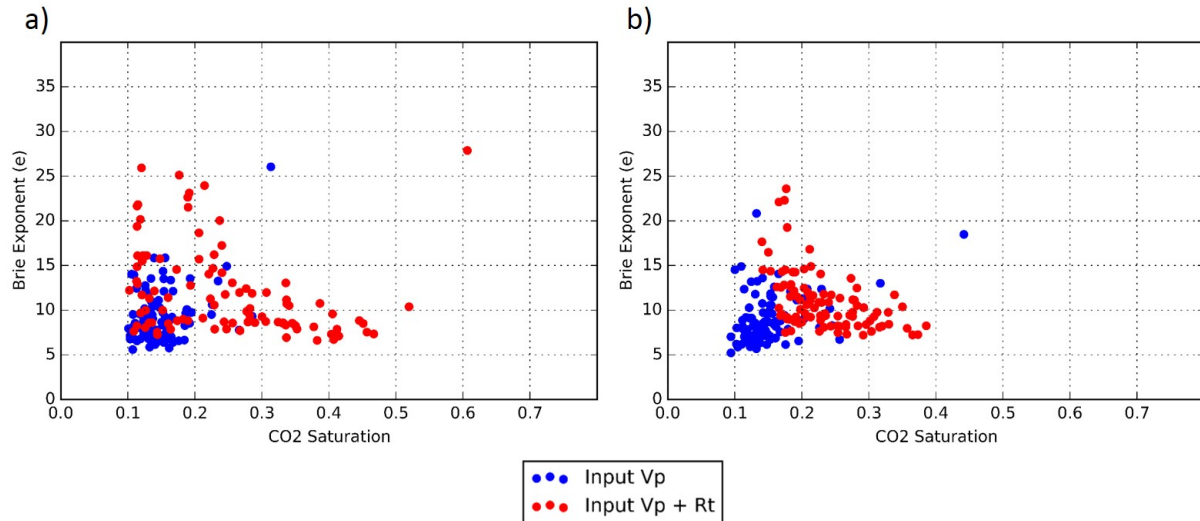
Figure 6.3: CO_2 saturation vs Brie Exponent at (a) Point A and (b) Point B when phi inverted together. Blue dots represent the inversion result using Vp only and red dots represent the inversion result using Vp and Rt.

Other plots are used to see the trade-off between Brie exponent and porosity inverted in the monitor model (Figure 6.3). Both inversion results using Vp and Vp + Rt in point A and point B are not showing strong correlation. Table 6.3 shows the estimation of Brie exponent under several inversion system.
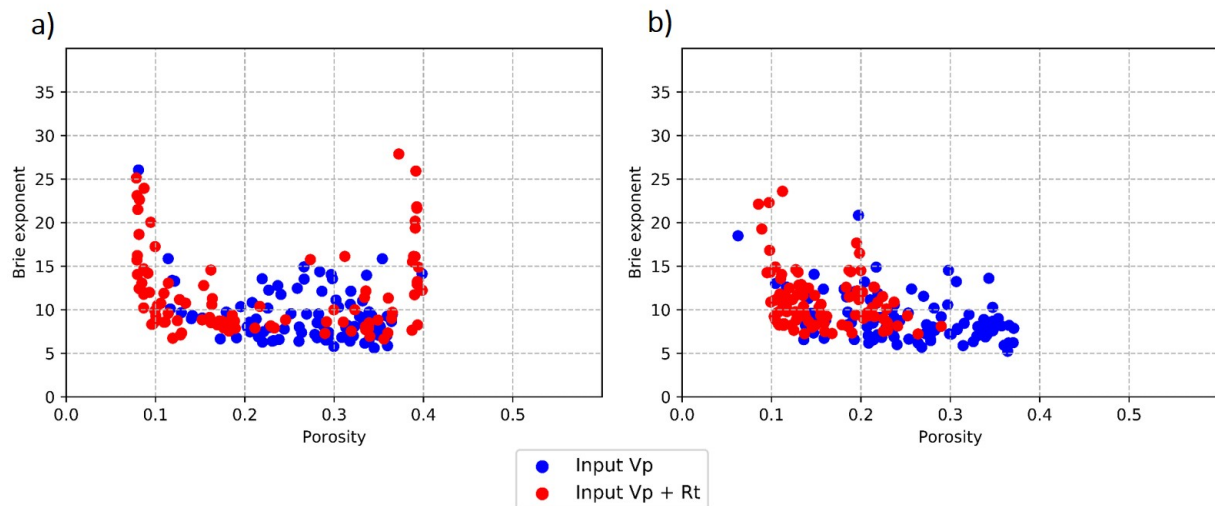
Figure 6.4: Brie Exponent vs Porosity inverted at the monitor model at (a) point A and (b) point B. Blue dots represent the inversion result using Vp and red dots represent the inversion result using Vp and Rt.

Table 6.3: Brie exponent (e) under different inversion scenario

No	Input	Inverted Parameter	Brie exponent (Point A)	References	Brie exponent (Point B)	References
1	Vp	S_{CO2}, e	5-10 for S_{CO2} 10% - 20%	Figure 6.2a	4-14 for S_{CO2} 8% - 20%	Figure 6.2b
2	Vp	S_{CO2}, ϕ, e	5-15 for S_{CO2} 10% - 20%	Figure 6.3a	5-15 for S_{CO2} 10% - 20%	Figure 6.3b
3	Vp and Rt	S_{CO2}, e	±7 for $S_{CO2} > 15\%$	Figure 6.2a	±7 for $S_{CO2} > 13\%$	Figure 6.2b
4	Vp and Rt	S_{CO2}, ϕ, e	5-26 for S_{CO2} 10% - 50%	FIgure 6.3a	7-23 for S_{CO2} 15% - 40%	Figure 6.3b

This test shows that the fluid mixing type of CO_2 and brine in Utsira is somewhere between uniform and patchy (Dupuy et al., 2017). It suggests that when CO_2 saturation in an area is lower than 15%, the Brie exponent is rather difficult to define. When this area is flooded by CO_2, the saturation increases. When it exceeds around 15%, Brie exponent decreases and become more constant (± 7). The uncertainty of Brie exponent is quite similar for both inversions using Vp and Vp + Rt. The range of uncertainty is from 5 to 11.

Combination of Vp and Rt is good to estimate Brie exponent. This is under one condition, the inversion system should be well-determined. The reason for this is that there are two inputs (Vp + Rt) and two inverted parameters (saturation and e). Brie exponent cannot be recovered by Rt because it is not included in Archie model used in the inversion. In this case, Rt is responsible to estimate only fluid saturation while Vp is looking for the best Brie exponent. This is probably why the saturation resulted from this scenario is highly influenced by resistivity.

6.3 A priori information and uncertainty analysis

All the inversion results (porosity and/or saturation) using Rt as input show low uncertainty. One reason is because resistivity from Archie model that is used to estimate CO_2 saturation is linked to only four parameters (R_w, m, n,ϕ). If these parameters are known, the calculation is more linear (compare to the one with Vp as input) and reduce uncertainty. In addition, Archie model does not take into account CO_2 properties (K_{CO2}, ρ_{CO2}, and η_{CO2}). When Vp is added, more parameters are involved and could lead the solutions to converge towards local minima which induces the uncertainty to increase.

Previous studies show that the inversion system should be well determined to estimate reservoir parameters more easily (Subagjo, 2017), (Yan, 2017), (Dupuy et al., 2016). One test has been done to see the effect of porosity as a priori information in the inversion. As previously discussed, when porosity is inverted simultaneously with saturation and Brie exponent, CO_2 saturation drops. Another test shows that when porosity is known, the inversion system becomes well-determined (Vp+Rt to invert saturation and Brie exponent), and the inversion is capable to distinguish Brie exponent based on CO_2 saturation. This shows that the sensitivity of the inversion result is dominantly controlled by frame properties which need to be estimated in a proper way. If porosity is inverted in the monitor model, the inversion system become under-determined. However, the inversion results is not dependent on fixed values (inverted from the baseline) which may be wrong and drive the inversion towards local minima. Another solution is by inverting these parameters in the baseline model. Even though the inversion system is under-determined in the baseline model (Vp to invert K_D, G_D, ϕ), it is better than to invert all parameters in the monitor model. When porosity is known, the estimation of saturation and Brie exponent shows lower uncertainty than if porosity is inverted together, regardless the input (Table 6.1).

Different method is used to define other poroelastic parameters (K_S, ρ_S, and k0). Knowing that the system will be highly under-determined if these parameters are inverted simultaneously, another approach has been used. In this study, Hashin-Shtrikman method (Hashin & Shtrikman, 1963) and volume weighted average (Appendix B) are used to esti-

mate K_S and ρ_S based on mineral composition of Utsira sandstone (Appendix A). Shale content (V_{shale}) from the log is then used to define and propagate these parameters inside the reservoir. In addition to that, some parameters are defined as constants because the influence in the inversion is insignificant, such as cementation factor (m), saturation exponent (n), and water resistivity (R_W) (Subagjo, 2017).

7 Conclusions

Combination of different geophysical methods in CO_2 monitoring are useful because of different contribution from each method. This is because physical properties of materials inside reservoir are generally interconnected and have different sensitivities (Dell'Aversana, 2014). This study shows how the combination of resistivity attribute derived from CSEM inversion and velocity attribute from FWI can collaborate to reveal information regarding to CO_2 saturation inside Utsira sandstone.

CSEM method work in the low frequency domain. Therefore, the resistivity resolutions (both vertical and horizontal) are more limited compared to P-wave velocity model. This is also because P-wave velocity used in this study is derived from full-waveform inversion which can help in better characterizing the CO_2 layers velocities and thicknesses (Romdhane & Querendez, 2014). P-wave velocity alone is not without weakness. Brie exponent that is used to define the way two fluids are mixing inside the reservoir is not well recovered if the inversion only use Vp as input. In this study, P-wave velocity and resistivity are jointly inverted to estimate fluid porosity and Brie exponent. It shows that CO_2 saturation and its mixing type inside reservoir can be accurately estimated using Vp and Rt as input in joint inversion.

One of the joint optimization problem is the big number of parameters that must be solved simultaneously (Dell'Aversana, 2014). This can cause huge non-linearity in the inversion. To circumvent, the use of a priori information (for example logs from well 15/9-13) is optimized to limit the possible solutions from inversion.

The joint inversion of P-wave velocity and resistivity shows that the CO_2 saturation at Inline 1838 can reach 68% with uncertainty of around 20%. At the location far from the injection point, CO_2 saturation reach 66% with uncertainty around 17%. If porosity is inverted together with saturation and Brie exponent, CO_2 saturation decreases to 57% at inline 1838 and 60% at inline 1874. However the uncertainty increases to 25% in both location. The Brie exponent (e) for CO_2 saturation higher than 15% is around 7, suggesting the fluid mixing type between CO_2 and brine is somewhere between patchy and uniform.

7.1 Recommendations

The research that has been conducted for this thesis has suggested several recommendations on which further research would be beneficial. First, in this thesis 3D propagation of resistivity based on reservoir model has been performed due to lack of information for 2D joint inversion. The uncertainty related to this process is not discussed in this thesis but it is not negligible. One solution is to perform 3D full-waveform inversion (FWI) to derive P-wave velocity cube. The 2D P-wave velocity model can be extracted at the same location as the CSEM survey and joint inversion can be performed using data that are represent the actual responds from the subsurface. In addition, it is clear that CO_2 accumulation can be observed from the P-wave velocity model. Using the 3D model, it is

possible to quantify CO_2 volume inside reservoir. The volume can be used as constraint in the inversion which can reduces uncertainty.

The other way to reduce uncertainty is by combining the rock physics inversion with Bayesian approach. It is well-known that in inversion, the relationship of data and model is non-linear. This non-linearity can leads the solution to converge to multiple minima. In Bayesian approach, the solution to the inverse problem is the posterior probability density function (PDF). PDF is used to represent all information available on the model (Sambridge, 1999b). Here, all models computed during optimization are considered contain information and can help to reduce uncertainty of inversion result.

Last, the use of different geophysical methods in monitoring reservoir. Gravity method are useful to monitor density changes. Even though gravimeters need repeated measurements due to instrumental drift (Furre et al., 2017), gravity method provides high frequency information about density distribution (Dell'Aversana, 2014). Due to its linear relationship with saturation, the combination of density model derived from gravity method and P-wave velocity can reduce the uncertainty in joint rock physics inversion.

Nomenclature

η Effective Viscosity (Pa.s)

η_W Viscosity of brine (Pa.s)

η_{CO2} Viscosity of CO_2 (Pa.s)

$\gamma(\omega)$ Auxiliary parameter

ω Angular frequency (Hertz)

ω_C Critical angular frequency (Hertz)

ϕ Porosity (volume fraction)

ρ Bulk density (kg/m^3)

ρ_F Effective fluid phase density (kg/m^3)

ρ_S Grain Density (kg/m^3)

ρ_W Density of brine (kg/m^3)

ρ_{CO2} Density of CO_2 (kg/m^3)

d   Data vector

g   Non linear function linking data and model

m   Model vector

e Brie exponent

$k(\omega)$ Dynamic Permeability (m^2)

$\tilde{\rho}(\omega)$ Flow resistance density (kg/m^3)

C Biot's modulus

$C(\mathbf{m})$ Scalar misfit function

G Shear modulus (Pa)

G_D Shear modulus of drained rock (Pa)

G_S Shear modulus of solid frame of rock (Pa)

H P-wave modulus or uniaxial compaction modulus (Pa)

K Bulk modulus (Pa)

K_D Bulk modulus of drained rock (Pa)

K_F Bulk modulus of of pore fluid (Pa)

K_S Bulk modulus of solid frame of rock (Pa)

K_U Undrained bulk modulus (Pa)

K_W Bulk modulus of brine (Pa)

K_{CO2} Bulk modulus of CO_2 (Pa)

M Fluid storage coefficient

m Cementation factor

n Saturation exponent

Qp P-wave quality factor

Qs S-wave quality factor

R_T Formation resistivity (ohm.m)

R_W Water resistivity (ohm.m)

S_W Brine saturation

S_{CO2} CO_2 saturation

V_{shale} Shale content or Volume of shale

Vp Compressional velocity or P-wave velocity (m/s)

Vs Shear velocity or S-wave velocity (m/s)

References

Abubakar, A., Gao, G., & Habashy, T. (2012, April). Joint inversion approaches for geophysical electromagnetic and elastic full-waveform data. *Inverse Problems*, *28*(5).

Adler, P., Jacquin, C., & Thovert, J. (1992, June). The formation factor of reconstructed porous media. *Water Resources Research*, *28*(6), 1571-1576.

Archie, G. (1942, December). The electrical resistivity log as an aid in determining some reservoir characteristics. , *146*(1).

Arts, R., Chadwick, R., Eiken, O., Thibeau, S., & Nooner, S. (2008, January). Ten years experience of monitoring CO2 injection in the utsira sand at sleipner, offshore Norway. *First Break*, *26*, 65-72.

Arts, R., Eiken, O., Chadwick, A., Zweigel, P., Meer, B., & Kirby, G. (2004, March). Seismic monitoring at the sleipner underground co2 storage site (north sea). *Geological Society of London*, 181-191.

Avseth, P., Mukerji, T., & Mavko, G. (2005). *Quantitative seismic interpretation: Applying rock physics tools to reduce interpretation risk* (1st ed.). Cambridge.

Bergmann, P., & Chadwick, A. (2015, September). Volumetric bounds on subsurface fluid subtitution using 4d seismic time shift with an application at sleipner, north sea. *Geophysics*, *80*(5), B153-B165.

Bhuiyan, A., Landrø, M., & Johansen, S. (2012, September). 3D CSEM modeling and time-lapse sensitivity analysis for subsurface CO2 storage. *Geophysics*, *77*(5), E343-E355.

Bickle, M. J. (2009, December). Geological carbon storage. *Nature Geoscience*, *2*, 815–818.

BIGCCS. (2008). *International ccs research center.* Retrieved from `https://bigccs.no/`

Biot, M. A. (1956a, March). Theory of propagation of elastic waves in a fluid-saturated porous solid. ii. higher frequency range. *The Journal of The Acoustical Society of America*, *28*(2), 179-191.

Biot, M. A. (1956b, March). Theory of propagation of elastic waves in a fluid-saturated porous solid. i. low frequency range. *The Journal of The Acoustical Society of America*, *28*(2), 168-178.

Boait, F., White, N., Bickle, M., Chadwick, R., Neufeld, J., & H.Huppert. (2012). Spatial and temporal evolution of injected co2 at the sleipner field, north sea. *Journal of Geophysical Research:Solid Earth*, *117*.

Brie, A., Pampuri, F., Marsala, A., & Meazza, O. (1995, October). Shear sonic interpretation in gas-bearing sands. *SPE Annual Technical Conference And Exhibition*, 701-710.

Brown, R. J. (1980, August). Connection between formation factor for electrical resistivity and fluid-solid coupling factor in biot's equations for acoustic waves in fluid-filled porous media. *Geophysics*, *45*(8), 1269-1275.

Burridge, R., & Vargas, C. (1979, July). The fundamental solution in dynamic poroelasticity. *Geophysical Journal International*, *58*(1), 61-90.

Bøe, L. Z., Park, J., Vöge, M., & Sauvin, G. (2017). Filtering out seabed pipeline influence to improve the resistivity image of an offshore co2 storage site. *EAGE/SEG Research Workshop, Geophysical Monitoring of CO2 Injection CCS and CO2 EOR, Trondheim, Norway*.

Bøe, R., & Zweigel, P. (2001). *Characterization of the nordland shale in the sleipner area by xrd analysis-a contribution to the saline aquifer co2 storage (sacs) project.* (Tech. Rep.). SINTEF Industry.

Carcione, J., Picotti, S., Gei, D., & Rossi, G. (2006, October). Physics and seismic modeling for monitoring co2 storage. *Pure and Applied Geophysics*, *163*, 175-207.

Cavanagh, A., & Haszeldine, R. (2014, January). The sleipner storage site: Capillary flow modeling of a layered CO2 plume requires fractured shale barriers within the utsira formation. *International Journal of Greenhouse Gas Control*, *21*, 101-112.

Chadwick, R., Arts, R., Bernstone, C., May, F., Thibeau, S., & Zweigel, P. (2008). *Best practice for the storage of CO2 in saline aquifers - observations and guidelines from the SACS and CO2STORE projects* (1st ed.). British Geological Survey Occasional Publication.

Chadwick, R., & Eiken, O. (2014). *Geological storage of carbon dioxide CO2. chapter 10: Offshore CO2 storage: sleipner natural gas field beneath the north sea* (1st ed.). Woodhead Publishing Limited.

Chadwick, R., P.Zweigel, U.Gregersen, Kirby, G., S.Holloway, & Johannessen, P. (2004, July). Geological reservoir characterization of a CO2 storage site: The utsira sand sleipner, northern north sea. *Energy*, *29*(9-10), 1371-1381.

Chadwick, R., S.Holloway, Kirby, G., U.Gregersen, , & Johannessen, P. (2000, January). The utsira sand, central north sea - an assesment of its potential for regional co2 disposal. *Proceedings of the 5th International Conference on Greenhouse Gas Control Technologies (GHGT-5)*.

Dell'Aversana, P. (2014). *Integrated geophysical models: combining rock physics with seismic, electromagnetics, and gravity data* (1st ed.). EAGE Publications.

Dupuy, B., Garambois, S., A.Asnaashari, Balhareth, H. M., Landrø, M., A.Stovas, & J.Virieux. (2016, May). Estimation of rock physics properties from seismic attributes-part 1: Strategy and sensitivity analysis. *Geophysics*, *81*(3), M35-M53.

Dupuy, B., Romdhane, A., Eliasson, P., Querendez, E., Yan, H., Torres, V., & A, G. (2017, November). Quantitative seismic characterization of CO2 at the Sleipner storage site North Sea. *Interpretation*, *5*(4), SS23-SS42.

Dupuy, B., & Stovas, A. (2014, January). Influence of frequency and saturation on avo attributes for patchy saturated rocks. *Geophysics*, *79*(1), B19-B36.

Furre, A., A.Kjær, & Eiken, O. (2015, August). CO2-induced seismic time shifts at sleipner. *Interpretation*, *3*(3), 23-35.

Furre, A., & Eiken, O. (2014, April). Dual sensor streamer technology used in sleipner co2 injection monitoring. *Geophysical Prospecting*, *62*(5), 1075-1088.

Furre, A., Eiken, O., Alnes, H., Vevatne, J. N., & Kiær, A. F. (2017, july). 20 years of monitoring CO2 injection at sleipner. *Energy Procedia*, *114*, 3916-3926.

Gao, G., Abubakar, A., & Habashy, T. (2012, May). Joint petrophysical inversion of electromagnetic and full-waveform seismic data. *Geophysics*, *77*(3), WA3-WA18.

Gassmann, F. (1951, October). Elastic waves through a packing of spheres. *Geophysics*, *16*(4), 673-685.

Gaus, I., Azaroual, M., & Czernichowski-Lauriol, I. (2005, April). Reactive transport modeling of the impact of co2 injection on the clayey cap rock at sleipner (north sea). *Chemical Geology*, *217*(3-4), 319-337.

Ghaderi, A., & Landrø, M. (2009, March). Estimation of thickness and velocity changes of injected CO2 layers from prestack time-lapse seismic data. *Geophysics*, *74*(2),

o17-o28.

Ghosh, R., Sen, M., & Vedanti, N. (2015, January). Quantitative interpratation of co2 plume for sleipner (north sea), using post stack inversion and rock physics modeling. *International Journal of Greenhouse gas control*, *32*, 147-158.

Hashin, Z., & Shtrikman, S. (1963). A variational approach to the theory of the elastic behaviour of multiphase material. *Journal of the mechanics and physics of solids*, *11*, 127-140.

IEA. (2008, January). *Geologic storage of carbon dioxide* (Tech. Rep.). International Energy Agency : Greenhouse Gas Research and Development Programme.

Johnson, D. L., Koplik, J., & Dashen, R. (1987, March). Theory of dynamic permeability and tortuosity in fluid-saturated porous media. *Chemical Geology*, *176*, 379-402.

Krushin, J. (1997). Seal capacity of nonsmectite shale. *AAPG Memoir*, *67*, 31-47.

Lindeberg, E. (2013). *Calculation of thermodynamic properties of co2, h2o and their mixtures also including salt with the excel macro 'CO2 thermodynamics'* (Tech. Rep.). SINTEF Industry.

Lothe, A. E., & Zweigel, P. (1999). *Saline aquifer co2 storage (sacs) informal annual report 1999 of sintef petroleum research's results in work area 1 'reservoir geology'* (Tech. Rep.). SINTEF Industry.

Mavko, G., Mukerji, T., & Dvorkin, J. (1998). *Rock physics handbook: Tools for seismic interpretation in porous media* (1st ed.). Cambridge University Press.

Mosegaard, K., & Sambridge, M. (2002, April). Monte carlo analysis of inverse problems. *Inverse Problems*, *18*(3), R29-R54.

Park, J., Fawad, M., Viken, I., Aker, E., & Bjørnarå, T. I. (2013, November). CSEM sensitivity study for sleipner CO2 injection monitoring. *Energy Procedia*, *37*, 4199-4206.

Park, J., Sauvin, G., & Vöge, M. (2017, July). 2.5D inversion and joint interpretation of CSEM data at sleipner CO2 storage. *Energy Procedia*, *114*, 3989-3996.

Park, J., Sauvin, G., Vöge, M., & Vanneste, M. (2016, September). 2.5D inversion and joint interpretation of marine EM data at sleipner CO2 storage. *Near Surface Geoscience, Barcelona*.

Park, J., Viken, I., Bjørnarå, T. I., & Aker, E. (2011, June). CSEM data analysis for sleipner CO2 storage. *Trondheim CCS-6 Conference, Trondheim*.

Pride, S. (2005). *Hydrogeophysics: Water science and technology* (1st ed.). Springer.

Queißer, M., & Singh, S. (2013, May). Full waveform inversion in the time lapse mode applied to co2 storage at sleipner. *Geophysical Prospecting*, *61*, 537-555.

Romdhane, A., & Querendez, E. (2014). CO2 characterization at the sleipner field with full waveform inversion: application to synthetic and real data. *Energy Procedia*, *63*, 4358-4365.

Sambridge, M. (1998, March). Exploring multidimensional landscapes without a map. *Inverse Problem*, *14*(3), 427-440.

Sambridge, M. (1999a, September). Geophysical inversion with a neighbourhood algorithm-ii. appraising the ensemble. *Geophysical Journal International*, *138*(3), 727-746.

Sambridge, M. (1999b, August). Geophysical inversion with a neighbourhood algorithm-i. searching a parameter space. *Geophysical Journal International*, *138*(2), 479-494.

Stockwell, J. W. (2001). *Seismic unix home page.* Retrieved from `https://github.com/JohnWStockwellJr/SeisUnix/blob/master/src/su/tutorial/suname.tex`

Subagjo, I. (2017, December). *Sensitivity tests of joint rock physics inversion for CO2 characterization at sleipner* (Tech. Rep.). Norwegian University of Science and Technology.

Teja, A., & Rice, P. (1981, February). Generalized corresponding states method for the viscosities of liquid mixtures. *Industrial and Engineering Chemistry Fundamentals*, *20*(1), 77-81.

Yan, H. (2017, July). *Rock physics inversion for co2 characterization at sleipner* (Tech. Rep.). Norwegian University of Science and Technology : Master Thesis.

Appendix A   Mineralogical composition of the Utsira sandstone and Nordland shale

Table A.1: Mineral composition of Utsira sandstone and its Bulk moduli, shear moduli, and density. Source: (Chadwick et al., 2004)

Minerals	ρ_s (g/cc)	Volume percentage	Ks (GPa)		Gs (GPa)	
			low	high	low	high
Quartz	2.65	75%	36.5	37.9	44	45.6
Calcite	2.71	3%	63.7	76.8	28.4	32
Feldspar	2.62	13%	37.5	37.5	15	15
Albite	2.63	3%	75.6	75.6	25.6	25.6
Aragonite	2.92	3%	44.8	44.8	38.8	38.8
Mica (muscovite)	2.79	2%	42.9	61.5	22.2	41.1
Mica (biotite)	3.05	2%	41.1	59.7	12.4	42.3

Table A.2: Density and mineral composition of Nordland shale. The mineral composition is taken from (Gaus et al., 2005)

Minerals	ρ_s (g/cc)	Volume percentage
Plagioclase	2.68	12.3%
Calcite	2.71	1%
Quartz	2.65	21.5%
Chlorite	2.47	4.1%
Mica/Illite	2.75	24.7%
Kaolinite	2.60	18%
K-feldspar	2.62	2.1%
Pyrite	5.01	2.8%
Siderite	3.87	1.6%
Smectite	2.63	8.8%
Mixed layer clay		1.4%
Others		1.7%

Appendix B Grain's Bulk moduli and density computation at the Utsira sandstone

The upper bound K^{HS+} and G^{HS+} and lower bound K^{HS-} and G^{HS-} is the Hashin-Shtrikman bounds illustrated in Hashin and Shtrikman (Hashin & Shtrikman, 1963). The equations below are taken from the book Quantitative Seismic Interpretation: Applying Rock Physics Tools to Reduce Interpretation Risk (Avseth et al., 2005). A more general form of Hashin-Shtrikman-Walpole bounds are used to calculate the bounds of mixtures of more than two phases (Avseth et al., 2005). Mineral constituents and bounds moduli for Utsira sandstone and Nordland shale are shown in Appendix A (Table A.1 and Table A.2)

$$K^{HS+} = \Lambda(G_{max}); K^{HS-} = \Lambda(G_{min}) \tag{B.1}$$

$$G^{HS+} = \Gamma(G_{max}(\zeta(K_{max},G_{max})); G^{HS-} = \Gamma(G_{max}(\zeta(K_{min},G_{min})) \tag{B.2}$$

Where K_{max} and G_{max} are the maximum bulk and shear moduli of the individual constituents. K_{min} and G_{min} are the minimum bulk and shear moduli of the individual constituents. $\Lambda(z)$, $\Gamma(z)$ and $\zeta(K,G)$ are given by:

$$\Lambda(z) = \left\langle \frac{1}{K(r) + \frac{4}{3}z} \right\rangle^{-1} - \frac{4}{3}z \tag{B.3}$$

$$\Gamma(z) = \left\langle \frac{1}{G(r) + z} \right\rangle^{-1} - z \tag{B.4}$$

$$\zeta(K,G) = \frac{G}{6}\left(\frac{9K + 8G}{K + 2G} \right) \tag{B.5}$$

Where the brackets $\langle . \rangle$ indicate an average over the medium, which is the same as an average over the constituents weighted by their volume fractions.

Appendix C   1D profiles of CO_2 saturation, Brie exponent and porosity if inverted together
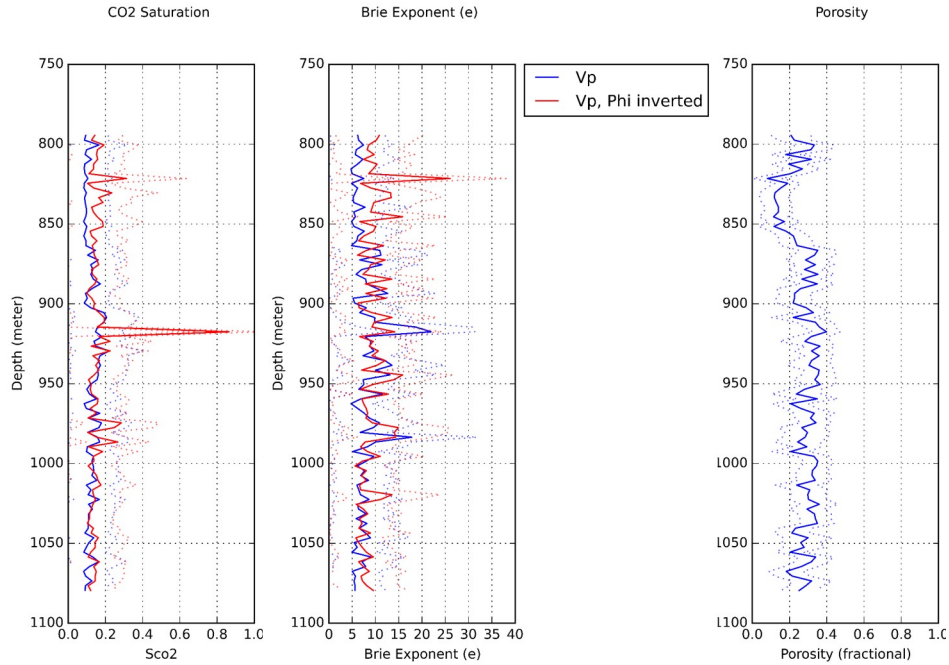
Figure C.1: CO_2 saturation (left), Brie exponent (centre), and porosity (right) inverted simultaneously from Vp at point A. The dotted line is the mean value plus minus standard deviation. In this case, porosity (right) is inverted together with CO_2 saturation and Brie exponent (e).
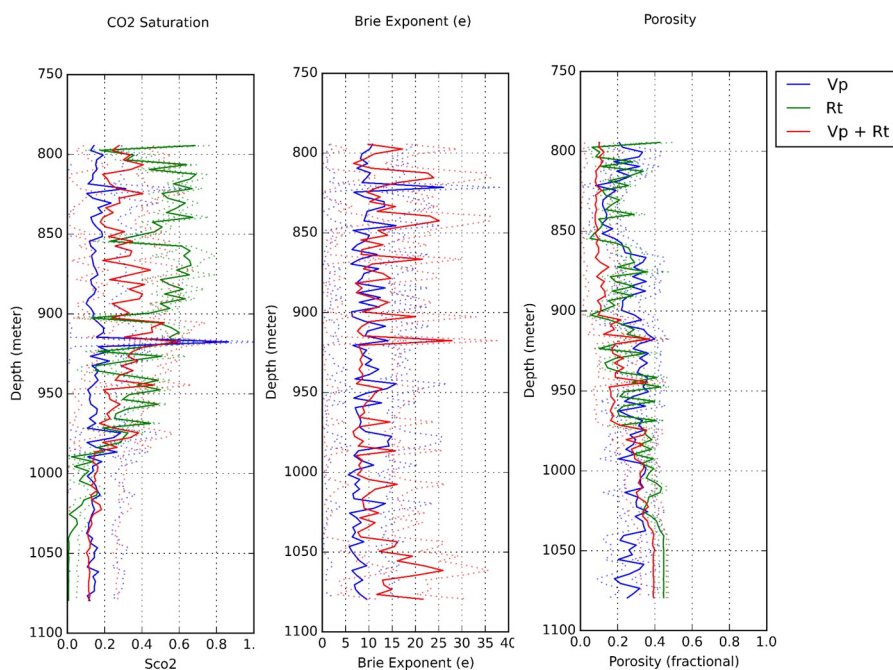
Figure C.2: CO$_2$ saturation (left), Brie exponent (centre), and porosity (right) inverted simultaneously from Vp (blue curve), Rt (green curve), and Vp+Rt (red curve) at point A. The dotted line is the mean value plus minus uncertainty. In this case, porosity (right) is inverted together with CO$_2$ saturation and Brie exponent (e).

Appendix D   2D profiles of a K_S, $k0$, and ρ_S at inline 1838 and inline 1874

3D cube of K_S, ρ_S, and $k0$ are computed using Equation 4.1, 4.2, and 4.3 from the 3D V_{shale} cube (Figure 4.4). Inline 1838 of K_S, $k0$, and ρ_S are sliced from the cubes and shown in Figure D.1
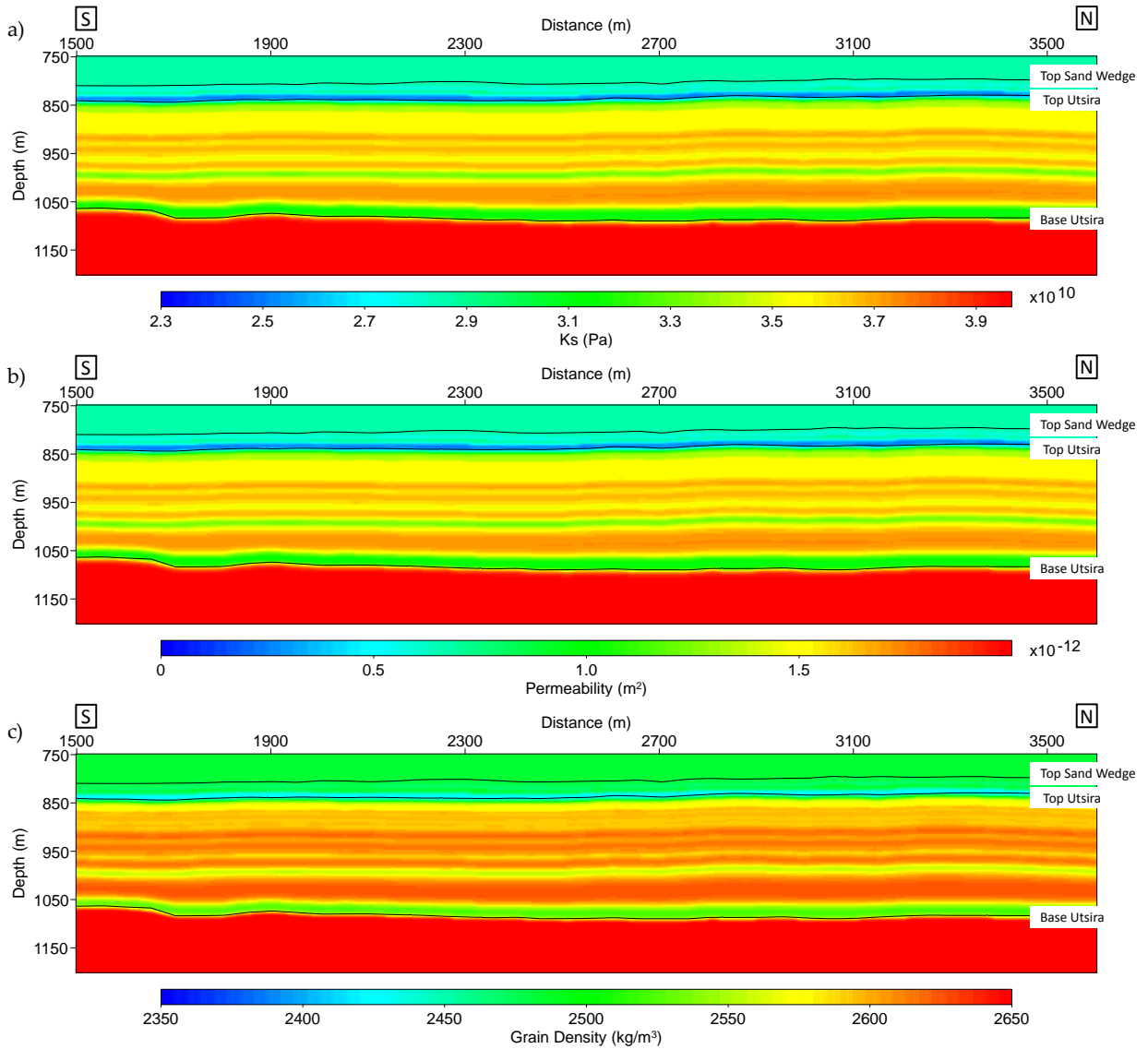
Figure D.1: 2D profile of (a) grain Bulk modulus (K_S), (b) permeability ($k0$), and (c) grain density (ρ_S) at inline 1838

D. 2D profiles of a K_S, $k0$, and ρ_S at inline 1838 and inline 1874

K_S, $k0$, and ρ_S for inline 1874 are shown in Figure D.2.
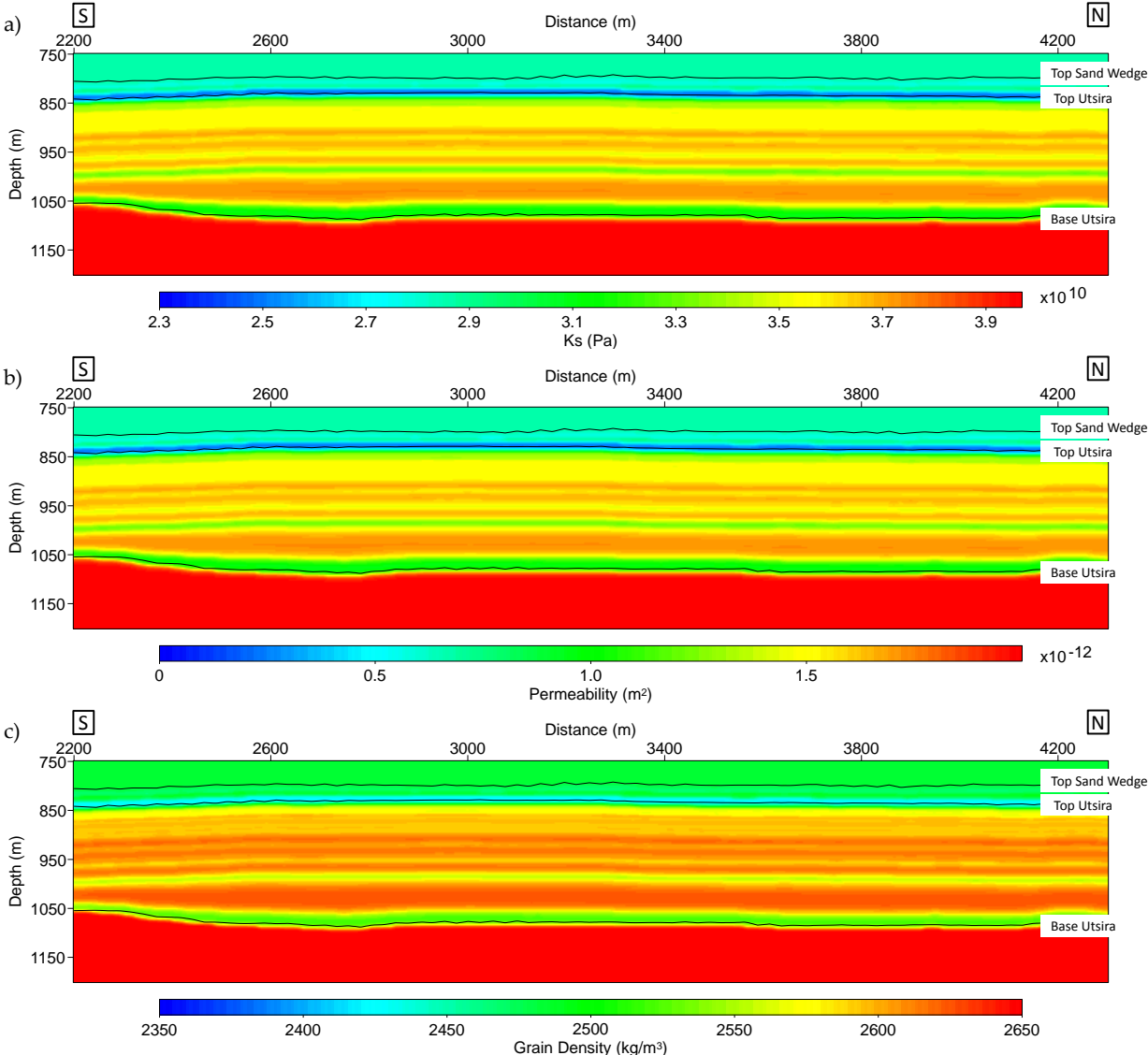
Figure D.2: 2D profile of (a) Grain Bulk modulus (K_S), (b) permeability ($k0$), and (c) grain density (ρ_S) at inline 1874

Appendix E Estimation of CO$_2$ saturation using Vp if Brie exponent (e) is constant (Inline 1874)

The 2D profiles of CO$_2$ saturation if Brie exponent is set as constant. Here, three values of e (1, 5, 40) are used and the inversion system become well-determined.
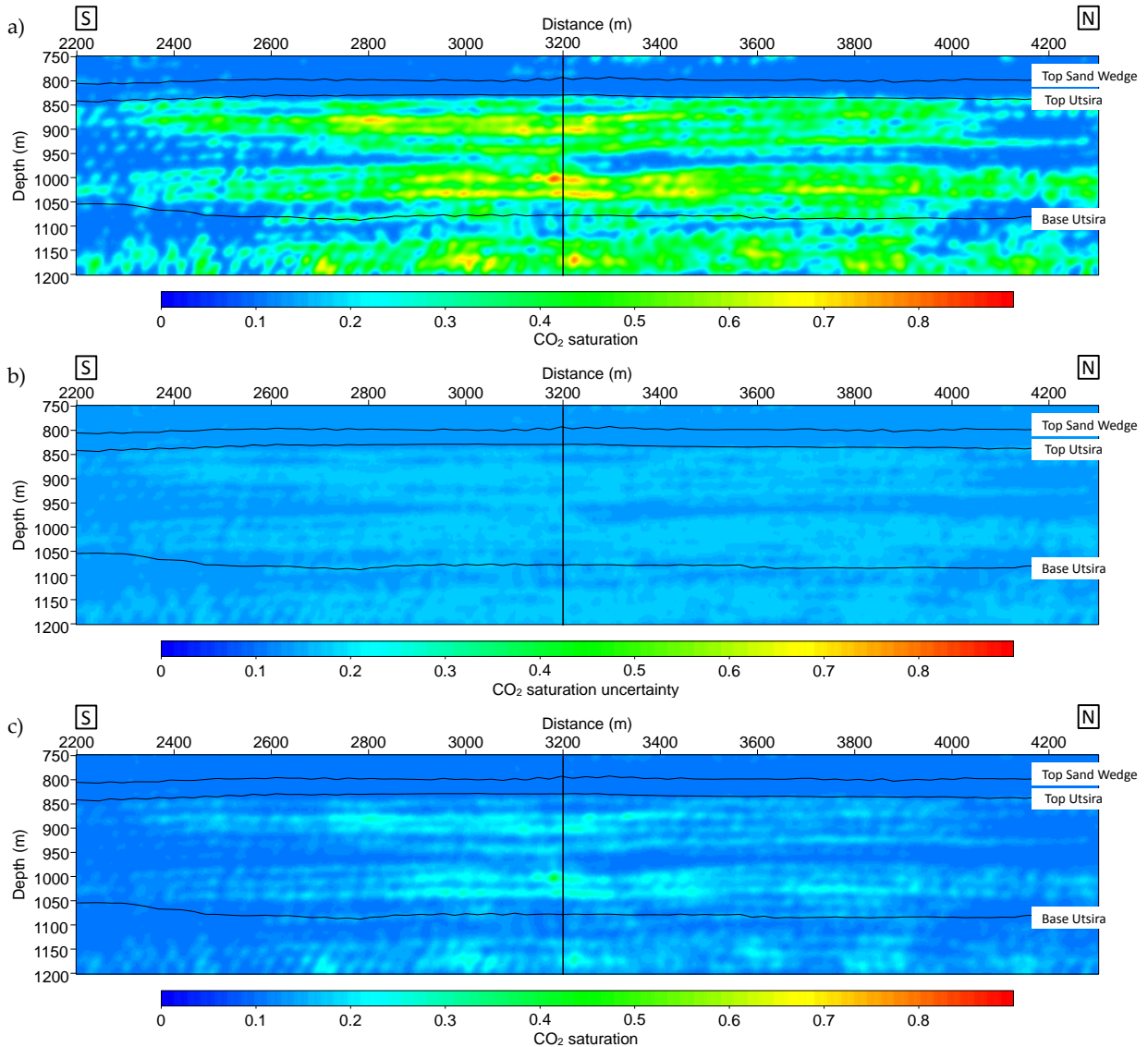
E. Estimation of CO₂ saturation using Vp if Brie exponent (e) is constant (Inline 1874)
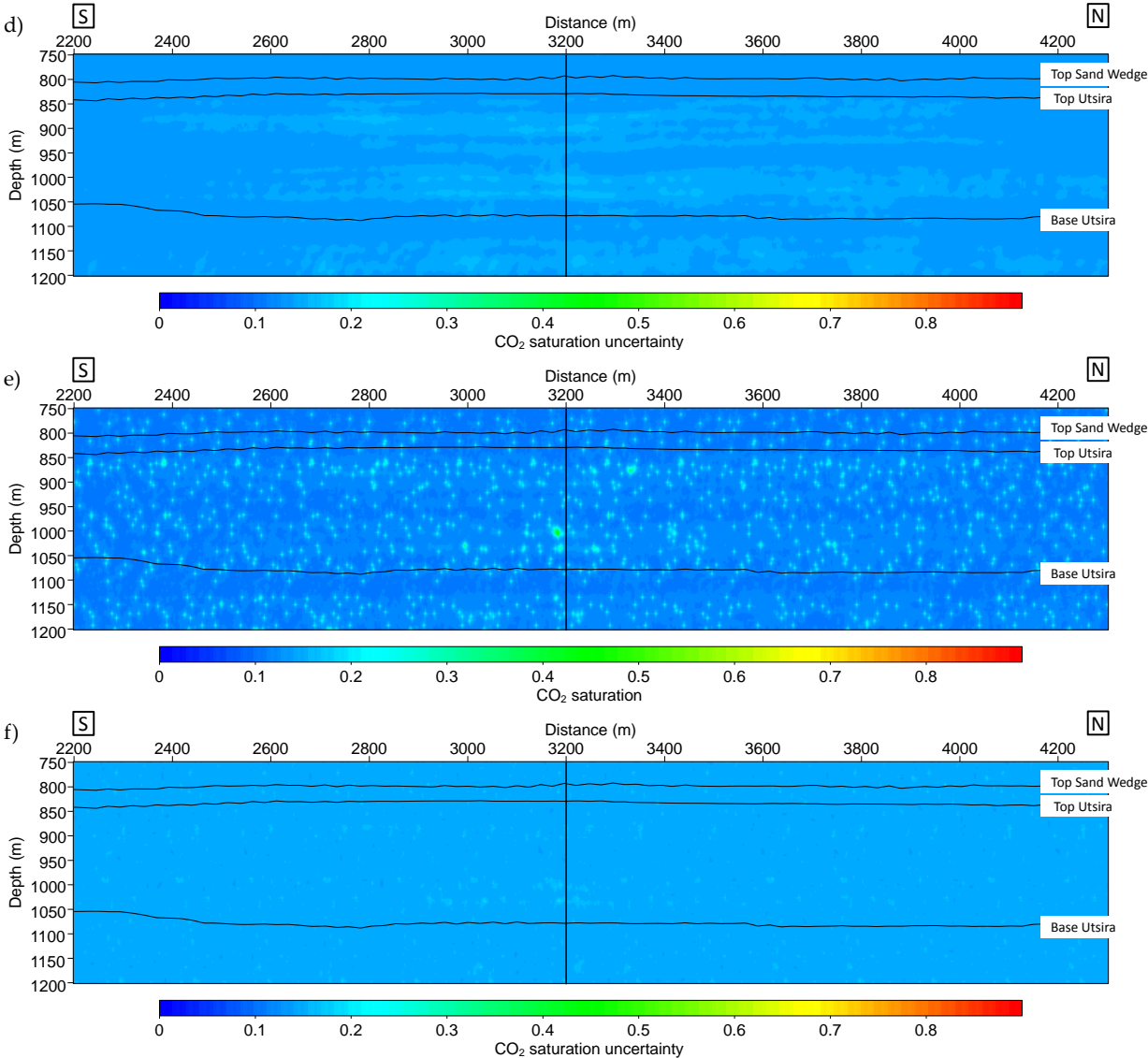
Figure E.1: 2D profile of CO₂ saturation and uncertainty at inline 1874 with (a & b) Brie exponent = 1, (c & d) Brie exponent = 5, and (e & f) Brie exponent = 40.
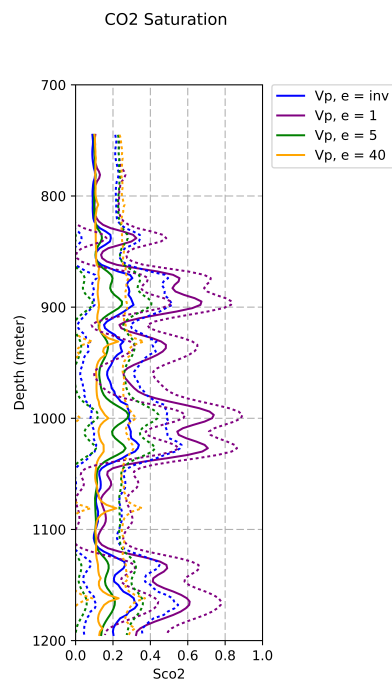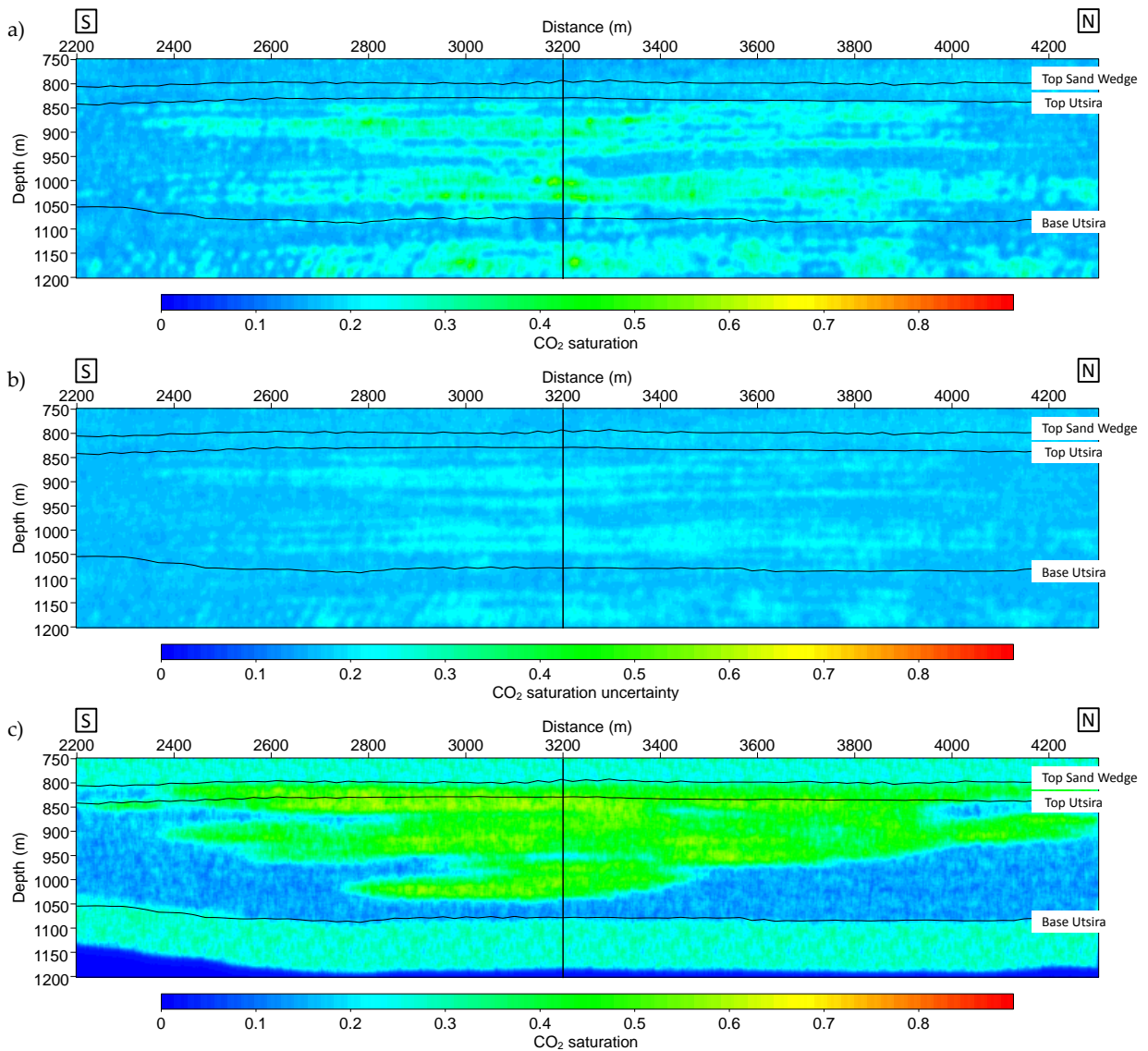
Figure E.2: 1D profile of CO$_2$ saturation inverted using Vp at x=3200, inline 1874 with constant Brie exponent. The CO$_2$ saturation with inverted e is also shown here for comparison. The dotted line are the mean value plus minus uncertainty.

Appendix F   Estimation of CO$_2$ saturation using Vp + Rt if Brie exponent (e) is constant (Inline 1874)

The 2D profiles of CO$_2$ saturation if Brie exponent is set as constant. Here, three values of e (1, 5, 40) are used and the inversion system become over-determined.
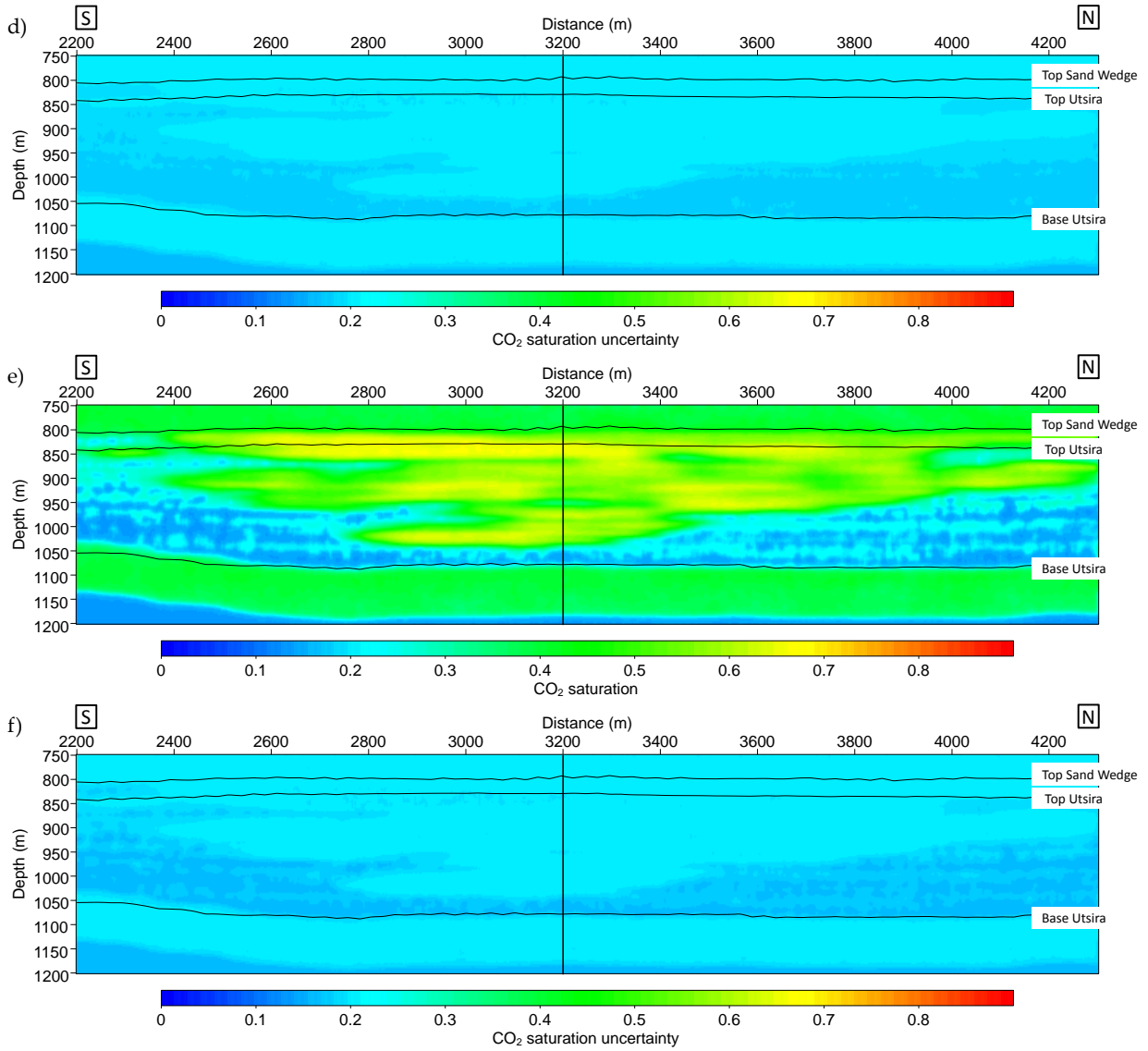
Figure F.1: 2D profile of CO_2 saturation and uncertainty at inline 1874 with (a & b) Brie exponent = 1, (c & d) Brie exponent = 5, and (e & f) Brie exponent = 40.
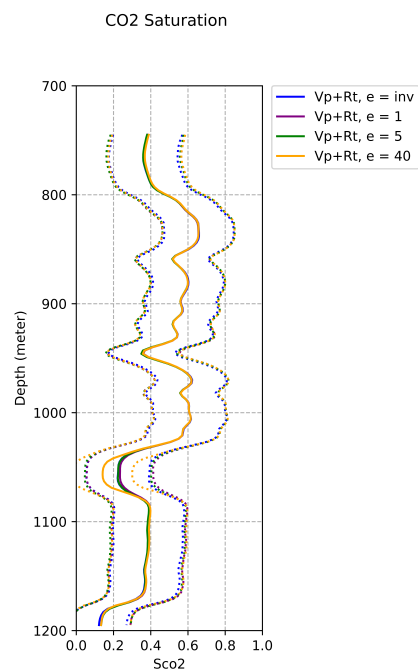
Figure F.2: 1D profile of CO$_2$ saturation inverted using Vp + Rt at x=3200, inline 1874 with constant Brie exponent. The CO$_2$ saturation with inverted e is also shown here for comparison. The dotted line are the mean value plus minus uncertainty.

Appendix G   Estimation of CO_2 saturation and Brie exponent (e) if porosity is inverted together using (Inline 1874)

The 2D profiles of CO_2 saturation, porosity, and Brie exponent are shown in Figure G.1, Figure G.3, and Figure G.5, respectively. Vp, Rt, and Vp+Rt are used as input, and porosity is inverted together with saturation and Brie exponent.

Estimation of CO_2 saturation

G. Estimation of CO₂ saturation and Brie exponent (*e*) if porosity is inverted together using (Inline 1874)
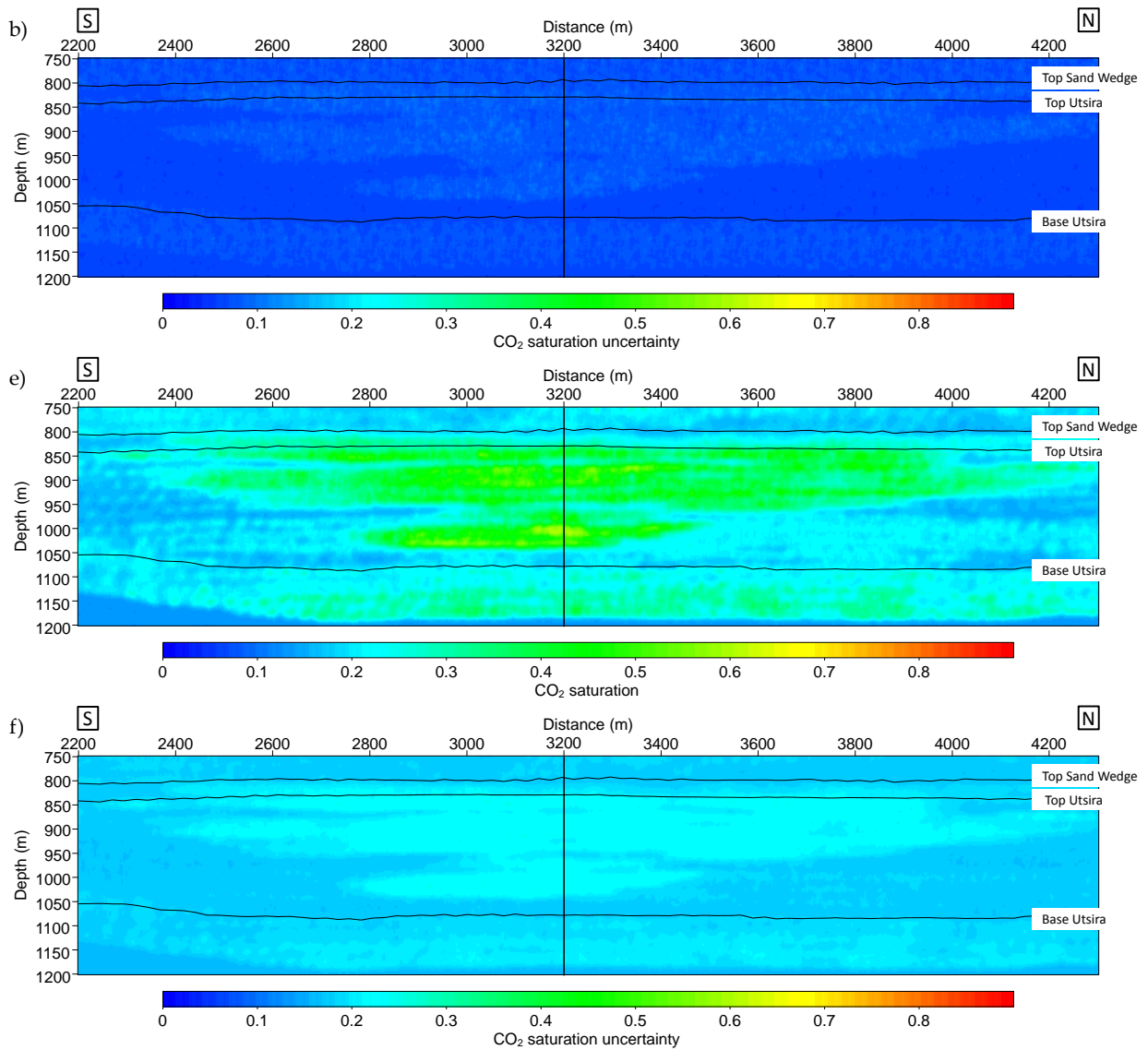
Figure G.1: 2D profile of (a & b) Using Vp, (c & d) Using Rt, (e & f) Using Vp + Rt
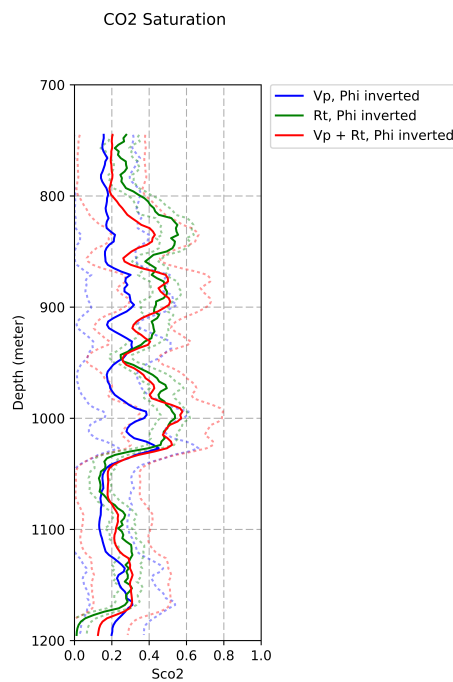
CO2 Saturation

Figure G.2: A comparison of 1D profile of CO$_2$ saturation if porosity is inverted together at
x=3200, inline 1874 using Vp, Rt, and Vp+Rt.The dotted line are the mean value
plus minus uncertainty.

Estimation of porosity
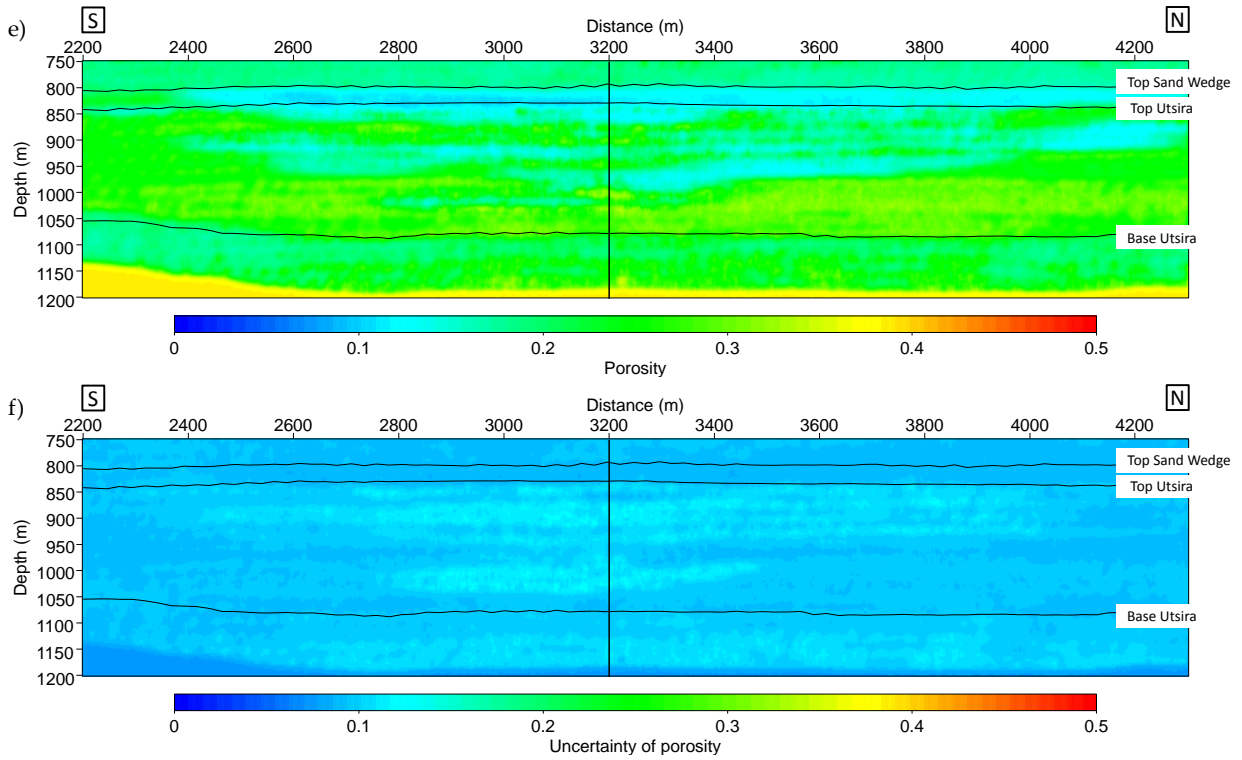
Figure G.3: 2D profile of porosity and uncertainty at inline 1874 if inverted together with CO_2 saturation and Brie exponent (a & b) Using Vp, (c & d) Using Rt, (e & f) Using Vp + Rt.
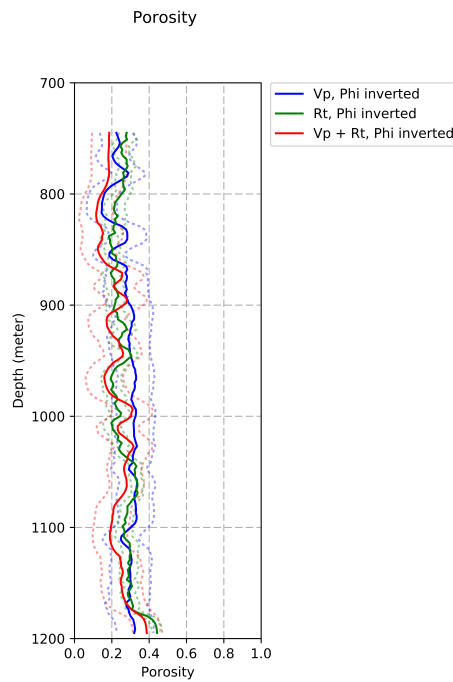

Figure G.4: Comparison of 1D profile of porosity if inverted together with CO_2 saturation and Brie exponent at x=3200, inline 1874 using Vp, Rt, and Vp+Rt. The dotted line are the mean value plus minus uncertainty.
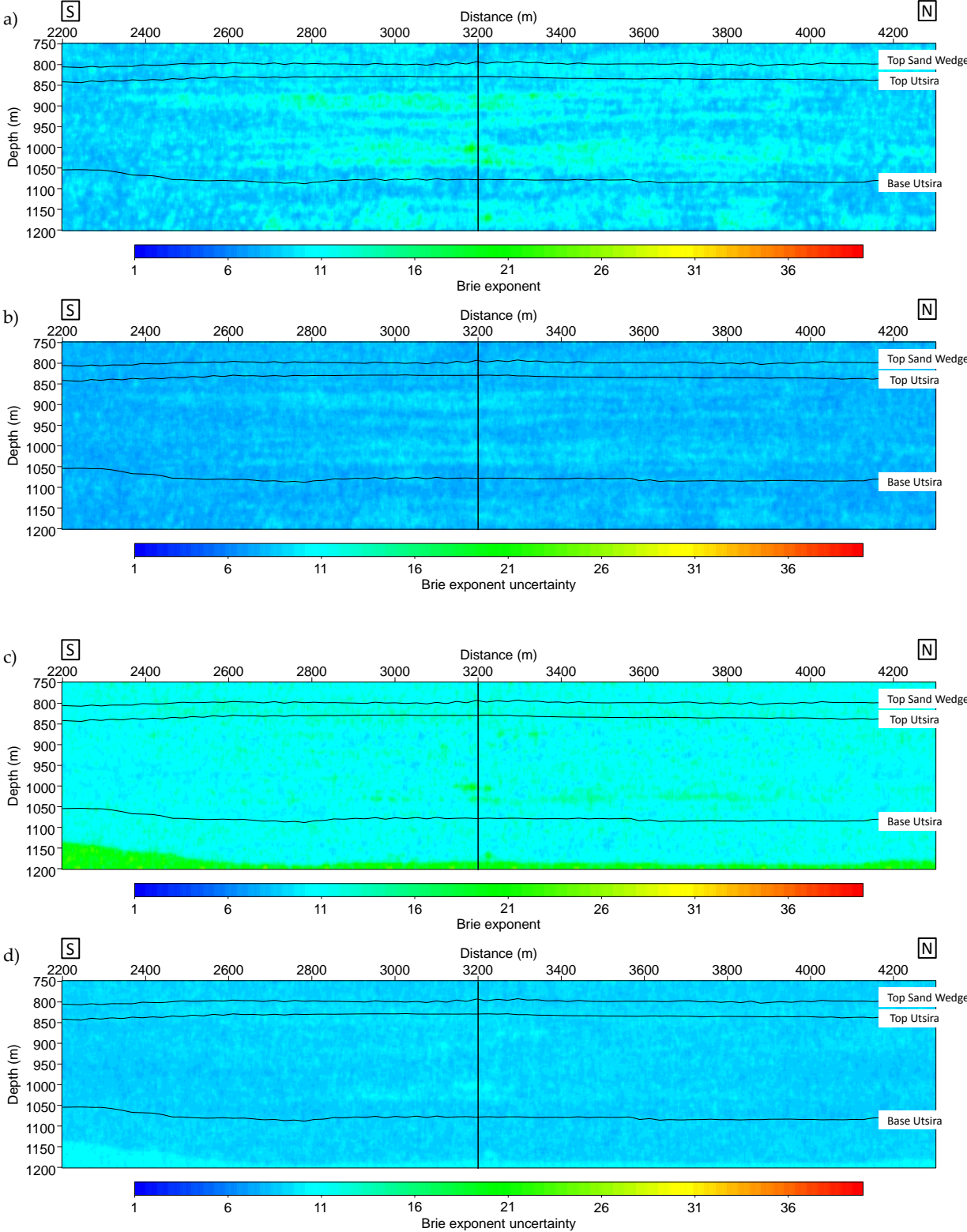
Estimation of Brie exponent (e)

Figure G.5: 2D profile of Brie exponent (e) at inline 1874 if porosity inverted together with
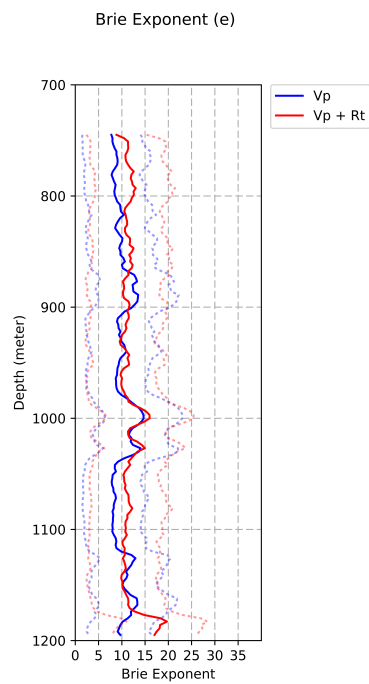CO_2 saturation and Brie exponent (a & b) Using Vp, (c & d) Using Vp+Rt.

Figure G.6: A comparison of 1D profile of Brie exponent if inverted together with CO$_2$ saturation and porosity at x=3200, inline 1874 using Vp and Vp + Rt. The dotted line are the mean value plus minus uncertainty.

Appendix H CO$_2$ saturation vs Brie Exponent at x=2500 m, Inline 1838 and at x=3200 m Inline 1874
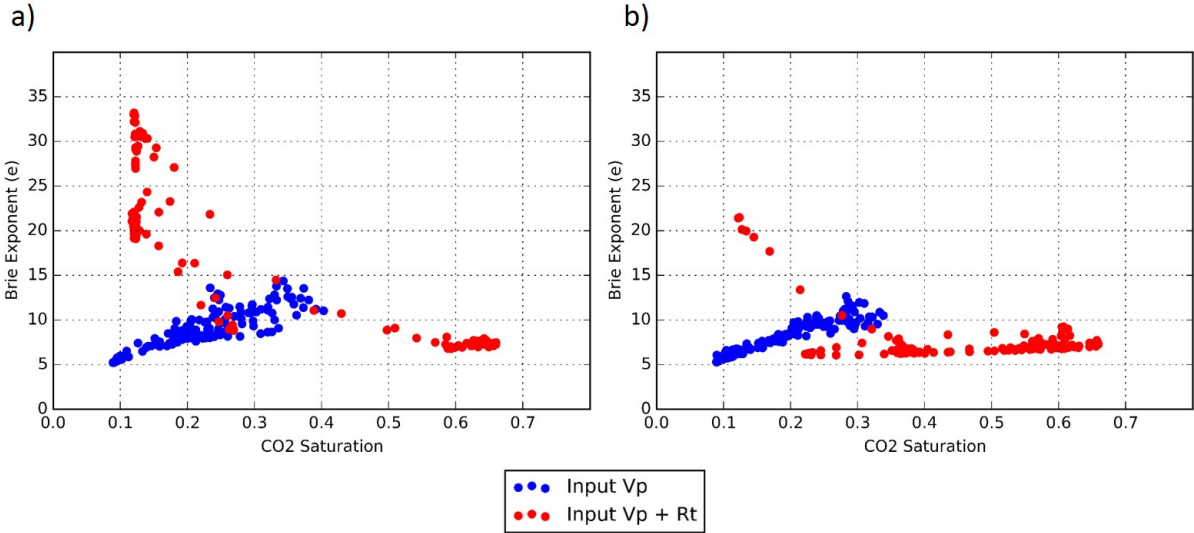

Figure H.1: CO$_2$ saturation vs Brie Exponent at (a) x=2500 m, Inline 1838 and (b) x=3200 m Inline 1874. Blue dots represent the inversion result using Vp only and red dots represent the inversion result using Vp and Rt.